Automotive Radar Self-Diagnostic Using Calibration Targets that are Embedded in Road Infrastructure

Erkut Yigit

Technische Universiteit Delft

TU Delft

Automotive Radar Self-Diagnostic Using Calibration Targets that are Embedded in Road Infrastructure

by

Erkut Yigit

in partial fulfillment of the requirements for the degree of

Master of Science

in Electrical Engineering

at the Delft University of Technology,

to be defended publicly on Thursday June 10, 2021 at 09:00 AM.

Student number:	1505386	
Thesis committee:	Prof. dr. A. Yarovoy,	TU Delft
	Dr. O. A. Krasnov,	TU Delft
	Dr. Ir. R. F. Remis,	TU Delft
	Dr. Nikita Petrov,	TU Delft

The work presented was performed at Microwave Sensing, Signals and Systems Group

Abstract

In order to ensure safety and prevent collisions on road, automotive radars must be fault proof and have to be tested on reliability and performance, which requires proper diagnostic of well-functioning of the radar so that the car may participate to traffic. One way of the diagnostic of well-functioning of the automotive radar is by means of calibration in service stations. In contrast to offline calibration in service stations, one another way of testing the automotive radar on well-functioning would be by means of monitoring the state, or with other words the healthiness, of the radar in real-time. One possible solution to monitor the radar state is to use a massive set of calibration targets in road infrastructure and thereby the problem lies in optimally estimating the state based on the RCS information provided by the radar. As a result, in the first part of this thesis, based on the defined target selection criteria, selection of the most appropriate calibration target among possible candidates is discussed.

Using massive set of targets is required to overcome the uncertainty in production and installation accuracy in one-target measurements. However, this method brings randomness which is caused by two error sources being the non-ideal shapes of the calibration targets originating from mass production errors and orientation errors either from installation or maintenance errors. Second part of the thesis investigates how this randomness affects the self-diagnostics performance of automotive radar. Thereby, the model of target orientation and RCS loss due to orientation errors, and, the model of target RCS and its RCS loss due to mass production errors are developed. For both error sources, the statistical characteristics of the loss factors are determined by means of corresponding probability distribution functions which are derived analytically. In case of orientation errors, analytical results are validated by Monte-Carlo simulations as well as Kullback-Leibler Divergence. In case of mass production errors, analytical results are validated by Monte-Carlo simulations only. Together with the results obtained in the first part, results of the statistical characteristics of the loss factor due to non-orthogonality help to find a balance between the size, quality and number of targets to be deployed in a certain range in a given road configuration.

To finalize the project, the measurement model is determined according to which the approach for self-diagnostics is developed under certain assumptions and considering a set of measurements of the same realization of a single target only. By the developed approaches, the relation of statistical parameters on self-diagnostics performance is determined by means of three different estimation methods and the results are validated by Monte-Carlo simulations.

Contents

List of Figures

List of Tables

1

Introduction

This chapter deals with the general overview of the thesis. The motivation for this thesis work is addressed in the first section which is then followed by a summary of the literature review of the calibration of both automotive radar and airborne SAR systems. The main contribution of this thesis project to autonomous driving as well as the novelties and the approach are then discussed in the next section. Finally, the outline of the remainder of the thesis is given in the last section.

1.1. Motivation

Through the advances and developments in millimeter-wave (mm-wave) semiconductor technology and signal processing techniques, autonomous driving became a reality and it gains increasing popularity nowadays. Together with different sensors such as lidar, ultrasound and camera's, automotive radars form the most important building block of self-driving cars and Advanced Driver Assistant Systems (ADAS). Biggest advantage these radars offer is their ability to see long distances (up to 200 m for Long Range Automotive Radar) ahead of the car when the visibility conditions are poor. As known, the information these radars provide are the radar cross section (RCS) of the encountered object(s), their velocity with respect to that of the car, distance to them and the angular position in terms of the elevation and azimuth coordinates. In order to ensure safety and prevent collisions on road, they must be fault proof and have to be tested on reliability and performance, which requires proper diagnostic of well-functioning of the radar so that the car may participate to traffic.

One way of the diagnostic of well-functioning of the automotive radar is by means of calibration in service stations. This type of calibration is performed offline using an object of known radar cross section placed at a known distance and orientation and it can be repeated in pre-determined periods. Despite the fact that there is full control over the environment involved in this calibration method, one drawback is that it might be expensive and time consuming, especially if the calibration has to be performed in relatively every short time periods.

In contrast to offline calibration in service stations, one another way of testing the automotive radar on well-functioning would be by means of monitoring the state, or with other words the healthiness, of the radar in real-time. One possible solution to monitor the radar state is to use a massive set of calibration targets in road infrastructure and thereby the problem lies in optimally estimating the state based on the RCS information provided. As a result, first part of this thesis is focused on the selection of the most appropriate calibration target among possible candidates.

Using massive set of targets is required to overcome the uncertainty in production and installation accuracy in one-target measurements in which, otherwise, the measurement environment must be fully controlled in terms of known RCS, distance, orientation, noise and eventually known clutter. However, this method introduces randomness into the project, which is caused by two error sources: I. Non-ideal shapes of the calibration targets originating from mass production errors, II. Orientation errors either from installation or maintenance errors. Therefore, a statistical approach is required in order to cope with the estimation problem here and, as a result, second part of the thesis is focused on statistical estimation of the state of the radar under certain assumptions.

With the results and the knowledge obtained in this thesis project, an improvement of safety of (semi-)autonomous vehicles can be achieved by means of improving reliability of automotive radars self-diagnostic to detect degraded radar performance via the developed approach which can make it possible to take it from offline to real-time.

1.2. Literature Review

Despite different kind of calibration targets and methods have been proposed and used for the calibration of different type of radar systems throughout the history, there is still a gap in the field of real-time calibration of automotive radars on the go. As discussed in the next chapter in more detail, these calibration targets are divided into two categories, being either active or passive.

Speaking of cars particularly, mainly active targets have been used in the calibration of cars. Examples comprise the alignment of the radar beam direction to the thrust vector of the vehicle in factory lines or service stations for initial calibration as depicted in figure 1.1. Used equipment thereby include lasers and transponders or receiving antennas which are integrated with power detectors [1],[2],[3].

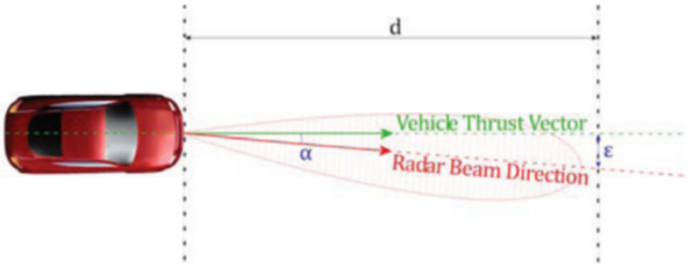

Figure 1.1: Error due to misalignment angle α between the vehicle thrust vector and the radar beam direction [3]

Speaking of airborne SAR systems, a ground based calibration experiment is reported in [4] where active radar calibrators and corner reflectors are used in conjunction with a test flight, whereas in [5] it is reported that using corner reflectors of known RCS as point targets for radiometric SAR calibration is simple and practicable. Figure 1.2 shows the arrangement of active radar calibrators (ARC) and corner reflectors (CR) deployed in the runway.

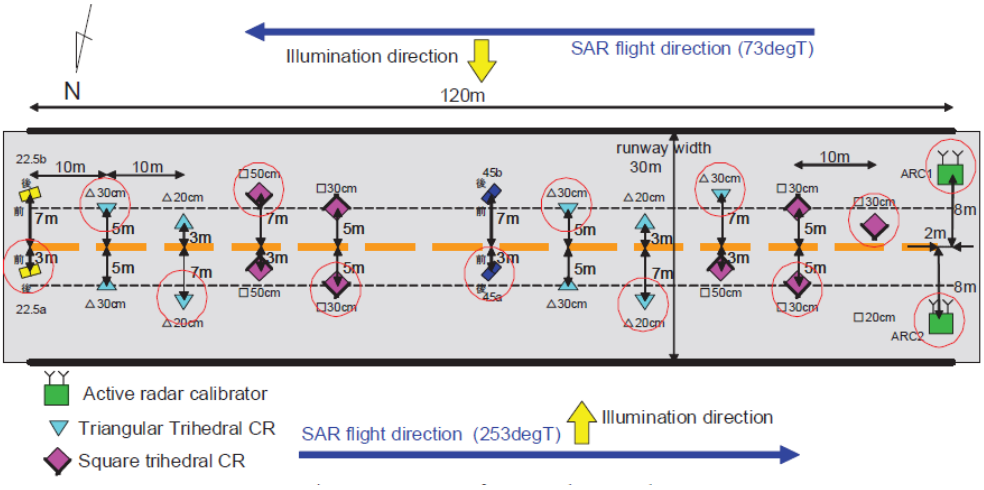

Figure 1.2: Arrangement of ARCs and CRs on the runway for the test flight [4].

1.3. Contributions, Novelties and Approach

This project investigates how the randomness, that is caused by the two error sources mentioned above, affects the self-diagnostics performance of automotive radar. In order to achieve this, first, the most appropriate calibration target is determined based on the defined target selection criteria, theoretically. This is then followed by the development of the model of target orientation and RCS loss due to orientation errors, and, the development of the model of target RCS and its RCS loss due to mass production errors. For both error sources, the corresponding probability distribution functions of the RCS loss factors are derived analytically. In case of orientation errors, analytical results are validated by Monte-Carlo simulations as well as Kullback-Leibler Divergence. In case of mass production errors, analytical results are validated by Monte-Carlo simulations only.

Then, the measurement model is determined according to which the approach for self-diagnostics, that is based on set of measurements of the realization of a single target, is developed under certain assumptions for convenience.

Finally, relation of statistical parameters on self-diagnostics performance is determined and the developed approach is validated by Monte-Carlo simulations.

1.4. Outline of the Thesis

This master thesis is organized as follows:

- Chapter 2 gives examples of a set of calibration targets which have been used throughout the history for the calibration of different type of radar systems. This is then followed by an evaluation of the calibration targets to determine the most appropriate one to use in this project based on the defined target selection criteria. Finally, based on a straight three-lanes European highway configuration and two different automotive radar specifications, minimum required size of the calibration target is determined.
- Chapter 3 deals with the statistical characteristics of RCS loss factors that originate from the two error sources. Thereby, the probability distributions of the loss factors are derived analytically for the four factors that cause reduction in the expected RCS to be returned from the selected calibration target. Then, validation of these analytical results are given which is followed by a distribution fit analysis that is performed on the histograms of each loss factors which are obtained via Monte-Carlo simulations. Furthermore, also the restrictions, that are put by the only single formula found from which the statistical characteristics of RCS loss factor due to non-orthogonality is determined, are investigated. Finally, the results of the beta distribution fit analysis on the histogram of total loss factor, assuming the size of the calibrator is accurate, are given and validated.
- Chapter 4 deals with the estimation of the quality metric based on which the healthiness of the automotive radar can be evaluated. Thereby the quality metric is defined first. Then, an estimation of this quality metric is done by means of three different estimation methods with each of them under certain assumptions.
- In Chapter 5 summarizes the findings and conclusions in this master thesis project, as well as some recommendations are provided for the future work.
- Appendix A gives the most important symbols used in the highway configuration as well as their meaning, formulas and their numeric values in a table for each of the corresponding figures.

2

Calibration Targets

Throughout the history, different kind of calibration targets have been proposed and used for the calibration of different type of radar systems. These calibration targets are divided into two main categories; active calibration targets and passive calibration targets.

2.1. Active Calibration Targets

Racor target, dopler/delay target and transponder are among the examples of active calibration targets. Racor target is a frequency shift reflector and needs both power supply and an antenna to be implemented. Doppler/delay radar targets are used to test and calibrate both pulse-Doppler radars and conventional pulse radars with Moving Target Indicator (MTI) modes of operation. This type of targets also need to be powered and use antenna as well. Transponder is a radio receiver which detects the energy and then transmits an amplified signal at a known level back to the radar. Figure 2.1 gives images of a racor target as well as a portable doppler/delay target.

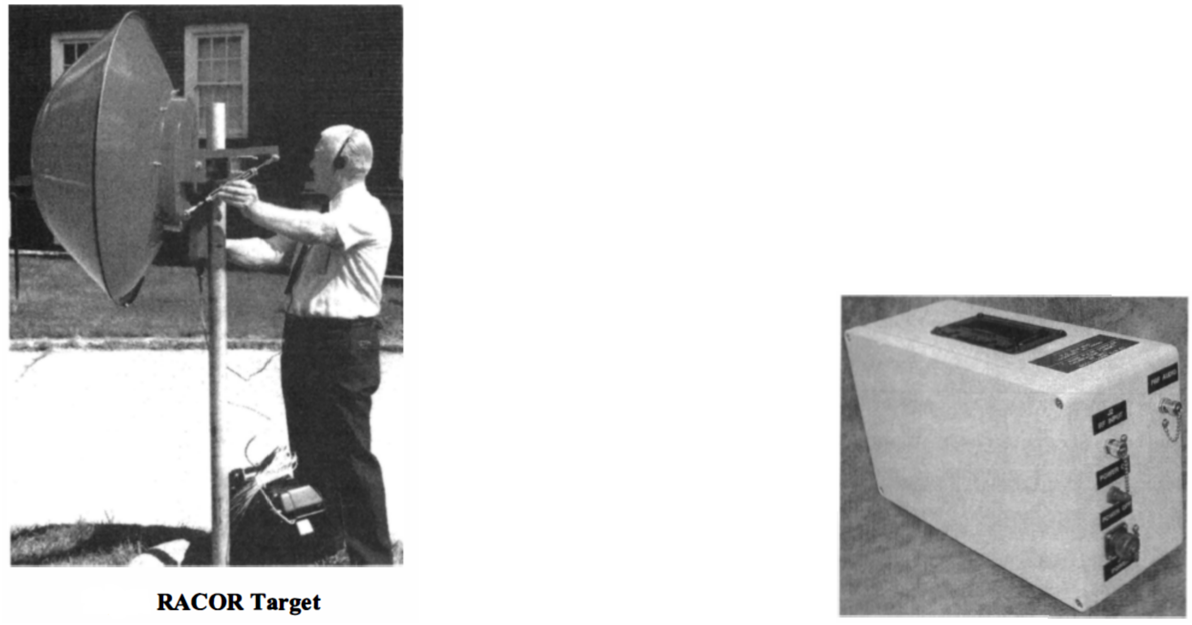

(a) RACOR target

(b) Portable Doppler/Delay Target

Figure 2.1: Examples of active calibration targets

2.2. Passive Calibration Targets

Examples of passive calibration targets are corner reflectors, metal spheres, rectangular metal plates and Luneburg Lens. There targets are used to calibrate different type of radar systems. One example is the calibration of Imaging Radar as well as Airborne SAR system using corner reflectors. Yet another example is the calibration of scatterometer using Luneburg Lens. Figure 2.2 gives the images of the examples mentioned above.

(a) Trihedral Corner Reflector (b) Metal Sphere (c) Rectangular Metal Plate

(d) Layers of Luneburg Lens

Figure 2.2: Examples of passive calibration targets

2.3. Existing Targets from Traffic Infrastructure

Besides the targets mentioned above, targets such as traffic signs and guide posts, that already exist in the current traffic infrastructure, can be considered as potential calibration targets. Figure 2.3 visualizes these two examples.

(a) Traffic Signs (b) Guide Posts

Figure 2.3: Examples of possible calibration targets already existing in the traffic infrastructure

2.4. Target Selection Criteria

Selection of the true calibration target is very important in the calibration of radar systems. Thereby there are some important desired characteristics that the calibration targets need to possess. These characteristics form also the criteria which the targets must fulfill and they are mainly:

1. Large and stable RCS;
2. Wide RCS pattern;
3. Low RCS sidelobes;
4. Small in physical size and weight;
5. Insensitivity of RCS to the surrounding environment;
6. Cost efficiency.

2.5. Selection of the Calibration Target

This section deals with the selection of the most appropriate calibration target to be used in this work. First, a comparison is made between the active and passive calibrators to determine which family of calibrators would be the most appropriate one. After that, a comparison is made among the set of targets from the family of calibrators determined from the first step.

2.5.1. Active Calibrators vs. Passive Calibrators

As already mentioned, calibration targets are divided into two main categories; active and passive. One big advantage of active calibrators is that the transmitted signal can be much larger than the signal scattered by passive calibrators. Yet another advantage is that the alignment problems, which do arise with passive calibrators, are not such a big issue since the communication antennas being used both for reception and transmission can have moderately broad antenna beams.

On the contrary, active calibrators comprise components such as power supply, antennas, delay elements, amplifiers and attenuators for their operation which makes them cost inefficient compared to passive calibrators. Additionally, the high amount of loss in the long coaxial cables makes active calibrators less attractive than passive calibrators. It is also apparent that the size and weight of these targets are in excess of that of the passive calibrators which make them impractical to deploy them around the roads and highways for automotive radar calibration.

From the discussion above, it is convenient to draw the conclusion that, considering the selection criteria, the disadvantages of active calibrators can be said to outweigh their advantages with respect to the passive calibrators. Therefore can be concluded that passive calibrators would be a more appropriate choice to use in the context of automotive radar calibration in real-time.

2.5.2. Evaluation of the Passive Calibration Targets

In section 2.5.1 concluded that the family of passive calibrators would be a more appropriate choice to use in this work. A search on the passive calibration targets that are being used for radar calibration resulted in corner reflectors, metal spheres, rectangular metal plates and Luneburg lens as mentioned in section 2.2. Below an evaluation is made for each of these targets separately.

Corner Reflectors Depending on the number of surfaces comprising them, corner reflectors are divided into two categories, being dihedral and trihedral corner reflectors. High-frequency radar cross section, that is estimated using geometrical optics and multiple scattering taken into account, for both dihedral and trihedral corner reflectors are given below.

Dihedral Corner Reflectors

For dihedral corner reflectors, the high-frequency RCS is given in [7] as:

$$\sigma(\theta = \frac{\pi}{2}, \phi) = \frac{16\pi a^2 b^2 \sin^2(\frac{\pi}{4} + \phi)}{\lambda_0^2} \tag{2.1}$$

with a the width of one plate and b being half of the length of the plate. Dihedral corner reflector has an obvious disadvantage. That is it provides a large and wide RCS only in the plane perpendicular to its corner faces, i.e. at $\theta = 90°$ as seen from the equation (2.1). Figure 2.4a represents a computed plot of equation (2.1) at f=77 GHz for $a = 0.1\ m$ and $b = 2a$. It is clear from this figure that the 3-dB pattern beamwidth of the corner reflector of the given dimensions at the given frequency is about 90°.

Trihedral Corner Reflectors

For triangular trihedral corner reflectors, the high-frequency RCS is given in [7] to be:

$$\begin{aligned} \sigma(\theta, \phi, l) \approx \frac{4\pi}{\lambda_0^2} l^4 [&\cos\theta + \sin\theta(\sin\phi + \cos\phi) \\ &-2[\cos\theta + \sin\theta(\sin\phi + \cos\phi)]^{-1}]^2 \end{aligned} \tag{2.2}$$

where l is the leg length of the reflector. From equation (2.2) it is obvious that the disadvantage of dihedral corner reflectors discussed above can be decreased to some extent with trihedral corner reflectors due to the flexibility in the elevation plane. Figure 2.4b gives a computed plot of equation (2.2) for different θ values at f=77 GHz for $l = 0.2\ m$. As seen from the figure, trihedral corner reflectors produce a large and wide RCS at a reasonably small dimension at the specified frequency. The 3-dB pattern beamwidth of the selected curve at $\theta = 30°$ in the figure is $2 \cdot 21.25° = 42.5°$, which is quite wide.

In the ideal case, walls of corner reflectors are orthogonal to each other. Any deviation from the orthogonality results in a reduction in the RCS of corner reflectors. Such a deviation might be caused, for example, by errors in the mass production of these reflectors in manufacturing.

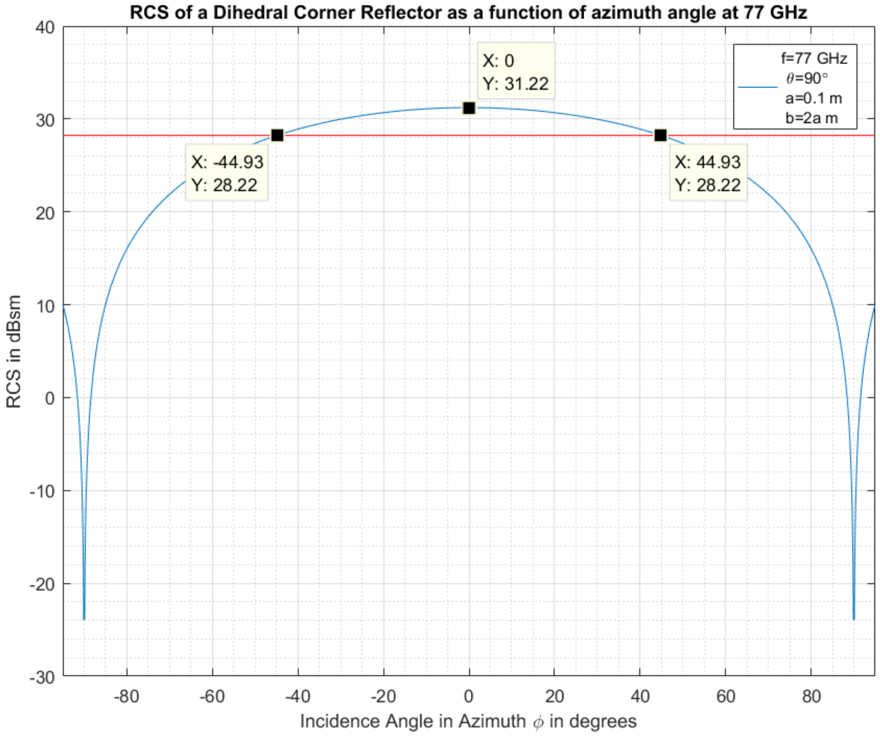

(a) RCS of a dihedral corner reflector

Metal Spheres For perfectly conducting metal spheres, the approximate solutions method in the far field gives the high-frequency radar cross section to be :

$$\sigma_{sph} = \pi a^2 \tag{2.3}$$

with a being the radius in x, y and z-directions [6]. One big advantage of metal sphere is that its radar cross section has no angular depencency which makes it insensitive to errors in orientation, as with Luneburg lens, but it is cheaper than Luneburg lens to construct. As obvious from the equation, it has a constant RCS value at a fixed size in terms of its radius a.
From Figure 2.5 one can conclude that in order to reach high RCS values, say RCS>30 dBsm, radius of the sphere must be a > 10 m already.

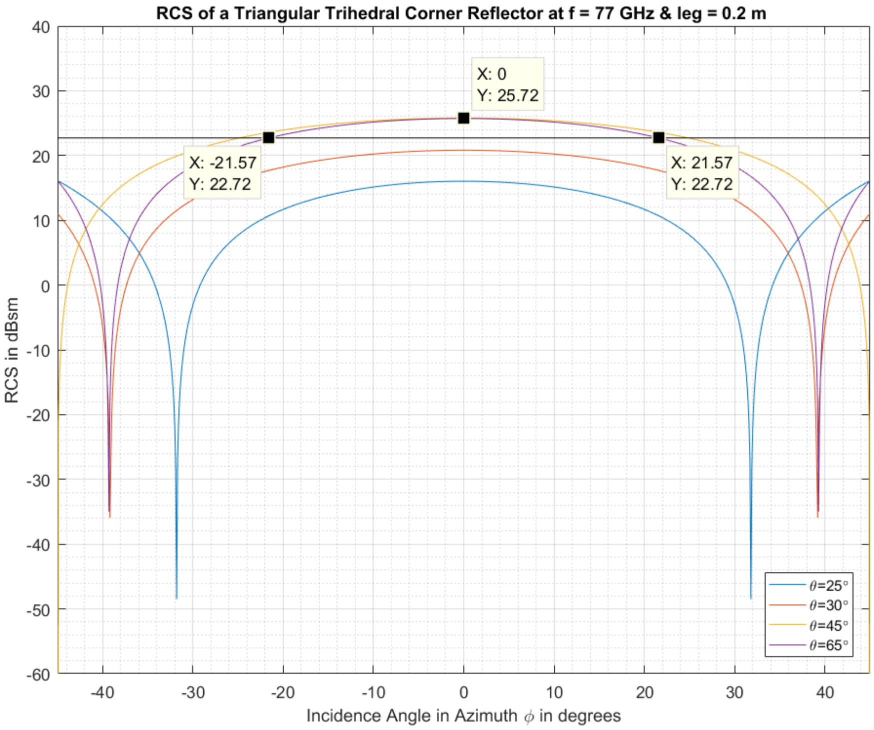

(b) RCS of a triangular trihedral corner reflector at different θ values

Figure 2.4: RCS of Corner Reflectors

Perfectly Conducting Ellipsoids

Since the radar cross section of metal spheres from equation (2.3) solely depends on their size, any external factor that results in a change in the radius would change its shape from sphere into an ellipsoid. This external factor could either be a hit or a mass production error in the radius in any direction, either x, y or z-direction. Therefore it is important to add ellipsoids into this discussion as well. Dependent on the ellipsoid semi-axes lengths, ellipsoids have two special cases, the prolate and oblate spheroid.

For perfectly conducting ellipsoids where $a \geq b \geq c$ with a, b, c being the ellipsoid semi-axes, radar cross section is given in [6] by the approximate solution for high-frequency to be:

$$\sigma(\theta, \phi) = \frac{\pi a^2 b^2 c^2}{[a^2 sin^2\theta cos^2\phi + b^2 sin^2\theta sin^2\phi + c^2 cos^2\theta]^2} \tag{2.4}$$

As apparent from equation (2.4), radar cross section of ellipsoids is both size and angular dependent in elevation as well as in azimuth plane. Figure 2.6 represents a computed plot of equation 2.4 as a function of azimuth incidence angle for different semi-axis lengths at $\theta 30°$. As it can be seen from this figure clearly that in order to reach a significant RCS value, semi-axis lengths of the ellipsoid need to be very big. Yet another disadvantage of an ellipsoid is that the 3-dB beamwidth of the RCS pattern gets large if the dimensions of the ellipsoid gets larger.

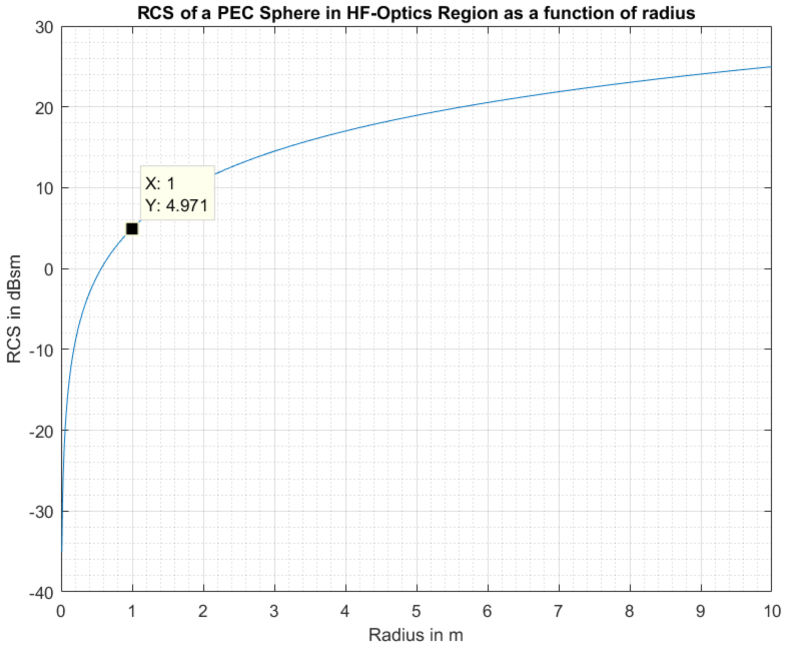

Figure 2.5: RCS of a Metal Sphere as a function of its radius

Prolate Spheroids

For perfectly conducting prolate spheroids where $a > b = c$, high-frequency radar cross section is given in [6] by the following formula:

$$\sigma(\theta = \frac{\pi}{2}, \phi) = \frac{\pi a^2 b^4}{[a^2 \cos^2(\phi) + b^2 \sin^2(\phi)]^2} \tag{2.5}$$

Equation (2.5) shows that in order to receive the scattered wave back from a prolate spheroid, incident wave in elevation plane must be $\theta = \frac{\pi}{2} = 90^\circ$, which means that otherwise the RCS can not be measured at all. This makes a prolate spheroid very sensitive to errors in orientation as a calibration target. As can be seen from figure 2.7a, which represents a computed plot of equation (2.5), RCS of a prolate spheroid has a low value even at reasonably big dimensions such as 1.2m x 0.7m. Additionally, the 3-dB pattern beamwidth depends pretty much on the dimensions, being about 55° for a=1.2m, b=0.7m and about 19° for a=1.2m, b=0.3m.

Oblate Spheroids

For perfectly conducting oblate spheroids where $a = b > c$, high-frequency solution for radar cross section is given in [6] by the following formula:

$$\sigma(\theta, \phi = 0) = \frac{\pi a^4 b^2}{[a^2 \sin^2(\theta) + c^2 \cos^2(\theta)]^2} \tag{2.6}$$

As can be seen from figure 2.7b, reaching a high RCS value goes at the expense of a narrower 3-dB pattern beamwidth; when the RCS has a value of 28.14 dBsm, corresponding 3-dB beamwidth is about 6.2° on the red curve, while the RCS corresponding to a 3-dB beamwidth of 34.2° is 14.16 dBsm on the yellow curve.

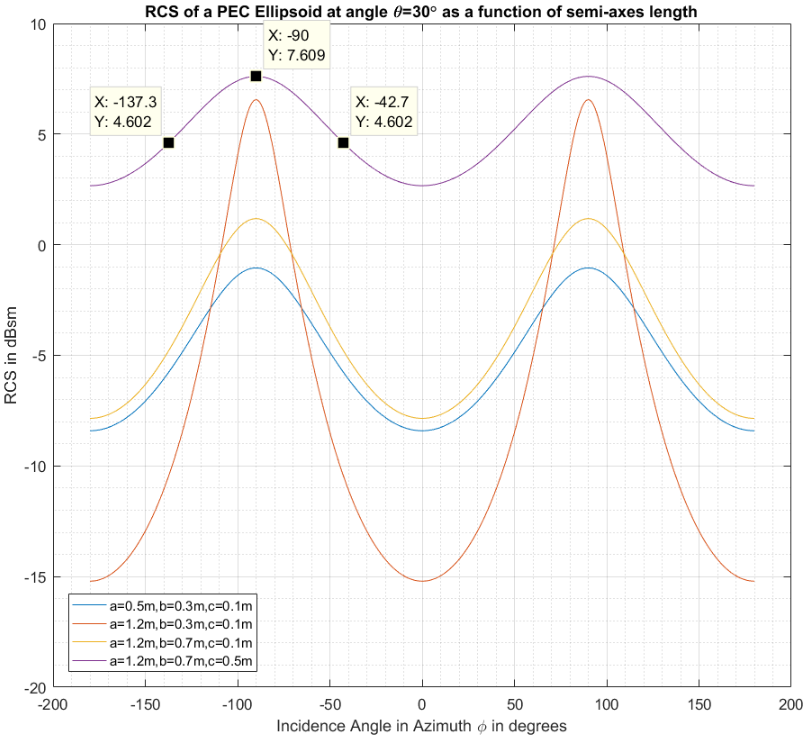

Figure 2.6: RCS of an Ellipsoid

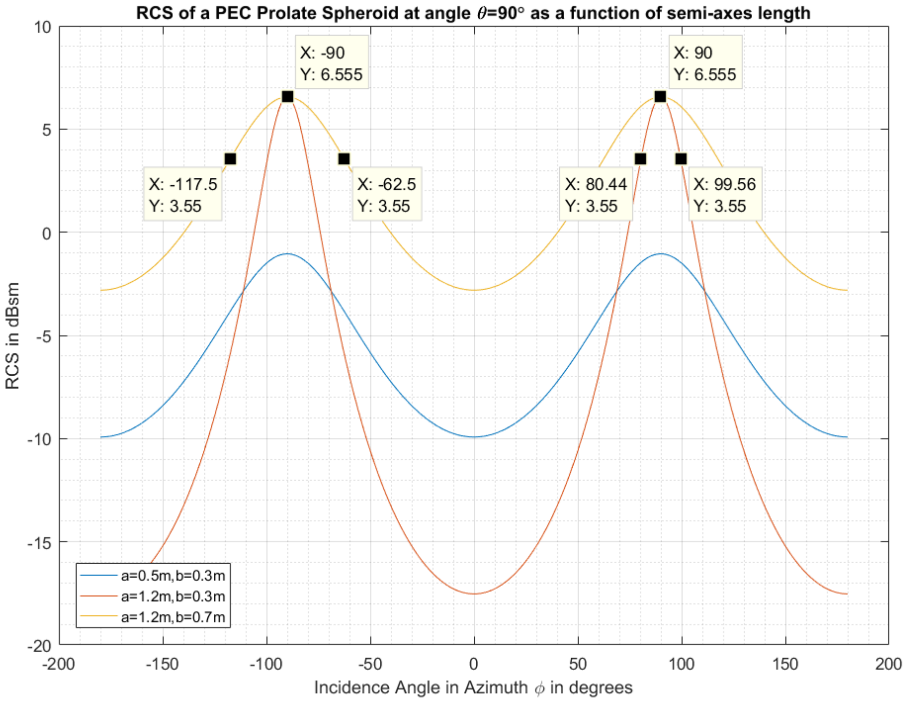

(a) RCS of a Prolate Spheroid

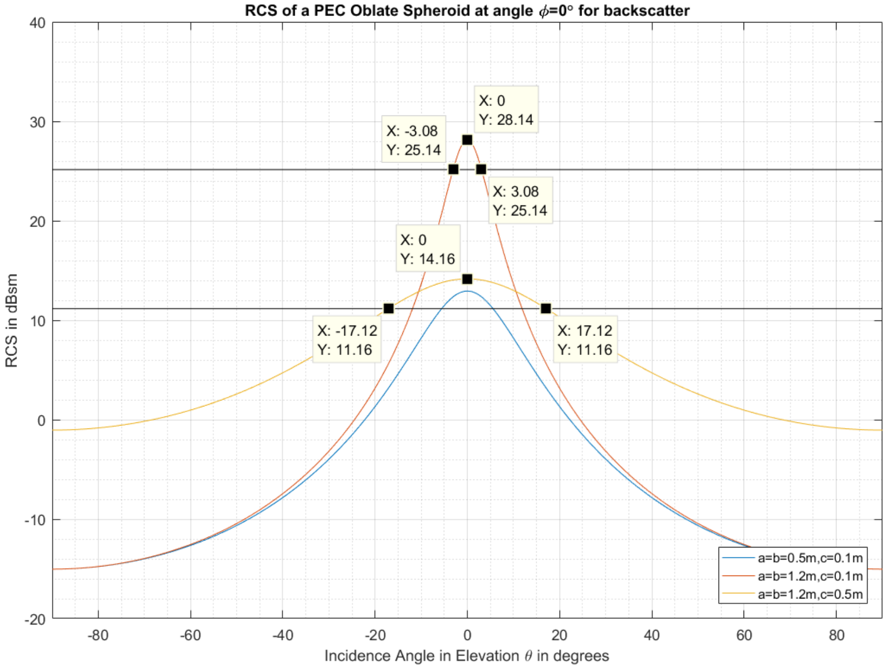

(b) RCS of an Oblate Spheroid

Figure 2.7: RCS of Prolate and Oblate Spheroids

Rectangular Flat Metal Plates For rectangular perfectly conducting metal plates, high frequency backscatter cross section has been obtained by the geometrical diffraction method by Ross and the results for both perpendicular and parallel polarizations are given respectively in [7] as:

$$\sigma_{\perp}(\phi) = \frac{b^2}{\pi} \Bigg| \left[cos(k_0 a sin\phi) - \frac{isin(k_0 a sin\phi)}{sin\phi} \right] - \frac{exp[i(k_0 a - \pi/4)]}{\sqrt{2\pi}(k_0 a)^{\frac{3}{2}}}$$
$$\times \left[\frac{1}{cos\phi} + \frac{exp[i(k_0 a - \pi/4)]}{4\sqrt{2\pi}(k_0 a)^{\frac{3}{2}}} \left(\frac{(1+sin\phi)exp[-ik_0 a sin\phi]}{(1-sin\phi)^2} + \frac{(1-sin\phi)exp[ik_0 a sin\phi]}{(1+sin\phi)^2} \right) \right]$$
$$\left[1 - \frac{exp[i(2k_0 a - \pi/2)]}{8\pi(k_0 a)^3} \right]^{-1} \Bigg|^2 \tag{2.7}$$

$$\sigma_{\parallel}(\phi) = \frac{b^2}{\pi} \Bigg| \left[cos(k_0 a sin\phi) + \frac{isin(k_0 a sin\phi)}{sin\phi} \right] - \frac{4\,\exp[i(k_0 a + \pi/4)]}{\sqrt{2\pi}(k_0 a)^{\frac{1}{2}}}$$
$$\times \left[\frac{1}{cos\phi} - \frac{exp[i(k_0 a + \pi/4)]}{2\sqrt{2\pi}(k_0 a)^{\frac{1}{2}}} \left(\frac{exp[-ik_0 a sin\phi]}{(1-sin\phi)} + \frac{exp[ik_0 a sin\phi]}{(1+sin\phi)} \right) \right]$$
$$\left[1 - \frac{exp[i(2k_0 a + \pi/2)]}{2\pi(k_0 a)} \right]^{-1} \Bigg|^2 \tag{2.8}$$

where k_0 is the free-space wavenumber, a is the plate width and b is the plate length.

As seen from the equations above, flat plates are sensitive to orientation errors, either in azimuth or elevation plane depending on the configuration of the plate. With ϕ being the aspect angle, computed plots of equations (2.7) and (2.8) are illustrated in figures 2.8a and 2.8b below, respectively.

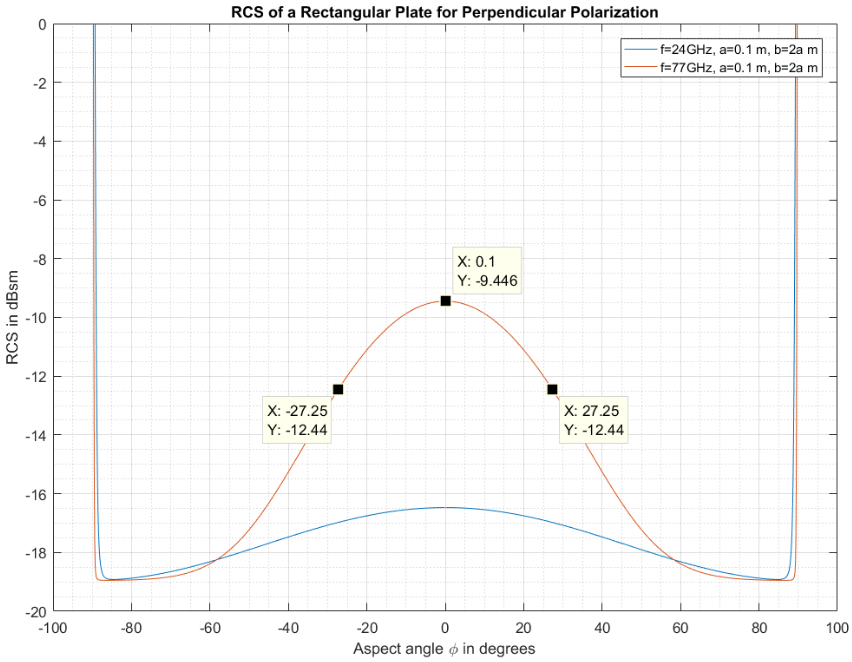

(a) RCS in Perpendicular Polarization

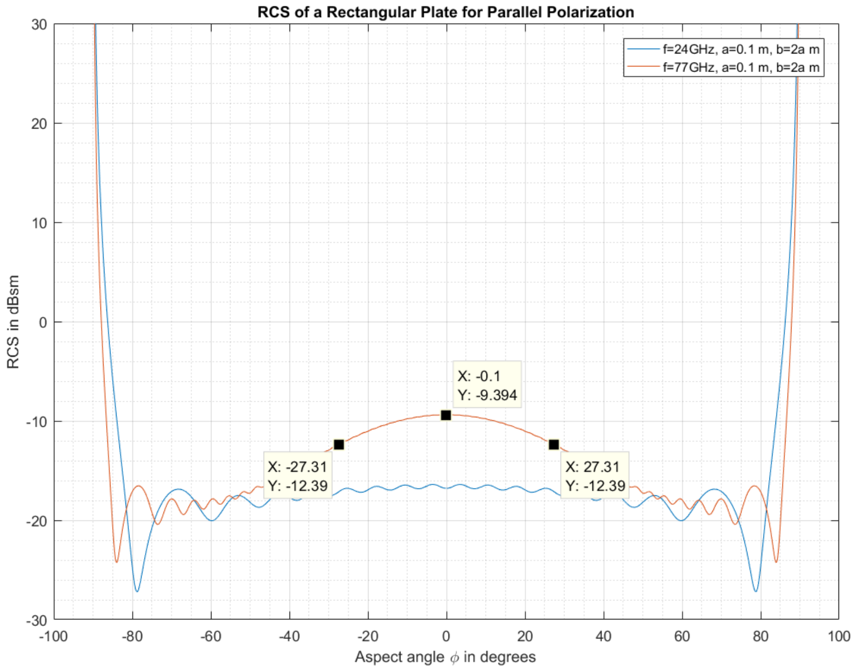

(b) RCS in Parallel Polarization

Figure 2.8: RCS of Rectangular Metal Plates in Perpendicular and Parallel Polarizations

Luneburg Lens A high-frequency approximate solution for the RCS of a Luneburg lens with a reflective coating is given in [6] to be:

$$\sigma = \pi k_0^2 a_0^4 \tag{2.9}$$

in which k_0 is the free-space wave number and a_0 is the lens radius. Luneberg lens offers some attractive features as a radar calibration target. It has a large radar cross section as well as insensitive to errors in orientation as also seen from the formula that it has no angular dependency. One very big disadvantage of Luneburg lenses is, however, that they are both difficult and costly to construct in sizes exceeding 0.5 m in diameter. One can read out from figure 2.9 that the RCS at $0.1m$ diameter is about 17 dBsm at f=77 GHz.

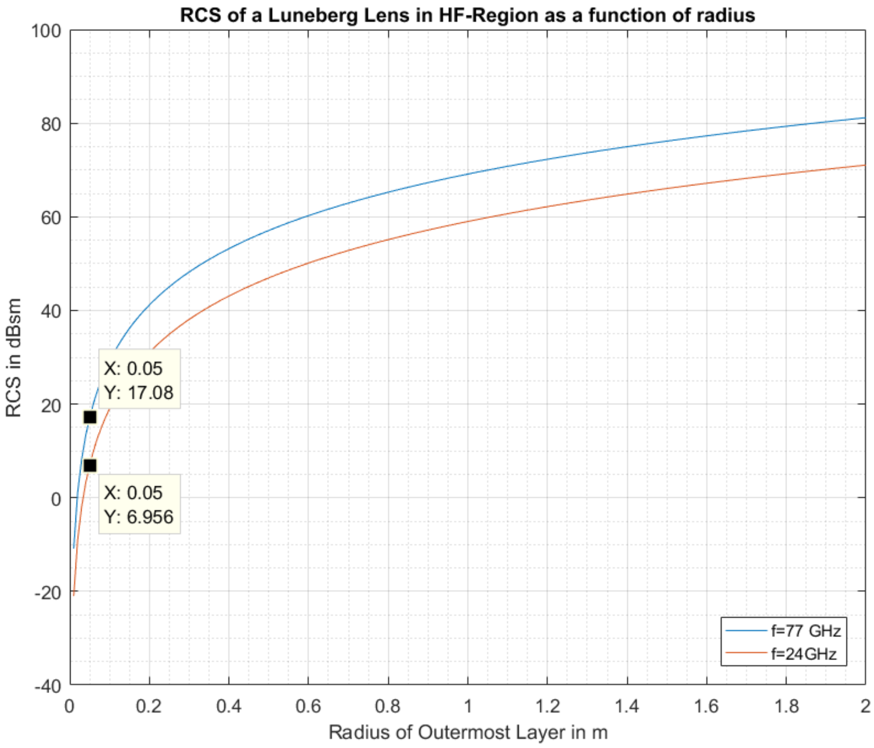

Figure 2.9: RCS of a Luneburg Lens as a function of its radius

2.5.3. Existing Targets from Traffic Infrastructure

As mentioned in section 2.3, objects already existing in the current traffic infrastructure can also be thought of as potential calibration targets. Traffic signs and guide posts are among those targets and their RCS characteristics are discussed below.

Traffic Signs It has been shown in [8] that the RCS of traffic signs is strongly angle dependent. Figure 2.10a represents the results of the RCS measurements conducted in [8] for different traffic signs. As can be seen from the figure, there occurs strong reflection from the traffic signs only if the plane of the sign is perpendicular to the radar, otherwise there is almost no back-scattering. Additionally, it is also shown here that the optical reflective cover material of two round traffic signs has no effect on their radar characteristics, i.e. RA2 vs. RA3.

Guide Posts In [9], it has been shown that guide posts can be discriminated from the cylindrical metal posts due to them having a unique RCS behaviour both in co- and cross- polarized channels. Metal post might either be the post used to hold up a traffic sign or bottom part of a traffic light or street light. Figure 2.10b as given in [9] shows the co- and cross-polarized RCS patterns of metal posts and dielectric guide posts. Note the sharp peaks at 105° and 255° in both co- and cross-polarized patterns. Additionally, the guide posts have a lower RCS because it is composed of a dielectric material. In conclusion, one can be sure about it that the object is a guide post when the RCS signature shows narrow sharp peaks in both co- and cross-polarized channels.

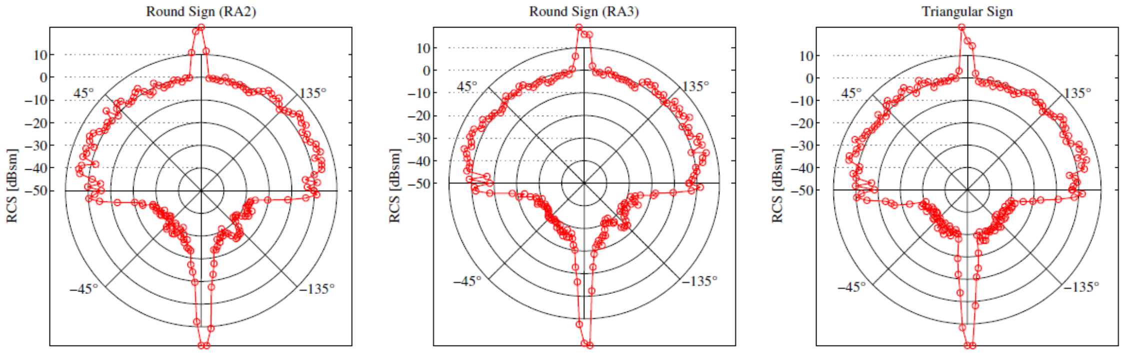

(a) Resulting angular diagrams of network analyzer RCS measurements [8].

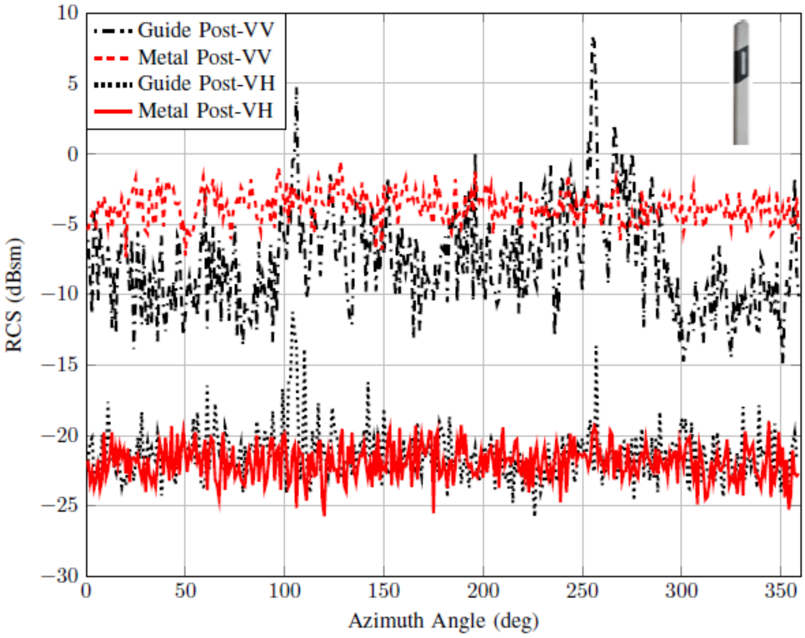

(b) RCS of metal and guide post [8].

Figure 2.10: RCS of existing targets from traffic infrastructure

2.5.4. Outcome of the Evaluation

Table 2.1 gives an overview of each of the calibrators discussed above and their characteristics according to the criteria listed in 2.4. In the comparison, same cross-section size has been used for the objects whenever possible and f=77 GHz.

In the table, green cells highlight what is considered to be the pro's and the red cells highlight what is considered as the con's that the calibrators exhibit based on the defined target selection criteria.

Evaluation resulted in that trihedral corner reflectors would be the most appropriate calibration targets to use in this project due to their relatively high RCS value, lesser sensitivity of RCS in orientation and reasonably wide 3-dB RCS pattern beamwidth with respect to other targets at reasonably comparable small size, weight and cost. 3-dB RCS pattern beamwidth is related to the RCS stability of the target since larger is the 3-dB RCS pattern beamwidth, higher is the stability of RCS of the target.

Table 2.1: **Characteristics of the Passive Calibrators (at f=76GHz when applicable)**

Target	**RCS Value [dBsm]**	**3-dB RCS beamwidth [degrees]**	**RCS Sensitivity**	**Physical Size [mxmxm]**	**Weight**	**Cost**
Luneburg Lens	17.08	n.a	n.a	0.10	*	***
Rect. Flat Metal Plates	~ 9.4	~ 54.5	****	0.10x0.20	*	*
Metal Spheres	4.97	n.a.	n.a	1	*	*
PEC Ellipsoids	7.6	94.6	**	1.2x0.7x0.5	*	*
Prolate Spheroids	6.55	55	*****	1.2x 0.7	*	*
Oblate Spheroids	14.16	34.2	**	1.2x1.2x0.5	*	*
Dihedral Cor. Ref.	31.22	89.8	****	0.1x0.2	*	*
Trihedral Cor. Ref.	25.72	43.14	***	0.2	*	*
Traffic Signs	20	a few	****	Round: 0.3 Triangular : 0.9	*	*
Guide Posts	8 at ϕ=255°	a few	*	1.73	*	*

[1] Number of $*$'s is used here as a weight metric which reflects how big, heavy, costly and sensitive to orientation errors the target is.

2.6. Calibration Target in a Highway Configuration

For triangular trihedral corner reflectors, the high-frequency RCS was given in equation (2.2) approximately as:

$$\begin{aligned}\sigma(\theta,\phi,l) \approx \frac{4\pi}{\lambda_0^2} l^4 [\cos\theta + \sin\theta(\sin\phi + \cos\phi) \\ -2[\cos\theta + \sin\theta(\sin\phi + \cos\phi)]^{-1}]^2\end{aligned} \tag{2.10}$$

where l is the leg length of the reflector [7].

The ideal orientation of the calibration target can be considered to be the pair of spherical incidence angles (θ_{ideal},ϕ_{ideal}) in elevation and azimuth planes, respectively, which maximizes equation (2.10) at a given leg length l and frequency f, because it is desirable to be able to receive the maximum amount of energy reflected back from the target into the automotive radar receiver. Any deviation from the pair of spherical incidence angles (θ_{ideal},ϕ_{ideal}) thus results in lower energy returned from the target.

Steps in modelling the configuration can be given as:

1. Determination of an appropriate position of the calibration target alongside the highway,
2. Range of incidence angles $\Delta\theta$ and $\Delta\phi$ into the calibration target,
3. Determination of the pair of ideal spherical incidence angles (θ_{ideal},ϕ_{ideal}),
4. Size of the calibration target,

Remainder of this section is build up following the steps mentioned above.

Additionally, the coordinate system used here is given in figure 2.11 as taken from [7].

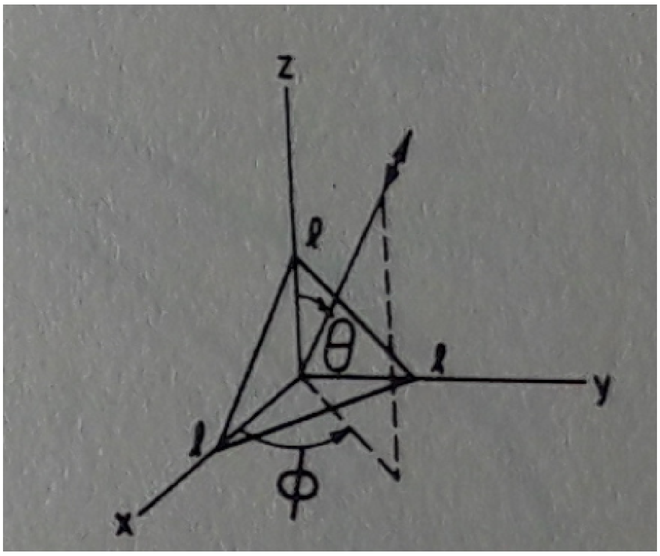

Figure 2.11: Coordinate system used for the orientation of the corner reflector [7].

2.6.1. Determination of an Appropriate Position of the Calibration Target alongside the Highway

The configuration used throughout this section concerns a straight European highway. The highway consists of three lanes, each of $w_{lane} = 3.75m$ wide and an Emergency Stopping Lane (ESL) of $w_{esl} = 2.5m$ wide, both as the European standards. Vehicles used in the configuration are assumed to be personal cars of $w_{car} = 2.0m$ wide.

An appropriate position of the calibration target is chosen to be point T which lies in between the points Q and P at a distance of d_1 m from point Q. This is represented in figure 2.12. Points Q and P are the nearest and furthest positions, respectively, to the ESL, where a calibration target can be placed considering visibility issues.

Additionally, based on this configuration, the distance between two successive targets is calculated to be at most $d = 66.243$ m as followed from the formula given in table A.1.

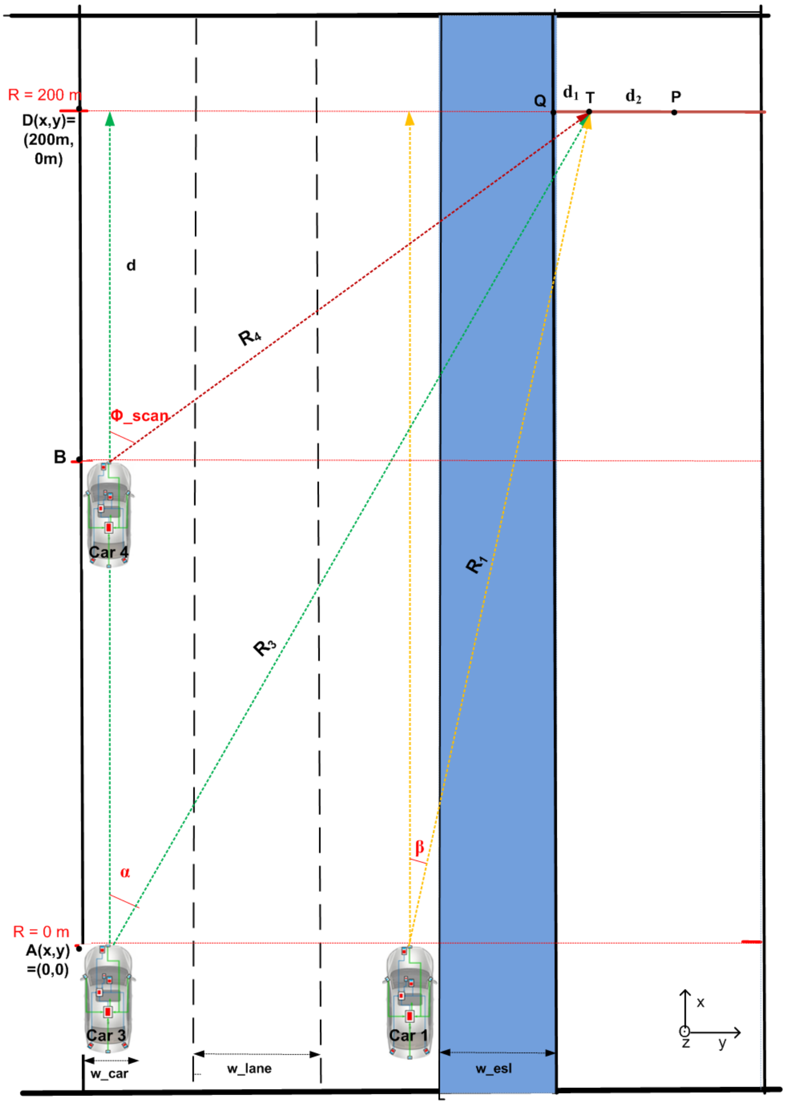

Figure 2.12: 3-Lanes highway configuration with calibrator placed at point T

2.6.2. Range of Incidence Angles

Determination of the range of spherical incidence angles ($\Delta\theta_{inc}$, $\Delta\phi_{inc}$) is based on the highway configuration from figure 2.12 which is extended further below according to visibility issues both in elevation and azimuth planes.

Range of Incidence Angles $\Delta\phi_{inc}$ in Azimuth Plane Consider figure 2.13, which is an extended version of figure 2.12. With the target placed at point T, range of incident angles $\Delta\phi_{inc}$ is decided by the vehicles Car 1 and Car 2 as represented. This range is highlighted in the figure as filled in with yellow color.

In this figure, ϕ_{ideal} represents the ideal orientation of the calibration target in azimuth plane which maximizes equation 2.2, with other parameters in the equation kept fixed. Moreover, ϕ_{min} and ϕ_{max} represents the two ends of the range of incidence angles $\Delta\phi_{inc}$ and they are expressed as:

- $\Delta\phi_{inc} = 90° - \zeta - \beta$,
- $\phi_{min} = \phi_{ideal} - 0.5 \cdot \Delta\phi_{inc}$,
- $\phi_{max} = \phi_{ideal} + 0.5 \cdot \Delta\phi_{inc}$.

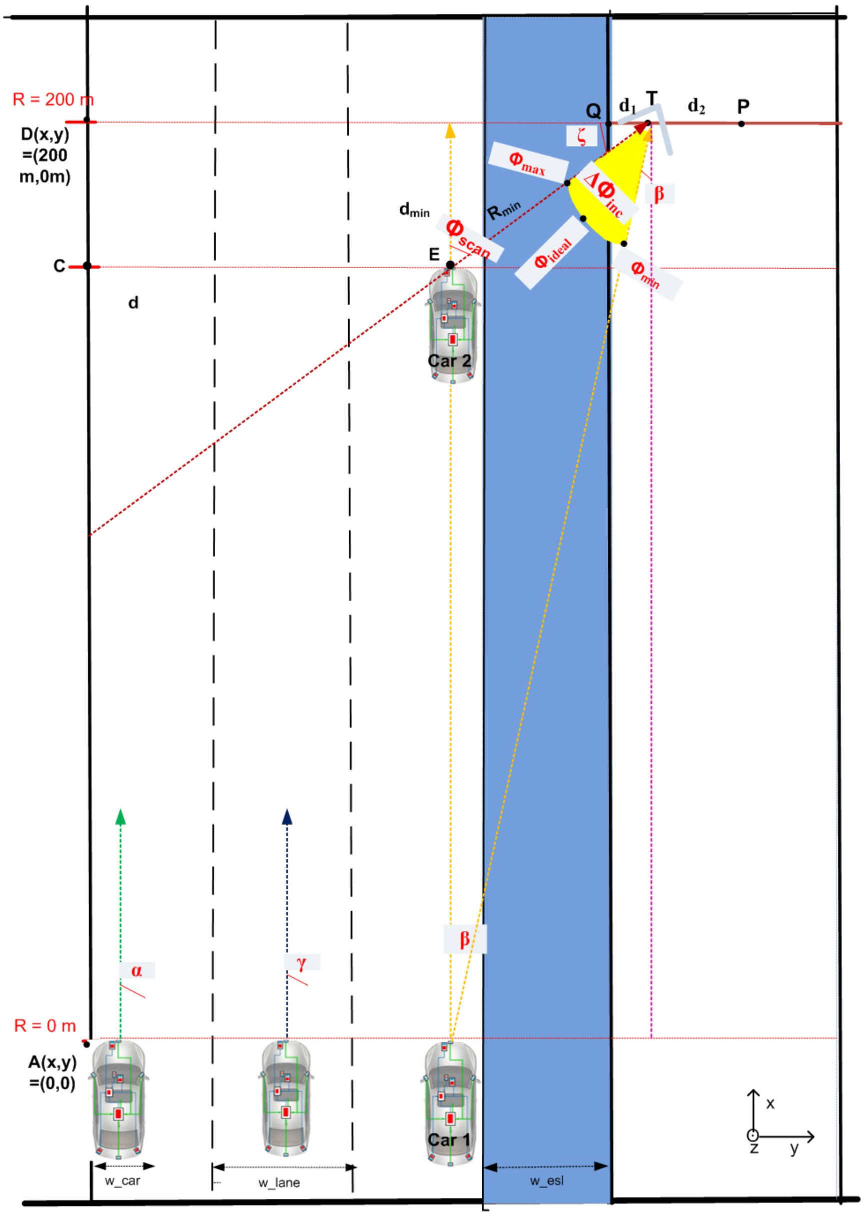

Figure 2.13: Configuration used for determination of the range of incidence angles $\Delta\phi_{inc}$ in azimuth plane

Range of Incidence Angles $\Delta\theta_{inc}$ in Elevation Plane Consider the configuration given in figure 2.14, where the calibration target is represented as the yellow dot. Automotive radars on the personal cars are assumed to be mounted at the height of h_{rad}. Also important is the maximum height h_{max}, above radar height h_{rad}, at which the calibration target can be placed such that it will be visible to all vehicles driving on the highway.

The maximum target height h_{max} is restricted by the vehicle, i.e. Car 2, which finds itself at the nearest possible position to the calibration target while the automotive radar still can detect the target. In other words, for heights above h_{max} this vehicle is not able to detect the target.

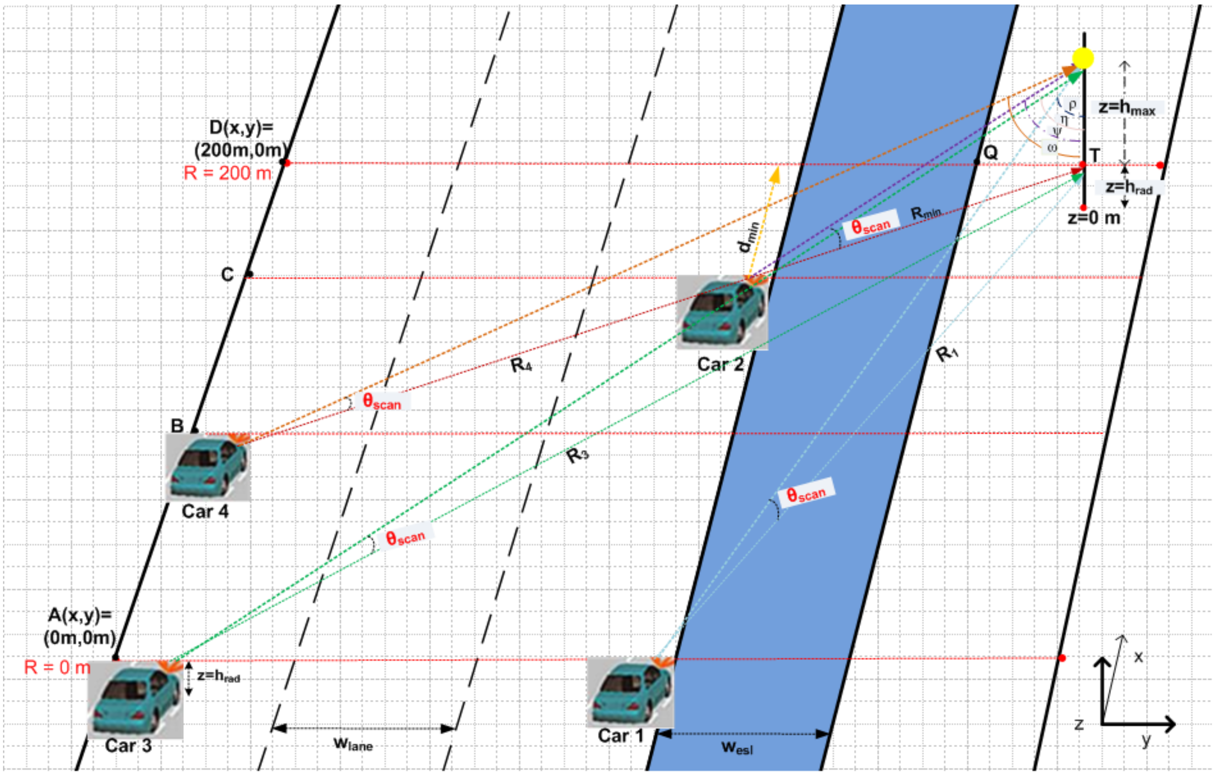

Figure 2.14: Configuration used for determination of the range of incidence angles $\Delta\theta_{inc}$ in elevation plane.

Note that this drawing is not drawn on the true scale and only meant for visual representation of the configuration. Therefore, for example, the angle ρ does not necessarily need to be smaller than the angle η despite the figure shows it the other way around.

The range of incidence angles in the used configuration thus concerns the region between θ_{max} and θ_{min}, which are computed as follow:

- $\Delta\theta_{inc} = \theta_1 - \theta_2$, where
- $\theta_1 = 180° - min\,\{\rho, \eta, \Psi, \omega\}$,
- $\theta_2 = 180° - max\,\{\rho, \eta, \Psi, \omega\}$,

  and,

- $\theta_{max} = \theta_{ideal} + 0.5 \cdot \Delta\theta_{inc}$,
- $\theta_{min} = \theta_{ideal} - 0.5 \cdot \Delta\theta_{inc}$.

2.6.3. Determination of the Pair of Ideal Spherical Incidence Angles

In 3.6 it is mentioned that the ideal orientation of the calibration target can be considered to be the pair of spherical angles (θ_{ideal},ϕ_{ideal}) which maximizes equation (2.10) within the appropriate interval of incidence angles. The idea behind this is clearly that the automotive radar gets the maximum RCS return from the target.

First, the ideal incident angle ϕ_{ideal} in azimuth plane is determined by evaluating equation (2.10) at different θ_{inc} values where the frequency and size of the corner reflector kept fixed as $f = 77\ GHz$ and $l = 0.10\ m$. Figure 2.15a shows that the maximum RCS is reached at $\phi_{inc} = 45°$ at all θ_{inc} values. Therefore, it is concluded that $\phi_{ideal} = 45°$.

Having determined ϕ_{ideal}, a further evaluation of equation (2.10) at $\phi_{inc} = 45°$, with the frequency and size of the corner reflector kept fixed as $f = 77\ GHz$ and $l = 0.10\ m$, shows in figure 2.15b the ideal incident angle in elevation plane to be $\theta_{ideal} = 54.7°$.

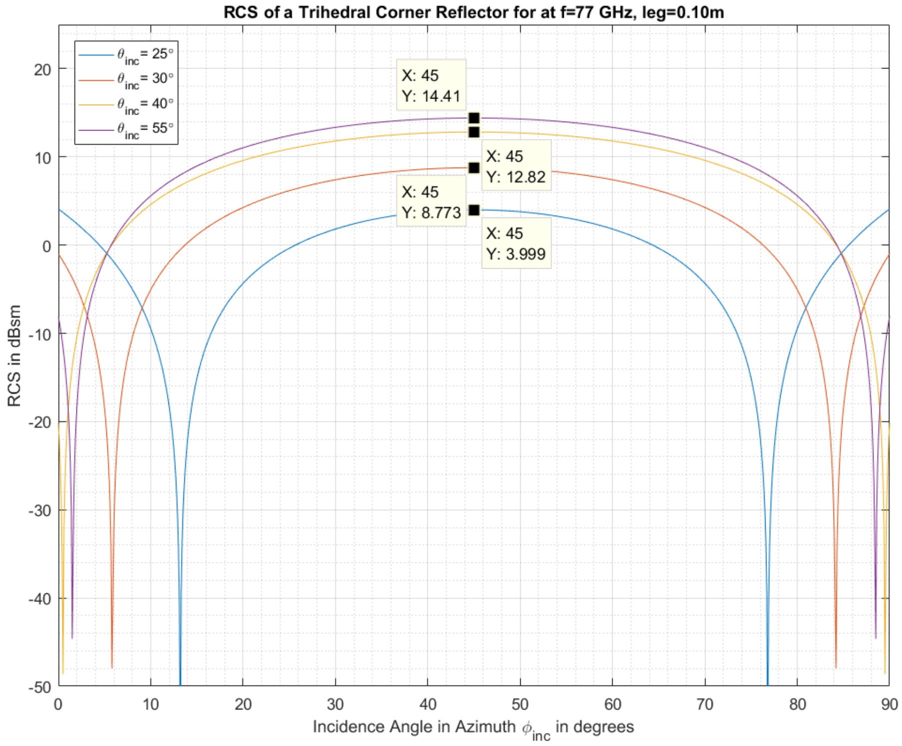

(a) RCS of a trihedral corner reflector as a function of azimuth incidence angles ϕ_{inc} at different elevation incidence angles θ_{inc}.

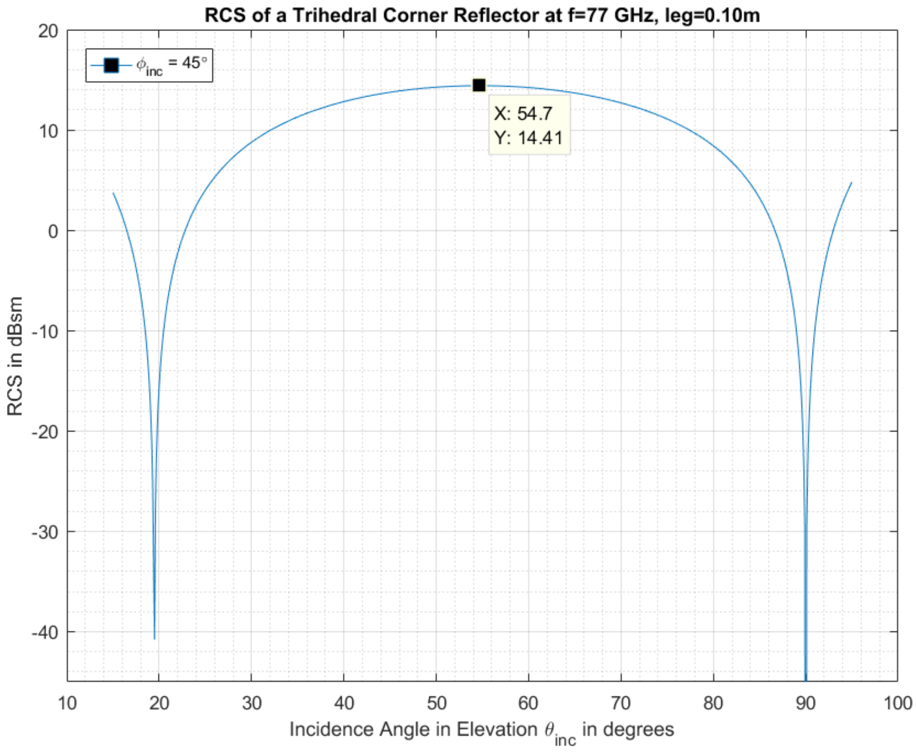

(b) RCS of a trihedral corner reflector as a function of elevation incidence angles θ_{inc} at the ideal incident angle ϕ_{ideal}.

Figure 2.15: Evaluation of equation (2.2) to find the ideal pair of spherical incidence angles (θ_{ideal},ϕ_{ideal}).

2.6.4. Size of the Calibration Target

Re-writing equation (2.10), size of the reflector follows to be approximately:

$$l \approx \left(\frac{\sigma_{req} \cdot \lambda_0^2}{4\pi[\cos\theta_{ideal} + \sin\theta_{ideal}(\sin\phi_{ideal} + \cos\phi_{ideal}) - 2[\cos\theta_{ideal} + \sin\theta_{ideal}(\sin\phi_{ideal} + \cos\phi_{ideal})]^{-1}]^2} \right)^{1/4} \tag{2.11}$$

Factors that determine the size of the leg length are thus the minimum required RCS σ_{req} of the calibration target and the ideal pair of spherical incidence angles (θ_{ideal},ϕ_{ideal}) at the given frequency. The minimum required RCS σ_{req} is calculated using the specifications of the automotive radar in question through the radar range equation.

Radar Range Equation The radar range equation for automotive FMCW radars in the form of (required) SNR, including the free-space losses, can be given as:

$$SNR = \frac{P_r}{P_n} = \frac{P_t G_t G_r \lambda^2 \sigma_{req}}{(4\pi)^3 R^4 k T_0 F B L_{sys}} F_{pr}^4 \cdot (\tau B) \tag{2.12}$$

with G_t = G_r= G in monostatic radar case, where;

- P_n is the thermal noise power kT_0FB ,
- L_{sys} is the system loss comprising transmitter losses, atmospheric losses, receiver losses, signal processing losses, the polarization mismatch loss and additionally the losses due to wet radome. Therefore, L_{sys} [dB] = L_{tr} [dB] + L_{atm} [dB] + L_{rec} [dB] + L_{sp} [dB] + L_{pol} [dB] + L_{rad} [dB], respectively. Assuming that signal processing losses L_{sp}, atmospheric losses L_{atm} and the polarization missmatch losses L_{pol} are negligible and that the transmitter and receiver losses, L_{tr} and L_{rec} are accounted for in the gains G_t and G_r , the system loss becomes $L_{sys} = L_{rad}$.

- F_{pr}^4 is the two-way propagation factor in the power form. This propagation factor is assumed to be 1 in the free-space conditions.
- σ_{req} is the minimum required RCS of the calibration target to be visible by the automotive radar in question.

and finally,

- (τB) is the waveform's *time-bandwidth* (TB) *product* coming from the *Pulse Compression Gain*.

The Minimum Required RCS σ_{req} Re-writing the radar range equation from equation (2.12) in the RCS form results in:

$$\sigma_{req} = \frac{SNR_{req.}(4\pi)^3 R^4 k T_0 F B L_{rad}}{P_t G^2 \lambda^2} \cdot (\frac{1}{\tau B}) \tag{2.13}$$

From equation 2.13 can be seen that the size of the target depends in turn on the radial distance R as well.

Specifications Recommmendation ITU-R, M.2057-0 System characteristics to be used in equation (2.13) for the calculation of the required RCS σ_{req} can be taken from the Recommmendation ITU-R, M.2057-0, "Systems characteristics of automotive radars operating in the frequency band 76-81 GHz for intelligent transport systems applications" [10]. Table 2.2 gives an overview of the recommended system characteristics both for long range radar and short range radar.

Table 2.2: **Automotive radar characteristics in the frequency band 76-81 GHz [10].**

Parameter	**Long Range Radar**	**Short Range Radar**
Sub-band used (GHz)	76-77	77-81
Max necessary bandwidth(GHz)	1	4
Typical sweep time (μs)	10 - 40 for fast FMCW	10 - 40 for fast FMCW
Maximum transmit power to antenna (dBm)	10	10
Receiver Sensitivity (dBm)	- 115	- 120
Receiver noise figure F (dB)	15	12
Antenna main beam gain(dBi)	Typical 30, Maximum 45	TX: 23 RX: 13
Antenna height (m)	0.3 - 1 above road	0.3 - 1 above road
Antenna azimuth scan angle(degrees)	TX/RX: ±15	TX/RX: ±50
Antenna elevation (degrees)	TX/RX: ±3	TX/RX: ±5.5

From the specifications, minimum required signal-to-noise ratio at the input of the receiver can be calculated to be $SNR_{req.,ITU} = \frac{P_r}{P_n} = \frac{-115\ dBm}{-98.977\ dB} = 16.02\ dB$, where T_0 is taken to be 290K in the calculations.

Range R in equation (2.13) is the maximum possible direct line-of-sight distance between the car and the calibration target while the target is still visible to the radar.From the configuration represented in figure 2.12 follows that $R = R3$.

Furthermore, in [11], it is shown that, depending on the thickness of the water film on the surface of radome formed by rain drops when the automotive radar operates in the adverse weather, amount of loss can become as high as $20\ dB$. Therefore, the amount of loss due to wet radome is considered to be $L_{rad} = 20\ dB$ as well as the pulse duration of $\tau_{ITU} = 10\ \mu s$. Additionally, the antenna gain is assumed to be $G = 30\ dBi$ and the operational bandwidth is assumed to be $B_{ITU} = 1\ GHz$.

Putting these values in equation (2.13) results in the required RCS to be $\sigma_{req.,ITU} = 0.3186\ dBsm$.

Specifications Continental ARS 30X Long Range Radar On the other hand, the required RCS $\sigma_{req.}$ can also be computed using the specifications of a commercial radar, for which the ”Continental ARS 30X Long Range Radar” is taken as an example here. Table 2.3 below gives the values of some important characteristics of this radar for far field measurements.

Table 2.3: **Some important system characteristics of Continental ARS 30X Long Range Radar [12].**

Continental ARS 30X Radar Sensor **77 GHz (for far field)**	
Distance Range	0.25 ... 200 m far field
Radar Operating Frequency Band	76 - 77 GHz
Transmission Capacity	<10 mW ≡ 10 dBm
Range Resolution	2 m
Range Accuracy	0.25 m
Speed Range	- 88 km/h ... +265 km/h
Speed Resolution	2.76 km/h
Speed Accuracy	0.5 km/h
Cycle Time	66 ms

Range Resolution and Bandwidth

From the range resolution, the operational bandwidth B is calculated from the following formula to be:

$$\begin{aligned} \Delta R = \frac{c}{2B} \quad -> \quad B &= \frac{c}{2\Delta R} \\ &= \frac{3 \cdot 10^8\ m/s}{2 \cdot 2\ m} = 75\ MHz \end{aligned} \tag{2.14}$$

Range Accuracy and Default SNR_0

From the range accuracy, we can calculate the SNR_0 as follows:

$$\delta R = \frac{c}{2B\sqrt{2SNR_0}} \quad -> \quad SNR_0 = \frac{1}{2}\left(\frac{c}{2B \cdot \delta R}\right)^2 \tag{2.15}$$

Filling in the values from the table, the result is $SNR_0 = 32 \equiv 15.05\ dBm$.

Speed Resolution and Observation Time CPI

From the speed resolution, the doppler frequency resolution is calculated as follows:

$$\Delta v_r = \frac{\lambda \Delta f_d}{2} \; -> \; \Delta f_d = \frac{2\Delta v_r}{\lambda} \tag{2.16}$$

Since the observation time CPI is the inverse of the doppler frequency resolution :

$$CPI = \frac{1}{\Delta f_d} = \frac{\lambda}{2\Delta v_r} \tag{2.17}$$

Filling in the values gives for the observation time $CPI \approx 2.55\ ms$.

Speed Range, PRF, N_{pulses} and the SNR

From the speed range, the maximum unambiguous radial speed $v_{r,max}$ is calculated to be:

$$\begin{aligned} v_{r,max.} &= \frac{88+265}{2}\ km/h \\ &= \frac{353}{2}\ km/h \\ &= 176.5\ km/h \\ &\approx 49.02\ m/s \end{aligned} \tag{2.18}$$

Since in general holds that $v_r = \frac{\lambda \cdot PRF}{2}$, filling in the corresponding values gives the PRF to be:

$$PRF = \frac{2v_{r,max.}}{\lambda} = 25\ kHz \tag{2.19}$$

Additionally, CPI is a function of the PRF, and so pulse time τ, and the number of pulses used for the estimation:

$$CPI = \frac{N_{pulses}}{PRF} = N_{pulses} \cdot \tau \tag{2.20}$$

Therefore, the number of pulses, or chirps in this case, can be calculated as follows:

$$\begin{aligned} N_{pulses} &= CPI \cdot PRF \\ &= 2.55\ ms \cdot 25\ kHz \\ &= 63.75 \\ &\approx 64. \end{aligned} \tag{2.21}$$

Assuming that coherent integration is used in the estimation process, the default SNR_0 is improved by the number of pulses used. Therefore,

$$\begin{aligned} SNR(N_{pulses}) &= SNR_0 \cdot N_{pulses} \\ &= 32 \cdot 64 \\ &\equiv 33.11\ dB. \end{aligned} \tag{2.22}$$

Pulse Time

From equation (2.20) follows that, the pulse time is:

$$Pulse\ Time\ \tau_{CONT} = \frac{CPI}{N_{pulses}} = \frac{2.55\ ms}{64} \approx 40\ \mu s. \tag{2.23}$$

Having determined the operational bandwidth to be $B_{CONT} = 75\ MHz$, the minimum required signal-to-noise-ratio to be $SNR_{req.,CONT} = 33.11\ dB$, the pulse duration to be $\tau_{CONT} = 40\ \mu s$ and again assuming $L_{rad} = 20\ dB$ and $G = 30\ dBi$, putting these values in equation (2.13) results in the required RCS to be $\sigma_{req.,CONT} = 11.38\ dBsm$.

Size of the Corner Reflector Having determined the minimum required signal-to-noise-ratio values $SNR_{req.,ITU}$ and $SNR_{req.,CONT}$, and thereby the minimum required RCS values $\sigma_{req.,ITU}$ and $\sigma_{req.,CONT}$ from both specifications and the pair of incidence angles to be ($\theta_{ideal} = 54.7°$, $\phi_{ideal} = 45°$) as shown earlier, filling in these values in equation (2.11) at the frequency $f = 77\ GHz$ results in that the size of the corner reflector should be minimum l_{min} $[m]$ values, which are given in table 2.4, in order to reach the minimum required RCS under the given pair of ideal incident angles.

Note that in case of ”Continental ARS 30X Long Range Radar” the minimum size l_{min} $[m]$ has been calculated only for the combination of the signal-to-noise value of $SNR = 33.11 dB$ and a pulse time of $\tau_{CONT} = 40\ \mu s$ since these are the values obtained from the known specifications above.

Table 2.4: **Minimum required size of the corner reflector l_{min} $[m]$ for combinations of different SNR_{req} and pulse duration τ values.**

		Pulse Duration τ **[μs]**			
		$10\ (= \tau_{ITU})$	20	30	$40\ (= \tau_{CONT})$
SNR Values [dB]	$SNR_{req.,ITU} = 16.02$	0.0444 m	0.0374 m	0.0338 m	0.0314 m
	25	0.0745 m	0.0627 m	0.0566 m	0.0527 m
	30	0.0994 m	0.0835 m	0.0755 m	0.0703 m
	$SNR_{req.,CONT} = 33.11$	-	-	-	0.0840 m

As it is more appropriate to take the threshold value of the SNR in the order of $20 \sim 30\ dB$ in practical systems, considering the results from Table 2.4 especially for the commercial Continental ARS Radar, one can conclude that the required size of the corner reflector should be $l_{min} \geq 0.0840\ m$.

2.7. Conclusions

In this chapter, the most appropriate calibration target is determined, after an evaluation among different possible calibrations targets, to be trihedral corner reflector. This evaluation is done based on the defined target selection criteria that is formed by some important desired characteristics the calibration targets need to possess.

Considering visibility and safety issues based on the geometry of a straight three-lanes European highway configuration, an appropriate position of the calibration target alongside the highway is chosen to be point T as given in figure 2.12. The formulas to compute the range of spherical incidence angles are provided to be :

- $\Delta\phi_{inc} = 90° - \zeta - \beta$,
- $\Delta\theta_{inc} = \theta_1 - \theta_2$, where

- $\theta_1 = 180^\circ - min\,\{\rho, \eta, \Psi, \omega\}$,
- $\theta_2 = 180^\circ - max\,\{\rho, \eta, \Psi, \omega\}$,

The pair of ideal spherical angles, which maximizes equation (2.10) within the appropriate interval of incidence angles, are determined to be ($\theta_{ideal} = 54.7^\circ$,$\phi_{ideal} = 45^\circ$).

The required size of the corner reflector is shown to depend on the minimum required RCS σ_{req} of the calibration target, the ideal pair of spherical incidence angles (θ_{ideal},ϕ_{ideal}) and the radial distance R at the given frequency. Considering two different references of specifications, *Recommmendation ITU-R, M.2057-0* and *Specifications Continental ARS 30X Long Range Radar*, minimum required RCS are obtained to be $\sigma_{req.,ITU} = 0.3186\ dBsm$ and $\sigma_{req.,CONT} = 11.38\ dBsm$ as well as the minimum required signal-to-noise ratio at the input of the receiver are determined to be $SNR_{req.,ITU} = 16.02\ dB$, and $SNR = 33.11dB$, respectively.

Minimum required size of the corner reflector is obtained to be $l_{min} \geq 0.0840\ m$ from the evaluation of these two references.

3

Statistical Characteristics of the RCS Loss Factor

This chapter investigates the statistical characteristics of the RCS loss in terms of *RCS Loss Factor* for orientation errors, both in elevation and azimuth plane, errors in leg length as well as the non-orthogonality of the corner walls which results from mass production errors.

3.1. RCS Loss Factor due to Orientation (Alignment) Errors

In general, the RCS loss factor due to orientation errors can be derived from the formula given in (2.10) to be:

$$L_{ori.} = \frac{\sigma_{rec.}(\theta, \phi, l)}{\sigma_{ideal}(\theta_{ideal}, \phi_{ideal}, l_{ideal})} \tag{3.1}$$

where $\sigma_{rec.}(\theta, \phi, l)$ is the received RCS reflected from the reflector under actual conditions and $\sigma_{ideal}(\theta_{ideal}, \phi_{ideal}, l_{ideal})$ is the RCS expected to be received under ideal orientation and leg length of the reflector.

3.1.1. RCS Loss Factor due to Errors in Elevation Plane

Considering equation (3.1), the RCS loss factor solely due to elevational orientation errors can be derived to be:

$$L_{elev.} = \frac{\sigma(\theta, \phi_{ideal}, l_{ideal})}{\sigma_{ideal}(\theta_{ideal}, \phi_{ideal}, l_{ideal})} \tag{3.2}$$

where,

$\sigma(\theta, \phi_{ideal}, l_{ideal})$ is the received RCS reflected from the reflector when the reflector has error in its orientation in elevation plane only, while the reflector has the ideal orientation in azimuth plane and has no errors in its leg length,

and,

$\sigma_{ideal}(\theta_{ideal}, \phi_{ideal}, l_{ideal})$ is the RCS expected to be received under ideal orientation both in elevation and azimuth planes and the leg length of the reflector has no errors. Specifically,

$$\begin{aligned} \sigma(\theta, \phi_{ideal}, l_{ideal}) \approx \frac{4\pi}{\lambda_0^2} l_{ideal}^4 [\cos\theta + \sin\theta(\sin\phi_{ideal} + \cos\phi_{ideal}) \\ -2[\cos\theta + \sin\theta(\sin\phi_{ideal} + \cos\phi_{ideal})]^{-1}]^2 \end{aligned} \tag{3.3}$$

and,

$$\begin{aligned}\sigma(\theta_{ideal}, \phi_{ideal}, l_{ideal}) \approx \frac{4\pi}{\lambda_0^2} l_{ideal}^4 [&\cos\theta_{ideal} + \sin\theta_{ideal}(\sin\phi_{ideal} + \cos\phi_{ideal}) \\ &-2[\cos\theta_{ideal} + \sin\theta_{ideal}(\sin\phi_{ideal} + \cos\phi_{ideal})]^{-1}]^2\end{aligned} \tag{3.4}$$

3.1.2. Approximation of High-Frequency RCS by its Taylor Series

First step to derive the probability distribution of the loss factor $L_{elev.}$, is to approximate the high-frequency RCS $\sigma(\theta, \phi_{ideal}, l_{ideal})$ by means of its Taylor series in the vicinity of the point $\theta = \theta_{ideal}$.

Consider equation (3.3) for the ideal azimuth incidence angle $\phi_{ideal} = 45°$ and the ideal leg length of the reflector l_{ideal} :

$$\begin{aligned}\sigma(\theta, \phi_{ideal}, l_{ideal}) \approx \frac{4\pi}{\lambda_0^2} l_{ideal}^4 [&\cos\theta + \sin\theta(\sin\phi_{ideal} + \cos\phi_{ideal}) \\ &-2[\cos\theta + \sin\theta(\sin\phi_{ideal} + \cos\phi_{ideal})]^{-1}]^2\end{aligned} \tag{3.5}$$

Since $\sin(45°) = \cos(45°) = \frac{\sqrt{2}}{2}$, this equation simplifies to :

$$\begin{aligned}&\sigma(\theta, \phi_{ideal}, l_{ideal}) \approx C\left[(\cos\theta + \sqrt{2}\sin\theta) - 2[\cos\theta + \sqrt{2}\sin\theta]^{-1}\right]^2 \\ &\text{where } C = \frac{4\pi}{\lambda_0^2} l_{ideal}^4.\end{aligned} \tag{3.6}$$

One can approximate the function $\sigma(\theta, \phi_{ideal}, l_{ideal})$ by means of ”quadratic approximation” that follows from the Taylor’s theorem.

Denote $\sigma(\theta, \phi_{ideal}, l_{ideal}) = f(\theta)$,

the quadratic approximation of the function $\sigma(\theta, \phi_{ideal}, l_{ideal})$ around the point $\theta = \theta_{ideal}$ by means of the second-order Taylor polynomial is to be given as :

$$\sigma(\theta, \phi_{ideal}, l_{ideal})\Big|_{\theta=\theta_{ideal}} \approx f(\theta_{ideal}) + \frac{d\,f(\theta)}{d\theta}\Big|_{\theta=\theta_{ideal}} (\theta - \theta_{ideal}) + \frac{1}{2!}\frac{d^2\,f(\theta)}{d^2\,\theta}\Big|_{\theta=\theta_{ideal}} (\theta - \theta_{ideal})^2 \tag{3.7}$$

The elements of the Taylor polynomial from equation (3.7) are obtained to be as follows:

$$f(\theta_{ideal}) = C\left[\cos\theta_{ideal} + \sqrt{2}\sin\theta_{ideal} - \frac{2}{\cos\theta_{ideal} + \sqrt{2}\sin\theta_{ideal}}\right]^2, \tag{3.8}$$

The first derivative $\frac{d\,f(\theta)}{d\theta}$ in equation (3.7) is obtained to be:

$$\begin{aligned}\frac{d\,f(\theta)}{d\theta} &= \frac{d\,\sigma(\theta, \phi_{ideal}, l_{ideal})}{d\theta} \\ &= 2\,C\left[(\cos\theta + \sqrt{2}\sin\theta) - 2(\cos\theta + \sqrt{2}\sin\theta)^{-1}\right] \\ &\cdot\left[(-\sin\theta + \sqrt{2}\cos\theta) + 2\,(\cos\theta + \sqrt{2}\sin\theta)^{-2}\cdot(-\sin\theta + \sqrt{2}\cos\theta)\right]\end{aligned} \tag{3.9}$$

To keep the notation short and simple, call the elements in the brackets from equation (3.9) as:

$$a(\theta) = \left[(\cos\theta + \sqrt{2}\sin\theta) - 2(\cos\theta + \sqrt{2}\sin\theta)^{-1}\right],$$

and,

$$b(\theta) = \left[\,(-\sin\theta + \sqrt{2}\cos\theta) + 2\,(\cos\theta + \sqrt{2}\sin\theta)^{-2} \cdot (-\sin\theta + \sqrt{2}\cos\theta)\right],$$

Therefore, the first derivative can be re-written simplified as:

$$\frac{d\,f(\theta)}{d\theta} = 2\,C\left[a(\theta) \cdot b(\theta)\right] \tag{3.10}$$

Note that, actually, $b(\theta) = \frac{d\,a(\theta)}{d\theta}$.

Now, from equation 3.10, using the product rule, the second derivative $\frac{d^2\,f(\theta)}{d^2\,\theta}$ can be obtained to be:

$$\frac{d^2\,f(\theta)}{d^2\,\theta} = 2\,C\left[\frac{d\,a(\theta)}{d\theta} \cdot b(\theta) + a(\theta) \cdot \frac{d\,b(\theta)}{d\theta}\right] \tag{3.11}$$

Note that since $b(\theta) = \frac{d\,a(\theta)}{d\theta}$, actually, $\frac{d\,b(\theta)}{d\theta} = \frac{d^2\,a(\theta)}{d^2\theta}$.

Therefore, the second derivative can be re-written as:

$$\frac{d^2\,f(\theta)}{d^2\,\theta} = 2\,C\left[b^2(\theta) + a(\theta) \cdot \frac{d^2 a(\theta)}{d^2\theta}\right] \tag{3.12}$$

Again using the product rule for the element in the right-half side after "+"-sign in the bracket assigned to $b(\theta)$, *i.e. for* $2\,(\cos\theta + \sqrt{2}\sin\theta)^{-2} \cdot (-\sin\theta + \sqrt{2}\cos\theta)$, the derivative becomes:

$$\begin{aligned}\frac{d^2\,a(\theta)}{d^2\theta} &= \frac{d\,b(\theta)}{d\theta}\\ &= (-\cos\theta - \sqrt{2}\sin\theta)\ +\\ &\left[-4(\cos\theta + \sqrt{2}\sin\theta)^{-3} \cdot (-\sin\theta + \sqrt{2}\cos\theta)^2 + 2(\cos\theta + \sqrt{2}\sin\theta)^{-2} \cdot (-\cos\theta - \sqrt{2}\sin\theta)\right]\end{aligned} \tag{3.13}$$

Since the element $\left.\frac{d\,f(\theta)}{d\theta}\right|_{\theta=\theta_{ideal}}$ in equation (3.7) stands for the derivative of the function $\sigma(\theta, \phi_{ideal}, l_{ideal})$ at the point $\theta = \theta_{ideal}$, at which point the high-frequency RCS from equation(2.2) has its maximum value, this element should equal to zero, i.e. $\left.\frac{d\,f(\theta)}{d\theta}\right|_{\theta=\theta_{ideal}} = 0$.

One of the solutions to the equation $\left.\frac{d\,f(\theta)}{d\theta}\right|_{\theta=\theta_{ideal}} = 0$ by solving it analytically is:

$$\theta = 2\left(\pi n + \tan^{-1}\left(\frac{1}{2}(\sqrt{6} - \sqrt{2})\right)\right),\ \ n \in \mathbb{Z} \tag{3.14}$$

which, for $n = 0$, results in $\theta \approx 0.955317\,rad = 54.74° = \theta_{ideal}$. This is represented in figure 3.1.

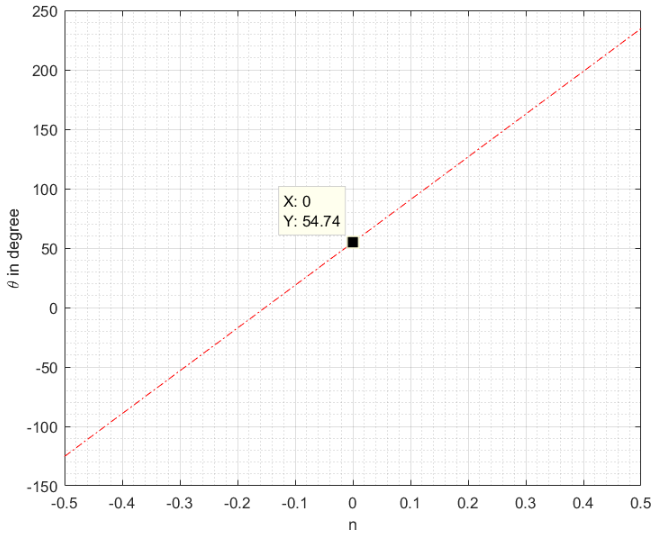

Figure 3.1: Solution from equation (3.14) as a function of n.

Also from figure 3.2 can be seen that, numerically, the derivative goes to zero around $\theta = \theta_{ideal} \approx 54.74°$.

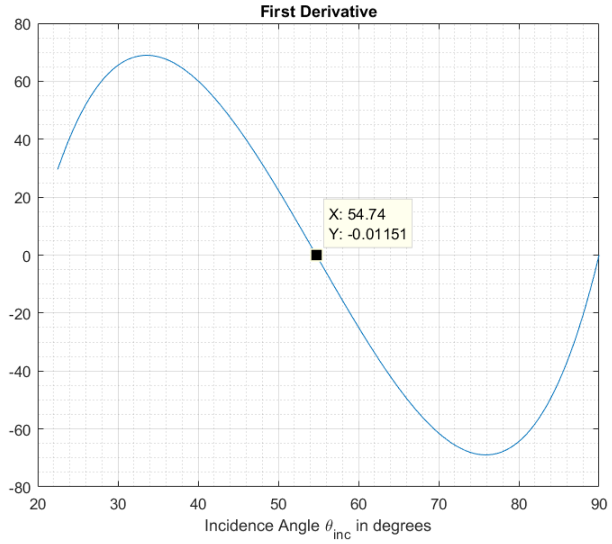

Figure 3.2: Derivative of the function $\sigma(\theta, \phi_{ideal}, l_{ideal})$ as a function of incident angle $\theta_{inc.}$.

Therefore, the Taylor polynomial from equation (3.7) simplifies to:

$$\sigma(\theta, \phi_{ideal}, l_{ideal})\Big|_{\theta=\theta_{ideal}} \approx f(\theta_{ideal}) + \frac{1}{2}\,\frac{d^2\, f(\theta)}{d^2\ \theta}\Big|_{\theta=\theta_{ideal}} (\theta - \theta_{ideal})^2 \tag{3.15}$$

which after filling in for the corresponding elements results into the following approximation:

$$\begin{aligned}\sigma(\theta, \phi_{ideal}, l_{ideal})\Big|_{\theta=\theta_{ideal}} \approx\ & C\left[\cos\theta_{ideal} + \sqrt{2}\sin\theta_{ideal} - \frac{2}{\cos\theta_{ideal} + \sqrt{2}\sin\theta_{ideal}}\right]^2 + \\ & C\left[b^2(\theta_{ideal}) + a(\theta_{ideal}) \cdot \frac{d^2 a(\theta)}{d^2\theta}\Big|_{\theta=\theta_{ideal}}\right](\theta - \theta_{ideal})^2\end{aligned} \tag{3.16}$$

Having approximated the high-frequency RCS $\sigma(\theta, \phi_{ideal}, l_{ideal})$ by means of its Taylor series in the vicinity of the point $\theta = \theta_{ideal}$ to be as given in equation (3.16), the loss factor $L_{elev.}$ takes finally the form :

$$L_{elev.} \approx \frac{\sigma(\theta, \phi_{ideal}, l_{ideal})\Big|_{\theta=\theta_{ideal}}}{\sigma_{ideal}(\theta_{ideal}, \phi_{ideal}, l_{ideal})} = 1 - N\,(\theta - \theta_{ideal})^2, \tag{3.17}$$

in which the factor N is simply obtained to be:

$$N = \frac{1}{2}\,\frac{d^2\,f(\theta)}{d^2\,\theta}\Big|_{\theta=\theta_{ideal}} \cdot \frac{1}{f(\theta_{ideal})} \tag{3.18}$$

Filling in for the elements of N into equation (3.17) gives that:

$$\begin{aligned} L_{elev.} &\approx 1 - \frac{1}{2}\,2\,C\left[b^2(\theta_{ideal}) + a(\theta_{ideal}) \cdot \frac{d^2a(\theta)}{d^2\theta}\Big|_{\theta=\theta_{ideal}}\right] \cdot \\ &\quad \frac{1}{C\left[\cos\theta_{ideal} + \sqrt{2}\sin\theta_{ideal} - \frac{2}{\cos\theta_{ideal}+\sqrt{2}\sin\theta_{ideal}}\right]^2}\,(\theta - \theta_{ideal})^2 \\ &\approx 1 - \frac{\left[b^2(\theta_{ideal}) + a(\theta_{ideal}) \cdot \frac{d^2a(\theta)}{d^2\theta}\Big|_{\theta=\theta_{ideal}}\right]}{\left[\cos\theta_{ideal} + \sqrt{2}\sin\theta_{ideal} - \frac{2}{\cos\theta_{ideal}+\sqrt{2}\sin\theta_{ideal}}\right]^2}\,(\theta - \theta_{ideal})^2 \end{aligned} \tag{3.19}$$

Equation (3.19) shows that the error $L_{elev.}$ does not depend on the parameters λ_0 and l_{ideal} of the corner reflector. For the pair of spherical incidence angles ($\theta_{ideal} = 54.7^\circ, \phi_{ideal} = 45^\circ$), the factor $N \approx 5.0$.

Figure 3.3 below gives the obtained Taylor approximation versus the original function of the high-frequency RCS.

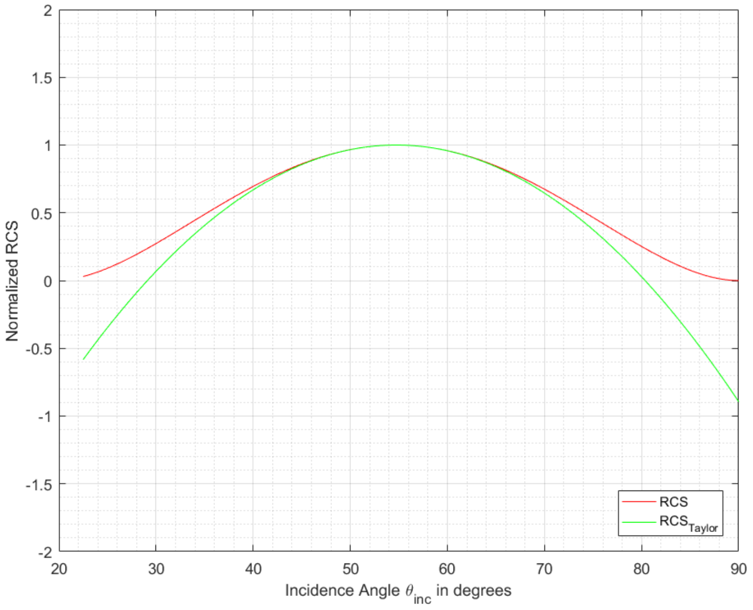

Figure 3.3: Original high-frequency RCS function vs. its Taylor approximation

3.1.3. Analytical Derivation of the Probability Distribution of the Loss Factor $L_{elev.}$

Deviations from the ideal orientation in elevation plane can be assumed to be normal distributed with mean θ_{ideal} and variance σ_θ^2. Therefore, the probability distribution of the incident elevation angle θ can be given by $\theta \sim N(\theta_{ideal}, \sigma_\theta^2)$:

$$p_1(\theta) = \frac{1}{\sqrt{2\pi}\sigma_\theta} \, exp\left(- \frac{(\theta - \theta_{ideal})^2}{2\sigma_\theta^2} \right) \tag{3.20}$$

Having determined the formula of the loss factor in equation (3.17) approximately to be:

$$L_{elev.} \approx 1 - N\,(\theta - \theta_{ideal})^2, \tag{3.21}$$

the probability distribution of the loss factor $L_{elev.}$ can be derived by means of "Transformation of Random Variables" from the probability distribution $p_1(\theta)$ of elevation incidence angle θ from equation (3.20). Therefore, the probability distribution of the loss factor $L_{elev.}$ is:

$$p(L_{elev.}) = 2\, p_1(\theta(L_{elev.})) \left| \frac{d\theta}{dL_{elev.}} \right| \tag{3.22}$$

where the factor 2 comes from the even symmetry of the function in equation (3.21), and,

$$\theta(L_{elev.}) = \theta_{ideal} + \left[\frac{1}{N}(1 - L_{elev}) \right]^{1/2} \tag{3.23}$$

is the inverse function that follows from equation (3.21), and the derivative of this inverse function is:

$$\frac{d\theta(L_{elev.})}{dL_{elev.}} = \frac{1}{2}\left[\frac{1}{N}(1 - L_{elev}) \right]^{-1/2} \cdot -\frac{1}{N} \tag{3.24}$$

which gives,

$$\left| \frac{d\theta(L_{elev.})}{dL_{elev.}} \right| = \frac{1}{2N}\left[\frac{1}{N}(1 - L_{elev}) \right]^{-1/2} \tag{3.25}$$

and,

$$p_1(\theta(L_{elev.})) = \frac{1}{\sqrt{2\pi}\sigma_\theta}\ exp\Big(-\frac{\frac{1}{N}(1-L_{elev.})}{2\sigma_\theta^2}\Big). \tag{3.26}$$

Finally, putting the pieces together according to equation (3.22), the probability distribution of the loss factor $L_{elev.}$ is obtained analytically to be:

$$p(L_{elev.}) = \frac{1}{(\frac{1}{N})^{-1/2}\sqrt{2\pi}\sigma_\theta}(1-L_{elev})^{-1/2}\ exp\Big(-\frac{\frac{1}{N}(1-L_{elev.})}{2\sigma_\theta^2}\Big) \tag{3.27}$$

Next, equation (3.27) can be approximated by β-distribution for small error in elevation orientation. For small error in orientation, i.e. $(\theta-\theta_{ideal}) \approx 0$ in equation (3.21), the loss factor $L_{elev}. \approx 1$.

Furthermore, the following factor from equation (3.27) can be re-written as:

$$exp\Big(-\frac{\frac{1}{N}(1-L_{elev.})}{2\sigma_\theta^2}\Big) = \Big[exp\ (1-L_{elev.})\Big]^{\frac{-1}{2N\sigma_\theta^2}} = \Big[exp\ (L_{elev.}-1)\Big]^{\frac{1}{2N\sigma_\theta^2}} \tag{3.28}$$

Denote $exp\ (L_{elev.}-1) = f(y)$, the Taylor expansion of $f(y)$ around the point $L_{elev.,0} \approx 1$ follows as:

$$f(y)\Big|_{L_{elev.}=L_{elev.,0}} \approx f(L_{elev.,0}) + \frac{d\,f(L_{elev.})}{dL_{elev.}}\Big|_{L_{elev.}=L_{elev.,0}}(L_{elev.}-L_{elev.,0}) \tag{3.29}$$

The elements of the Taylor polynomial from equation (3.29) can be obtained to be:

$$f(L_{elev.,0}) \approx exp\ (L_{elev.,0}-1) = exp\ (0) = 1 \tag{3.30}$$

$$\frac{d\,f(L_{elev.})}{dL_{elev.}}\Big|_{L_{elev.}=L_{elev.,0}} \approx exp\ (L_{elev.,0}-1) = exp\ (0) = 1 \tag{3.31}$$

which after filling into equation 3.29 results in:

$$exp\ (L_{elev.}-1)\Big|_{L_{elev.}=L_{elev.,0}} \approx L_{elev.}. \tag{3.32}$$

Therefore,

$$exp\Big(-\frac{\frac{1}{N}(1-L_{elev.})}{2\sigma_\theta^2}\Big) = \Big[exp\ (L_{elev.}-1)\Big]^{1/2N\sigma_\theta^2}\Big|_{L_{elev.}=L_{elev.,0}} \approx L_{elev.}^{1/2N\sigma_\theta^2} \tag{3.33}$$

Using this approximation in (3.27) gives:

$$p_\beta(L_{elev.}) \approx \frac{1}{(\frac{1}{N})^{-1/2}\sqrt{2\pi}\sigma_\theta}(1-L_{elev})^{-1/2}\ L_{elev.}^{1/2N\sigma_\theta^2} \tag{3.34}$$

which has the form of β-distribution pdf with the shape parameters:

$$\alpha = \frac{1}{2N\sigma_\theta^2}+1 \tag{3.35}$$

$$\beta = \frac{1}{2} \tag{3.36}$$

However, this pdf is subject to normalization to satisfy the rule that $\int_0^1 p_\beta(L_{elev.})\ dL_{elev.} = 1$. It is notable that the error in orientation affects only the parameter α of the distribution, in which $\beta = 0.5$ is a fixed value. Below in figure's 3.4a and 3.4b, an example of the PDF's from (3.27) and (3.34) is given for $\sigma_\theta = 1.25°$, $\sigma_\theta = 1.05°$,$\sigma_\theta = 0.85°$ and $N = 5.0$, which was obtained before from equation (3.17) for the pair of spherical incidence angles ($\theta_{ideal} = 54.7°, \phi_{ideal} = 45°$).

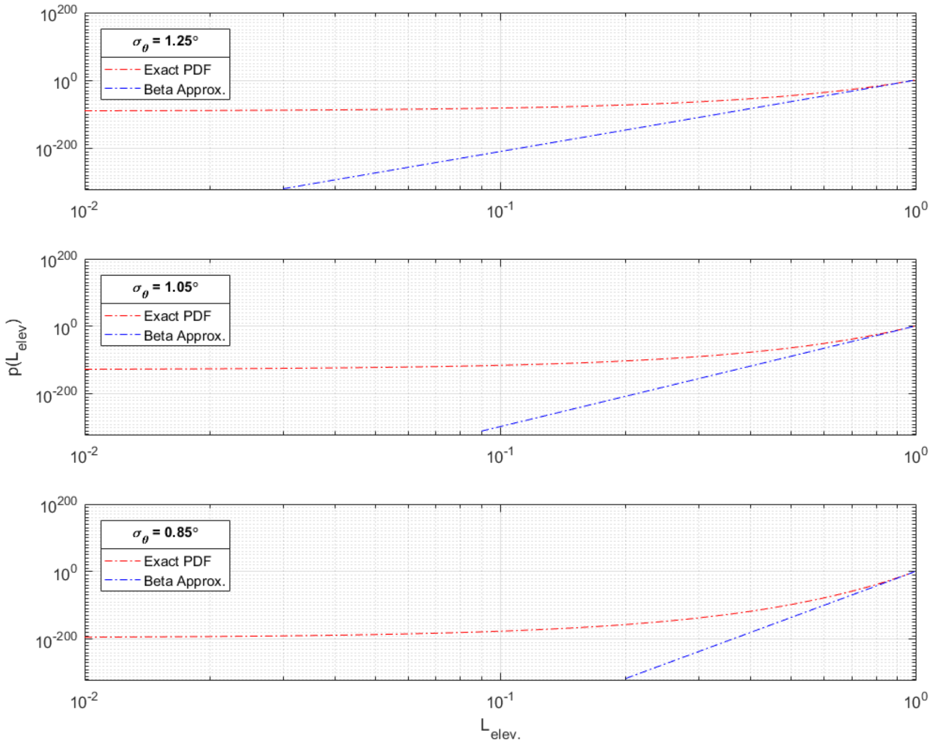

(a) Both x- and y-axis in logarithmic scale.

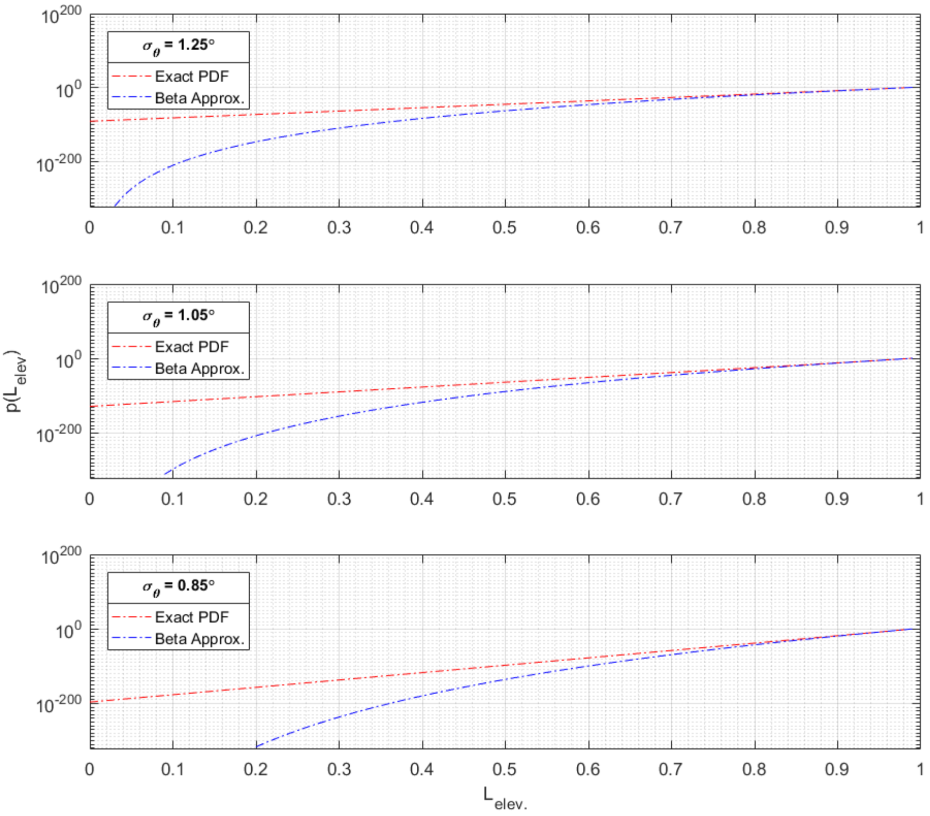

(b) y-axis in logarithmic scale only.

Figure 3.4: Exact PDF vs. its β-distribution approximation for different values of the standard deviation σ_θ for $N = 5.0$.

Additionally, figure 3.5 below represents the shape parameters obtained from the derived β-distribution alongside the shape parameters obtained from the Monte-Carlo simulation performed for n=10000 realizations of targets evaluated at $f = 77\ GHz$.

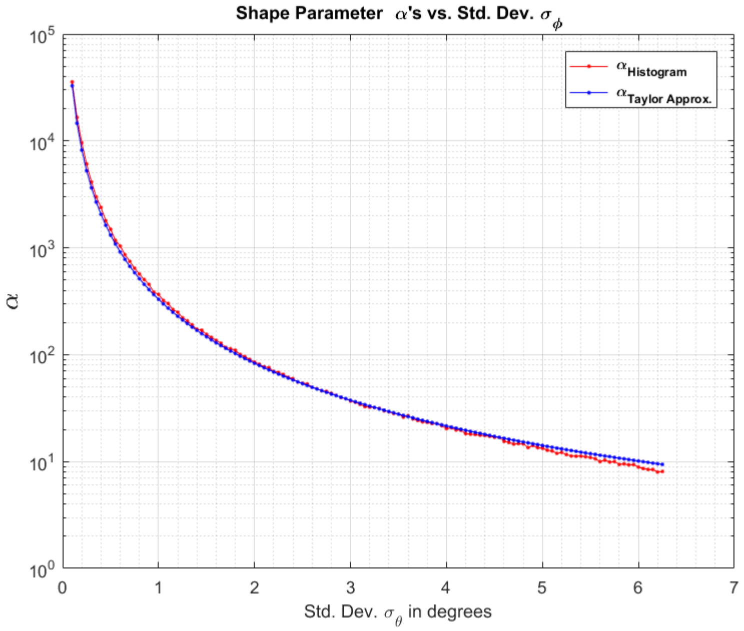

Figure 3.5: Shape parameters $\alpha_{Histogram}$ from simulations vs. the obtained ones from the β-distribution approximation.

From both figures one can conclude that the plots agree quite well with each other which means that the approximation made above is applicable.

3.1.4. Validation of the Analytical Results by Kullback-Leibler Divergence

The analytical results in this chapter were derived as given in the following order:

1. Starting with the high-frequency RCS $\sigma(\theta, \phi_{ideal}, l_{ideal})$ as the function of angle θ as given in (3.3).
2. This high-frequency RCS is approximated in the vicinity of the maximum, where $\theta = \theta_{ideal}$, by the parabola given in equation (3.16). This has led to the pdf $p(L_{elev.})$ given in equation (3.27).
3. Demonstrated that (3.27) can be approximated well by a known β-distribution, $p_\beta(L_{elev.})$, with certain shape parameters (α, β) as given in equation (3.34).

By means of Kullback-Leibler divergence, it can be shown how the distribution $p_\beta(L_{elev.})$ is different from the distribution of $p(L_{elev.})$. With other words, Kullback-Leibler divergence here is a metric of how well the β-distribution approximation fit the exact distribution in equation (3.27).
Additionally, also the Kullback-Leibler divergence between the Monte Carlo simulation results and the analytically derived probability distributions are considered below.

Kullback-Leibler Divergence Between $p(L_{elev.})$ and $p_\beta(L_{elev.})$

As since for distributions of continuous random variables, the Kullback-Leibler divergence between $p(L_{elev.})$ and its β-approximation $p_\beta(L_{elev.})$ is defined to be the integral:

$$D_{KL}\left(P \,||\, P_\beta\right) = \int p(L_{elev})\, log\left(\frac{p(L_{elev})}{p_\beta(L_{elev})}\right) dL_{elev} \tag{3.37}$$

which can also be written as the following summation:

$$D_{KL}\left(P \,||\, P_\beta\right) = \sum_{i=1}^{m} p(L_{elev,i})\, log\left(\frac{p(L_{elev,i})}{p_\beta(L_{elev,i})}\right) \delta L_{elev} \tag{3.38}$$

where $p(L_{elev,i}) = p(\delta L_{elev} \cdot i)$, $p_\beta(L_{elev,i}) = p_\beta(\delta L_{elev} \cdot i)$ and $\delta L_{elev} = \frac{1}{m}$ since $L_{elev} \in [0, 1]$.

Figure 3.6 below shows the KL-Divergence between $p(L_{elev.})$ and $p_\beta(L_{elev.})$ as a function of σ_θ for both with and without normalization of $p_\beta(L_{elev})$. Results in the figure are for $n = 10000$ realizations and $\delta L_{elev} = 1e-4$, where the factor $N = 5.0$ as it was determined earlier that for the pair of spherical incidence angles ($\theta_{ideal} = 54.7°, \phi_{ideal} = 45°$), the factor is $N \approx 5.0$.

As expected, with normalization of the pdf $p_\beta(L_{elev.})$, the divergence is very low for small errors in orientation in terms of σ_θ-values and it gets higher for bigger errors in orientation. This justifies the correctness of transition from step 2 to step 3. Therefore the β-approximation made here is applicable and it is validated. Moreover, the divergence becomes much bigger even for relatively small errors in orientation when the pdf $p_\beta(L_{elev.})$ is not normalized as expected.

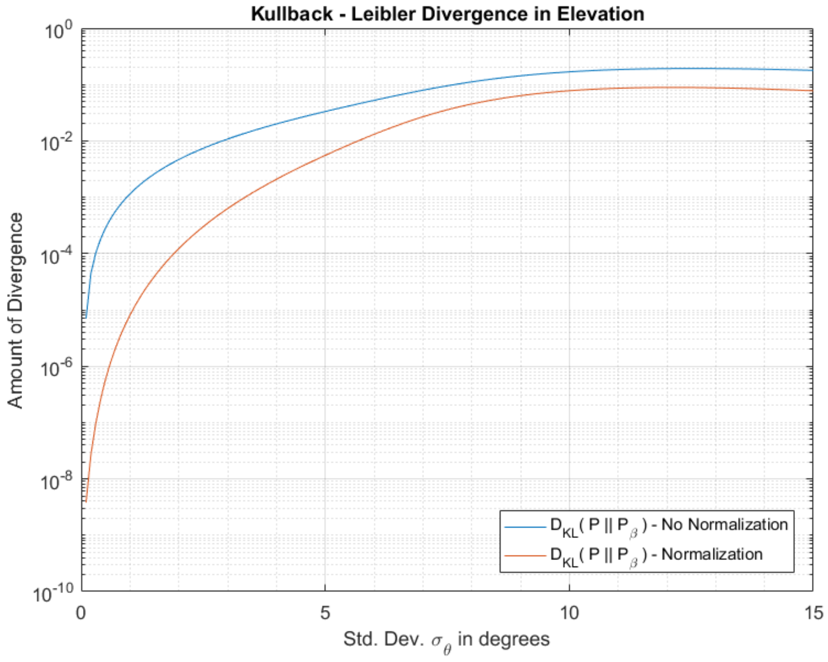

Figure 3.6: KL-Divergence between $p(L_{elev.})$ and $p_\beta(L_{elev.})$ as a function of σ_θ with and without normalization of $p_\beta(L_{elev.})$

Kullback-Leibler Divergence Between $p_{sim}(L_{elev.})$ From MC Simulation and Analytically Derived Probability Distributions $p(L_{elev.})$ and $p_{\beta}(L_{elev.})$

The Kullback-Leibler divergence between $p_{sim}(L_{elev.})$ that is gained from the Monte Carlo simulation and the analytically derived probability distribution $p(L_{elev.})$ can be written as:

$$D_{KL}\left(P_{sim} \,||\, P\right) = \sum_{i=1}^{m} p_{sim}(L_{elev,i})\, log\left(\frac{p_{sim}(L_{elev,i})}{p(L_{elev,i})}\right)\delta L_{elev.} \tag{3.39}$$

and similarly,

the Kullback-Leibler divergence between $p_{sim}(L_{elev.})$ gained from the Monte Carlo simulation and the analytically derived β-approximated probability distribution $p_{\beta}(L_{elev.})$ can be written as:

$$D_{KL}\left(P_{sim} \,||\, P_{\beta}\right) = \sum_{i=1}^{m} p_{sim}(L_{elev,i})\, log\left(\frac{p_{sim}(L_{elev,i})}{p_{\beta}(L_{elev,i})}\right)\delta L_{elev.} \tag{3.40}$$

Figure 3.7 below shows the Kullback-Leibler divergence plot between $p_{sim}(L_{elev.})$ obtained from the Monte-Carlo simulation and the analytically derived pdf's of $p(L_{elev.})$ and $p_{\beta}(L_{elev.})$ as a function of σ_{θ} for $n = 10000$ realizations of the target and $\delta L_{elev} = 1e-4$ for the leg size of $l = 0.10\ m$ at $f = 77GHz$ for the ideal spherical incidence angles ($\theta_{ideal} = 54.7°, \phi_{ideal} = 45°$). Note that the pdf $p_{\beta}(L_{elev.})$ is normalized in the computations here.

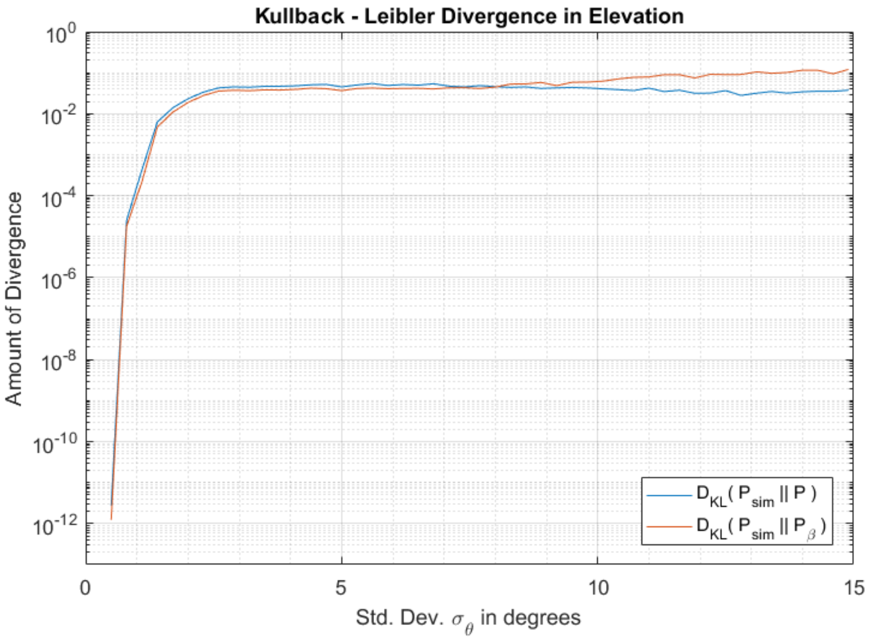

Figure 3.7: Kullback-Leibler Divergence results between $p_{sim}(L_{elev.})$ and the probability distributions $p(L_{elev.})$ and $p_{\beta}(L_{elev.})$ as a function of σ_{θ}.

From both Kullback-Leibler divergence plots in the figure can be concluded that for small errors in orientation in terms of σ_{θ}-values, the divergence is much smaller than for bigger errors in orientation. Particularly the Kullback-Leibler divergence plot $D_{KL}\left(P_{sim} \,||\, P\right)$ justifies the correctness of transition from step 1 to step 2 by which the approximation of the high-frequency RCS in the vicinity of the maximum is validated. Also, the Kullback-Leibler divergence plot $D_{KL}\left(P_{sim} \,||\, P_{\beta}\right)$ justifies the correctness of transition from step 1 through step 3.

3.1.5. Beta Distribution Fit on the Distribution of RCS Loss Factor $L_{elev.}$

Beta distribution is a family of continuous probability distributions which are defined on the interval [0,1]. Furthermore, a beta distribution is parametrized by two positive shape parameters α and β. If X is a random variable with beta distribution $Beta(\alpha, \beta)$, the pdf of X, for $0 \leq x \leq 1$ and $\alpha, \beta > 0$, is given as :

$$p(x) = \frac{x^{\alpha-1}(1-x)^{\beta-1}}{B(\alpha, \beta)}, \tag{3.41}$$

where $B(\alpha, \beta)$ is the Beta function.

The error in the elevation orientation is assumed to be normally distributed with the mean value of $E(\theta) = \theta_{ideal}$ and standard deviation of $\sigma_\theta = 1.25°$, i.e. $\theta \sim N(\theta_{ideal}, \sigma_\theta^2)$.

Figure 3.8 gives the result of the beta distribution fit, that is obtained for n=10000 targets evaluated at $f = 77\ GHz$, on the histogram of the loss factor for the ideal leg length $l_{ideal} = 0.10\ m$ and ideal azimuthal incidence angle ϕ_{ideal}. The corresponding shape parameters for this beta distribution are estimated to be $\alpha = 228.29$ and $\beta = 0.546$.

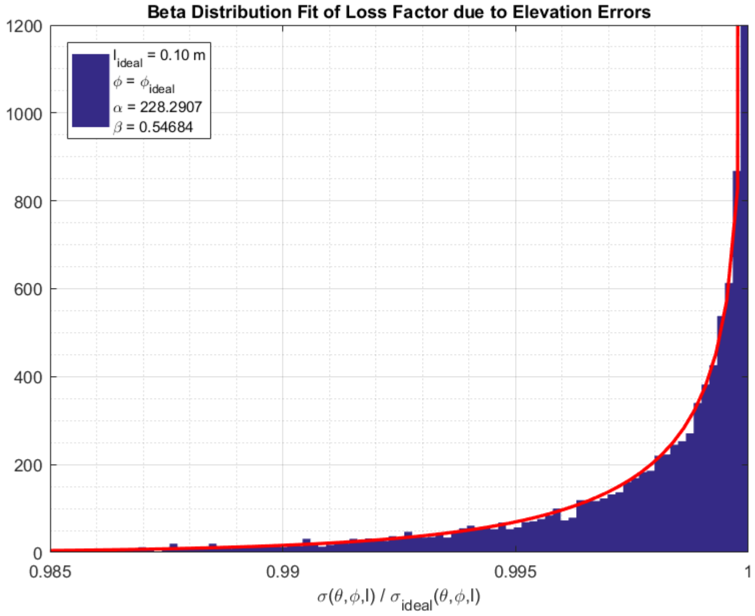

Figure 3.8: Beta distribution fit of the loss factor in RCS due to orientation errors in elevation plane.

Additionally, figure 3.9 gives the results of the beta distribution fit for the ideal leg length l_{ideal} and ideal azimuthal incidence angle ϕ_{ideal} for different variances of $\sigma^2_{\theta,1} > \sigma^2_{\theta,2} > \sigma^2_{\theta,3}$. As expected, as the variance gets smaller, the beta distribution gets narrower which means the loss factor $L_{elev.}$ gets closer to the unity.

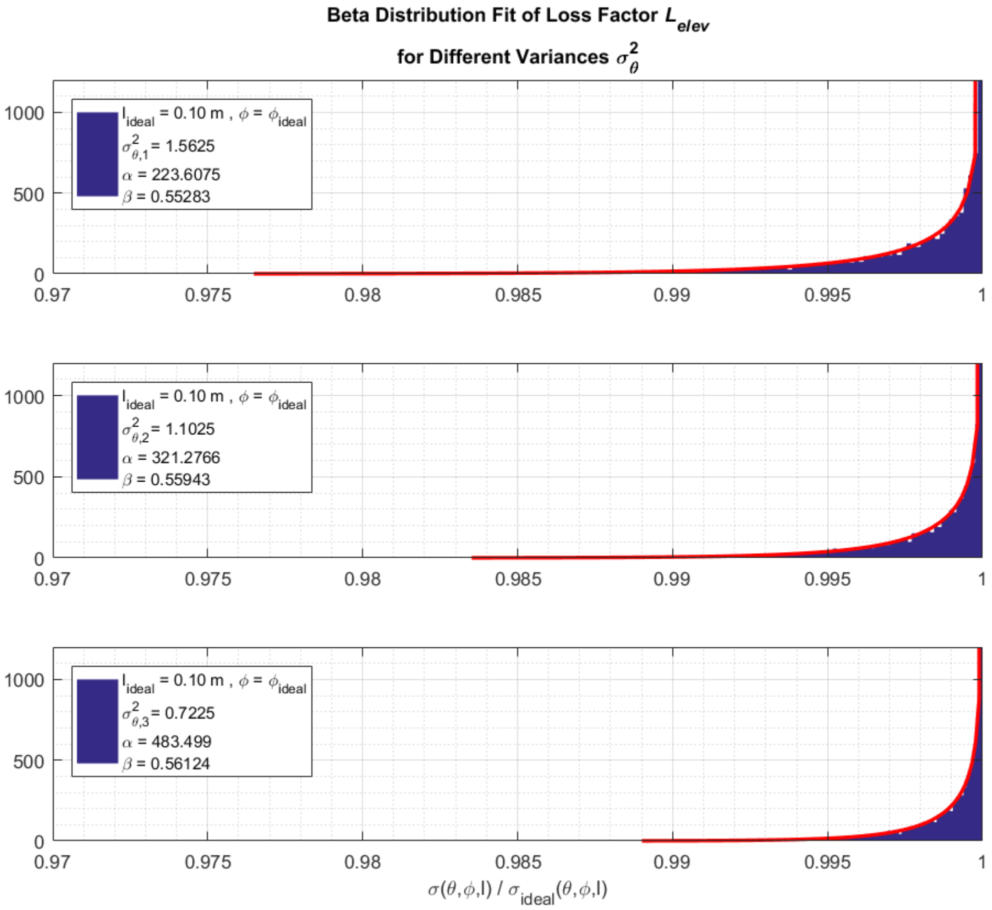

Figure 3.9: Beta distribution fit of the loss factors in RCS due to orientation errors in elevation plane for different variances of $\sigma^2_{\theta,1} > \sigma^2_{\theta,2} > \sigma^2_{\theta,3}$.

3.2. RCS Loss Factor due to Errors in Azimuth Plane

Considering equation (3.1), the RCS loss factor solely due to azimuthal orientation errors is :

$$L_{azi.} = \frac{\sigma(\theta_{ideal}, \phi, l_{ideal})}{\sigma_{ideal}(\theta_{ideal}, \phi_{ideal}, l_{ideal})} \tag{3.42}$$

3.2.1. Approximation of High-Frequency RCS by its Taylor Series

Following the same steps as in the previous section, the Taylor polynomial of high-frequency RCS at the point $\phi = \phi_{ideal}$ is obtained to be approximately:

$$\sigma(\theta_{ideal}, \phi, l_{ideal})\Big|_{\phi=\phi_{ideal}} \approx C\Big[(a + b\,(\sin\phi_{ideal} + \cos\phi_{ideal})) - \frac{2}{(a + b\,(\sin\phi_{ideal} + \cos\phi_{ideal}))}\Big]^2 + C\left[t^2(\phi_{ideal}) + s(\phi_{ideal}) \cdot \frac{d^2 s(\phi)}{d^2\phi}\Big|_{\phi=\phi_{ideal}}\right](\phi - \phi_{ideal})^2 \tag{3.43}$$

where,

$C = \frac{4\pi}{\lambda_0^2} l^4_{ideal}$,

$$a = \cos(54.7°),$$

$$b = \sin(54.7°),$$

$$s(\phi) = \Big[(a + b\ (\sin\phi + \cos\phi)) - 2(a + b\ (\sin\phi + \cos\phi))^{-1}\Big],$$

and,

$$t(\phi) = \Big[b\ (\cos\phi - \sin\phi) + 2\ (a + b\ (\sin\phi + \cos\phi))^{-2} \cdot\ b\ (\cos\phi - \sin\phi)\Big].$$

Having approximated the high-frequency RCS $\sigma(\theta_{ideal}, \phi, l_{ideal})$ by means of its Taylor series at the point $\phi = \phi_{ideal}$ as given in equation (3.43), the loss factor $L_{azi.}$ takes the form :

$$L_{azi.} \approx \frac{\sigma(\theta_{ideal}, \phi, l_{ideal})\Big|_{\phi=\phi_{ideal}}}{\sigma_{ideal}(\theta_{ideal}, \phi_{ideal}, l_{ideal})} = 1 - K\ (\phi - \phi_{ideal})^2. \tag{3.44}$$

in which the factor K is simply obtained to be:

$$K = \frac{\Big[t^2(\phi) + s(\phi) \cdot \frac{d^2 s(\phi)}{d^2\phi}\Big|_{\phi=\phi_{ideal}}\Big]}{\Big[(a + b\ (\sin\phi_{ideal} + \cos\phi_{ideal})) - \frac{2}{(a+b\ (\sin\phi_{ideal}+\cos\phi_{ideal}))}\Big]^2} \tag{3.45}$$

Equation (3.44) shows that the error $L_{azi.}$ does not depend on the parameters λ_0 and l_{ideal} of the corner reflector. For the pair of spherical incidence angles ($\theta_{ideal} = 54.7°, \phi_{ideal} = 45°$), the factor $K \approx 3.33$.

Figure 3.10 below gives the obtained Taylor approximation versus the original function of the high-frequency RCS.

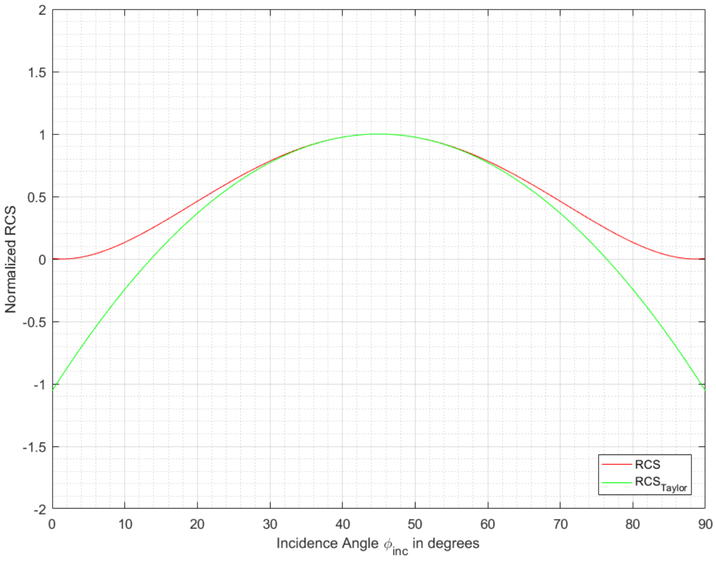

Figure 3.10: Original high-frequency RCS function vs. its Taylor approximation

3.2.2. Analytical Derivation of the Probability Distribution of the Loss Factor $L_{azi.}$

Deviations from the ideal orientation in azimuth plane are assumed to be normal distributed with mean ϕ_{ideal} and variance σ_ϕ^2. Therefore, the probability distribution of the incident azimuth angle ϕ can be given by $\phi \sim N(\phi_{ideal}, \sigma_\phi^2)$:

$$p_1(\phi) = \frac{1}{\sqrt{2\pi}\sigma_\phi} exp\Bigg(- \frac{(\phi - \phi_{ideal})^2}{2\sigma_\phi^2}\Bigg) \tag{3.46}$$

Having determined the formula of the loss factor before in equation (3.44), following the same steps as in the previous chapter, the probability distribution of the loss factor $L_{azi.}$ is obtained analytically to be:

$$p(L_{azi.}) = \frac{1}{(\frac{1}{K})^{-1/2}\sqrt{2\pi}\sigma_\phi}(1 - L_{azi.})^{-1/2}\, exp\Bigg(- \frac{\frac{1}{K}(1 - L_{azi.})}{2\sigma_\phi^2}\Bigg) \tag{3.47}$$

which can be approximated by β-distribution for small error in azimuth orientation.

Again following the same kind of approximations in (3.47) as done in the previous chapter in elevation plane gives:

$$p_\beta(L_{azi.}) \approx \frac{1}{(\frac{1}{K})^{-1/2}\sqrt{2\pi}\sigma_\phi}(1 - L_{azi})^{-1/2}\, L_{azi.}^{1/2K\sigma_\phi^2} \tag{3.48}$$

which has the form of β-distribution pdf with the shape parameters:

$$\alpha = \frac{1}{2K\,\sigma_\phi^2} + 1, \tag{3.49}$$

$$\beta = \frac{1}{2}. \tag{3.50}$$

However, this pdf is also subject to normalization to satisfy the rule that $\int_0^1 p_\beta(L_{azi.})\, dL_{azi.} = 1$. It is notable that the error in orientation affects only the parameter α of the distribution, in which $\beta = 0.5$ is a fixed value as in the previous chapter in elevation plane.

Below in figures 3.11a and 3.11b, an example of the PDF's from (3.47) and (3.48) is given for $\sigma_\phi = 6.2850°$, $\sigma_\phi = 2.2850°$, $\sigma_\phi = 1.2850°$ and $K = 3.33$, which was obtained before from equation (3.44) for the pair of spherical incidence angles ($\theta_{ideal} = 54.7°, \phi_{ideal} = 45°$).

Additionally, figure 3.12 below represents the shape parameters obtained from the derived β-distribution alongside the shape parameters obtained from the Monte-Carlo simulation performed for n=10000 realizations of targets evaluated at $f = 77\ GHz$.

From both figures can be concluded that the plots agree quite well with each other which means that the approximation made above is applicable.

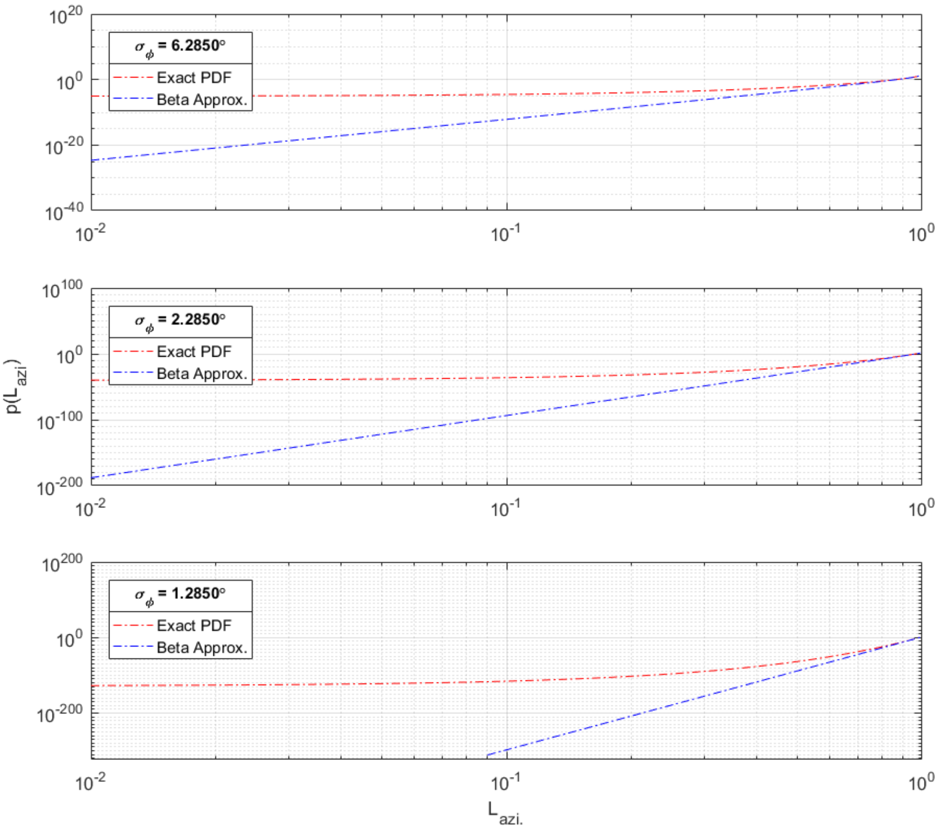

(a) Both x- and y-axis in logarithmic scale.

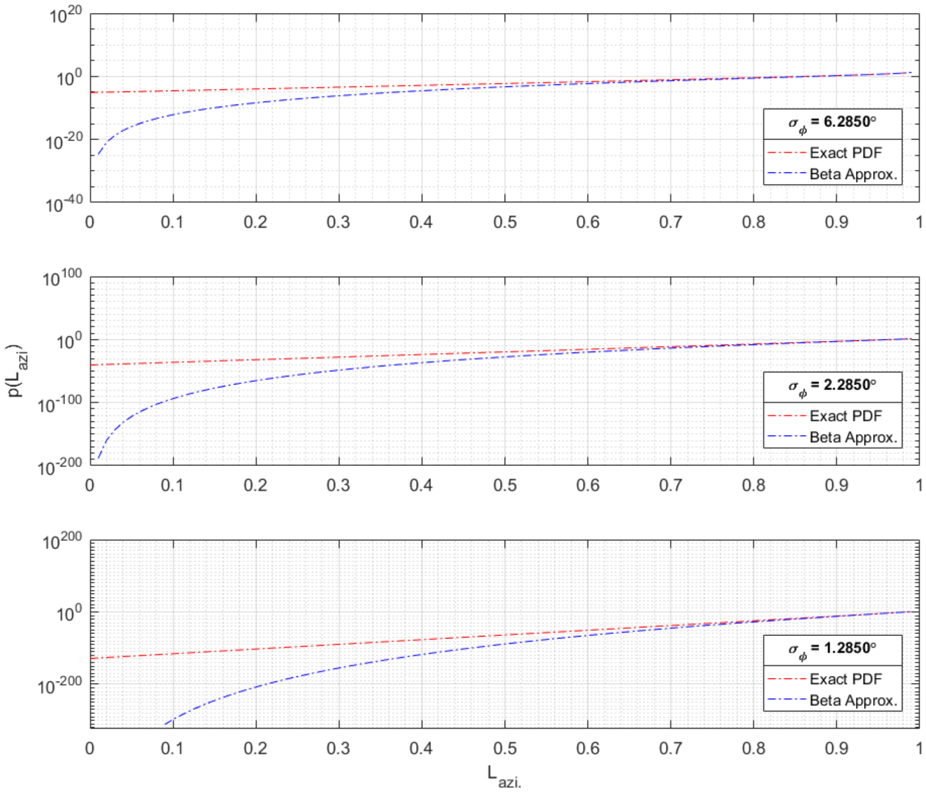

(b) y-axis in logarithmic scale only.

Figure 3.11: Exact PDF vs. its β-distribution approximation for different values of the standard deviation σ_ϕ for $K = 3.33$.

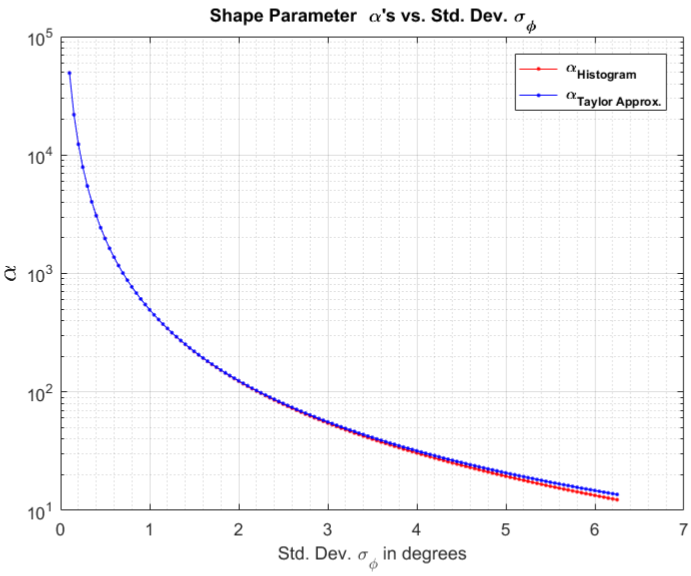

Figure 3.12: Shape parameters $\alpha_{Histogram}$ from simulations vs. the obtained ones from the β-distribution approximation.

3.2.3. Validation of the Analytical Results by Kullback-Leibler Divergence

Analytical results in this section are derived in the same order as listed in section 3.1.4, but now considering the azimuth plane.

How the distribution $p_\beta(L_{azi.})$ is different from the distribution of $p(L_{azi.})$ is shown below by means of Kullback-Leibler divergence. Additionally, also the Kullback-Leibler divergence between the Monte Carlo simulation results and the analytically derived probability distributions are considered.

Kullback-Leibler Divergence Between $p(L_{azi.})$ and $p_\beta(L_{azi.})$

The Kullback-Leibler divergence between $p(L_{azi.})$ and its β-approximation $p_\beta(L_{azi.})$ can be written as the following summation:

$$D_{KL}\left(P\,||\,P_\beta\right) = \sum_{i=1}^{m} p(L_{azi,i})\ log\left(\frac{p(L_{azi,i})}{p_\beta(L_{azi,i})}\right)\delta L_{azi.} \tag{3.51}$$

Figure 3.13 below shows the KL-Divergence between $p(L_{azi.})$ and $p_\beta(L_{azi.})$ as a function of σ_ϕ for both with and without normalization of $p_\beta(L_{azi.})$. Results in the figure are for $n = 10000$ realizations and $\delta L_{azi} = 1e-4$ where the factor $K = 3.33$ as it was determined earlier that for the pair of spherical incidence angles $(\theta_{ideal} = 54.7°, \phi_{ideal} = 45°)$, the factor is $K \approx 3.33$.

As expected, with normalization of the pdf $p_\beta(L_{azi.})$, the divergence is very low for small errors in orientation in terms of σ_ϕ-values and it gets higher for bigger errors in orientation. This justifies the correctness of transition from step 2 to step 3 and therefore the β-approximation made here is applicable and it is validated. Moreover, the divergence becomes much bigger even for small errors in orientation when the pdf $p_\beta(L_{azi.})$ is not normalized as expected.

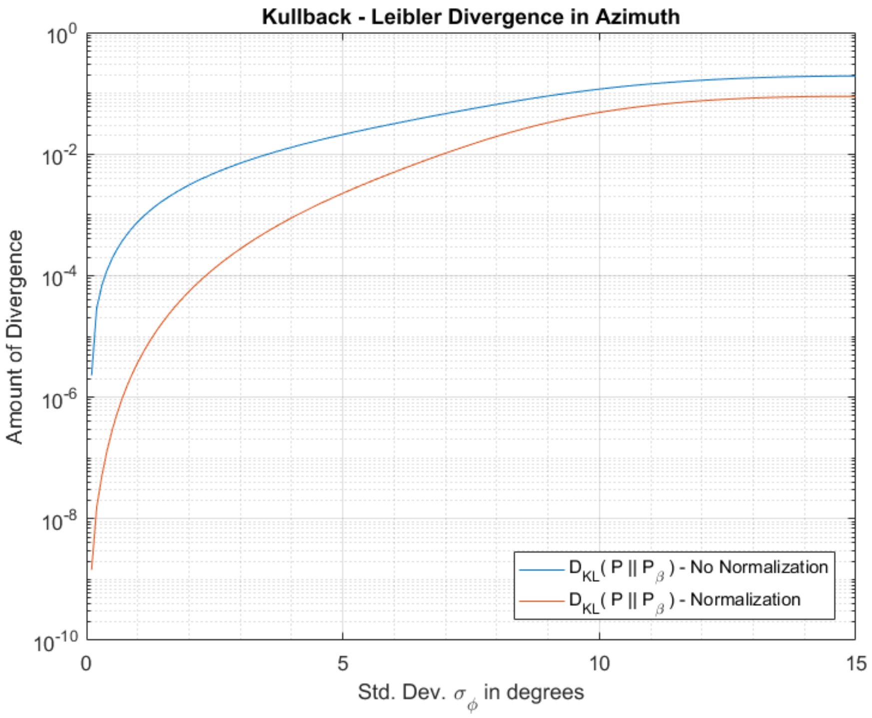

Figure 3.13: KL-Divergence between $p(L_{azi.})$ and $p_{\beta}(L_{azi.})$ as a function of σ_{ϕ} with and without normalization of $p_{\beta}(L_{azi.})$.

Kullback-Leibler Divergence Between $p_{sim}(L_{azi})$ From MC Simulation and Analytically Derived Probability Distributions $p(L_{azi})$ and $p_{\beta}(L_{azi})$

The Kullback-Leibler divergence between $p_{sim}(L_{azi})$ that is gained from the Monte Carlo simulation and the analytically derived probability distribution $p(L_{azi})$ can be written as:

$$D_{KL}\,(P_{sim}\,||\,P) = \sum_{i=1}^{m} p_{sim}(L_{azi,i})\; log\left(\frac{p_{sim}(L_{azi,i})}{p(L_{azi,i})}\right)\delta L_{azi.} \tag{3.52}$$

and similarly,

the Kullback-Leibler divergence between $p_{sim}(L_{azi})$ gained from the Monte Carlo simulation and the analytically derived β-approximated probability distribution $p_{\beta}(L_{azi.})$ can be written as:

$$D_{KL}\left(P_{sim}\,||\,P_{\beta}\right) = \sum_{i=1}^{m} p_{sim}(L_{azi,i})\; log\left(\frac{p_{sim}(L_{azi,i})}{p_{\beta}(L_{azi,i})}\right)\delta L_{azi.} \tag{3.53}$$

where $p(L_{azi,i}) = p(\delta L_{azi}\cdot i)$, $p_{\beta}(L_{azi,i}) = p_{\beta}(\delta L_{azi}\cdot i)$ and $\delta L_{azi} = \frac{1}{m}$ since $L_{azi} \in [0,1]$.

Figure 3.14 below shows the Kullback-Leibler divergence plot between $p_{sim}(L_{azi})$ obtained from the Monte Carlo simulation and the analytically derived pdf's of $p(L_{azi})$ and $p_{\beta}(L_{azi.})$ as a function of σ_{ϕ} for $n = 10000$ realizations of the target and $\delta L_{azi} = 1e-4$ for the leg size of $l = 0.10\ m$ at $f = 77GHz$ for the ideal spherical incidence angles ($\theta_{ideal} = 54.7°, \phi_{ideal} = 45°$). Note that the pdf $p_{\beta}(L_{azi.})$ is normalized in the computations here.

From both Kullback-Leibler divergence plots in the figure can be concluded that for small errors in orientation in terms of σ_{ϕ}-values, the divergence is much smaller than for bigger errors in orientation. Particularly the Kullback-Leibler divergence plot $D_{KL}\,(P_{sim}\,||\,P)$ justifies the correctness of transition

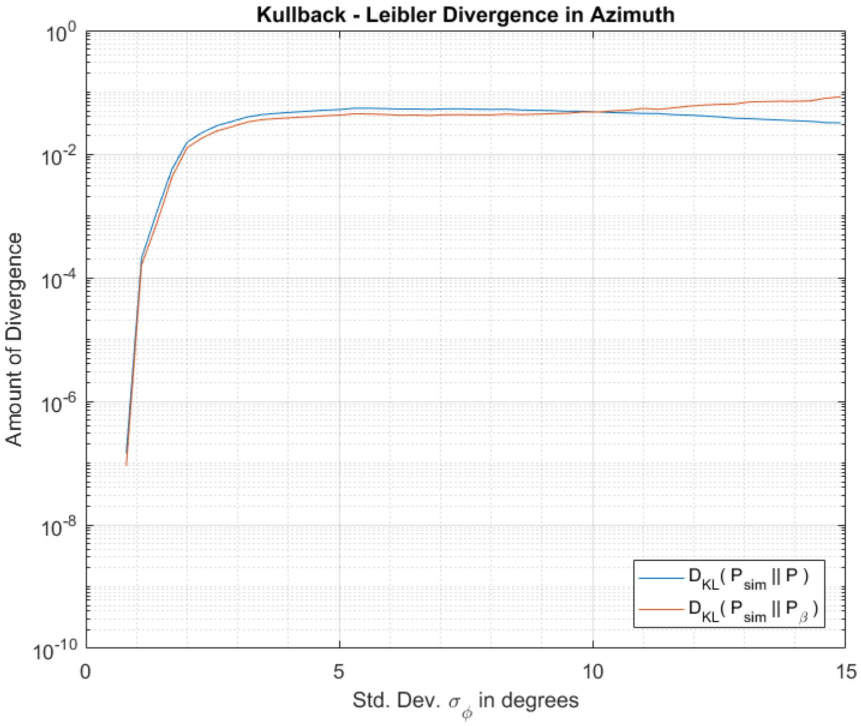

Figure 3.14: Kullback-Leibler Divergence results between $p_{sim}(L_{azi})$ and the probability distributions $p(L_{azi})$ and $p_{\beta}(L_{azi})$ as a function of σ_{ϕ}.

from step 1 to step 2 whereby the approximation of the high-frequency RCS in the vicinity of the maximum is validated. Also, the Kullback-Leibler divergence plot $D_{KL}\left(P_{sim} \,||\, P_{\beta}\right)$ justifies the correctness of transition from step 1 through step 3.

3.2.4. Beta Distribution Fit on the Distribution of RCS Loss Factor $L_{azi.}$

The error in the azimuth orientation is assumed to be normally distributed with the mean value of $E(\phi) = \phi_{ideal}$ and standard deviation of $\sigma_{\phi} = 6.285°$, i.e. $\phi \sim N(\phi_{ideal}, \sigma_{\phi}^2)$.

Figure 3.15 gives the result of the beta distribution fit, that is obtained for n=10000 targets evaluated at $f = 77\ GHz$, on the histogram of the loss factor for the ideal leg length $l_{ideal} = 0.10\ m$ and ideal elevation incidence angle θ_{ideal}. The corresponding shape parameters for this beta distribution are estimated to be $\alpha = 12.33$ and $\beta = 0.492$.

Additionally, figure 3.16 gives the results of the beta distribution fit for the ideal leg length l_{ideal} and ideal elevation incidence angle θ_{ideal} for different variances of $\sigma_{\phi,1}^2 > \sigma_{\phi,2}^2 > \sigma_{\phi,3}^2$. As expected, as the variance gets smaller, the beta distribution gets narrower which means the loss factor $L_{azi.}$ gets closer to the unity.

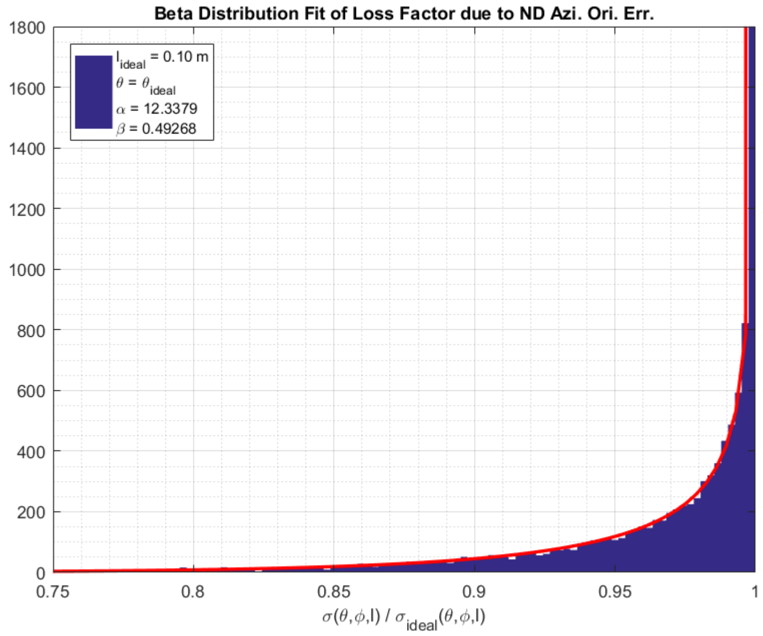

Figure 3.15: Beta distribution fit of the loss factor in RCS due to orientation errors in azimuth plane.

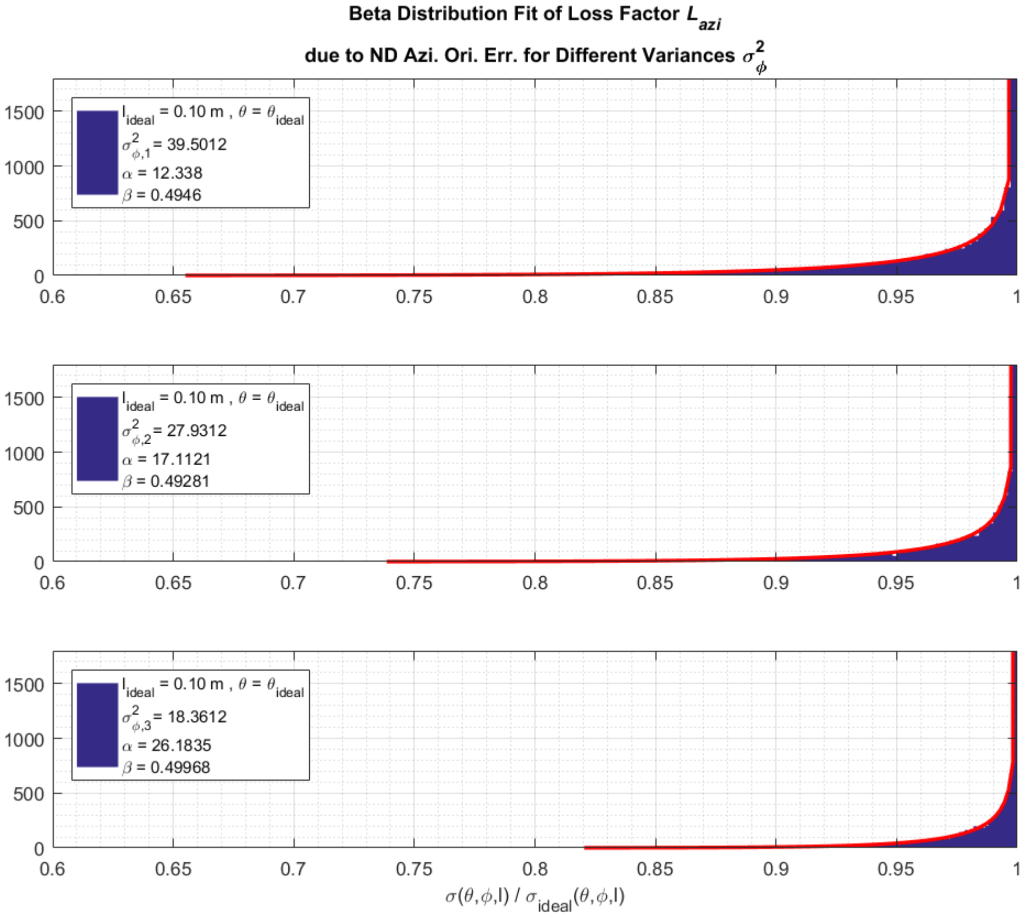

Figure 3.16: Beta distribution fit of the loss factors in RCS due to orientation errors in azimuth plane for different variances of $\sigma^2_{\phi,1} > \sigma^2_{\phi,2} > \sigma^2_{\phi,3}$.

Furthermore, also a beta distribution fit analysis is made on the distribution of the RCS loss factor, $L_{azi.,veh.pos.}$, that originates from the observation errors. Observation error in the azimuth plane was modelled to be uniform distributed between ϕ_{min} and ϕ_{max}, i.e. $U(\phi_{min}, \phi_{max})$, which was, according to the configuration used, found to be $\phi_{min} = 38.715°$ and $\phi_{max} = 51.285°$.

Figure 3.17 gives the result of this analysis, which is obtained for n=10000 targets evaluated at $f = 77\ GHz$, for the ideal leg length $l_{ideal} = 0.10\ m$ and ideal elevation incidence angle θ_{ideal}, including the estimated shape parameters $\alpha = 50.12$ and $\beta = 0.668$.

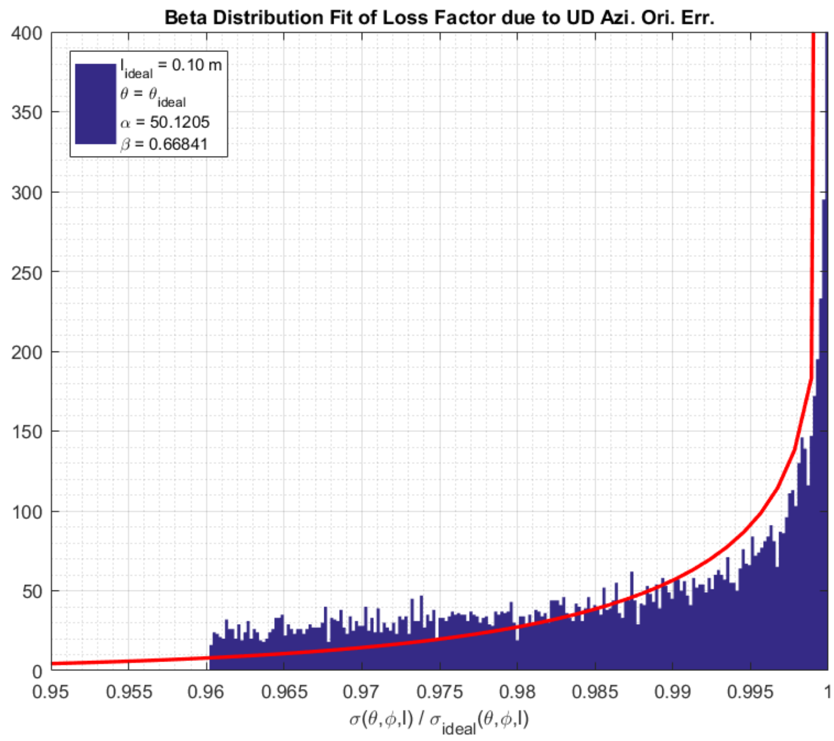

Figure 3.17: Beta distribution fit of the loss factor in RCS due to errors in the position of vehicles in azimuth plane.

3.3. RCS Loss Factor due to Errors in Leg Length

Considering equation (2.10), yet another factor that can cause RCS loss is the inaccuracy in the leg length l of the corner reflectors. The RCS loss factor solely due to production errors in leg length is then:

$$L_{pro.} = \frac{\sigma(\theta_{ideal}, \phi_{ideal}, l)}{\sigma_{ideal}(\theta_{ideal}, \phi_{ideal}, l_{ideal})} \tag{3.54}$$

3.3.1. Analytical Derivation of the Probability Distribution of the Loss Factor $L_{pro.}$ due to Errors in Leg Length

If it is assumed that the corner reflectors can be produced with some acceptable tolerance in the leg lengths, they can be assumed to be normal distributed with mean l_{ideal} and variance σ_l^2, i.e. $l \sim N(l_{ideal}, \sigma_l^2)$:

$$p_1(l) = \frac{1}{\sqrt{2\pi\sigma_l}}\, exp\left(- \frac{(l - l_{ideal})^2}{2\sigma_l^2} \right) \tag{3.55}$$

From equations (2.10) and (3.54) follows that:

$$L_{pro.} = \frac{4\pi}{\sigma_0\, \lambda_0^2} l^4 \left[x - \frac{2}{x} \right]^2, \text{ with } x = \cos\theta + \sin\theta(\sin\phi + \cos\phi) \\ \text{and } \sigma_0 = \sigma_{ideal}(\theta_{ideal}, \phi_{ideal}, l_{ideal}) \tag{3.56}$$

Following the procedure given in the previous section, the probability distribution of the loss factor $L_{pro.}$ is obtained analytically from the probability distribution $p_1(l)$ of length l from equation (3.55) to be :

$$p(L_{pro.}) = \frac{1}{2(\frac{\pi}{\sigma_0})^{1/4}\sqrt{2\pi}\sigma_l}\, L_{pro.}^{-3/4} \left(\frac{\lambda_0}{2[x - \frac{2}{x}]} \right)^{1/2} exp\left(- \frac{\left\{ \left(\frac{L_{pro.}\, \sigma_0}{\pi} \right)^{1/4} \left(\frac{\lambda_0}{2[x - \frac{2}{x}]} \right)^{1/2} - l_{ideal} \right\}^2}{2\sigma_l^2} \right) \tag{3.57}$$

3.3.2. Normal Distribution Fit on the Distribution of RCS Loss Factor $L_{pro.}$

Figure 3.18 represents the result of the normal distribution fit on the distribution of the RCS loss factor that is obtained for n=10000 targets evaluated at $f = 77\ GHz$. In the simulation, leg lengths of the reflectors are assumed to be normal distributed with mean value of $E(l) = l_{ideal} = 0.10\ m$ and standard deviation of $\sigma_l = 2\ mm$, i.e. $l \sim N(l_{ideal}, \sigma_l^2)$. The distribution of the RCS loss can clearly be fitted by a normal distribution.

From this result can be concluded that the pdf in equation (3.57) might further be approximated by a normal distribution.

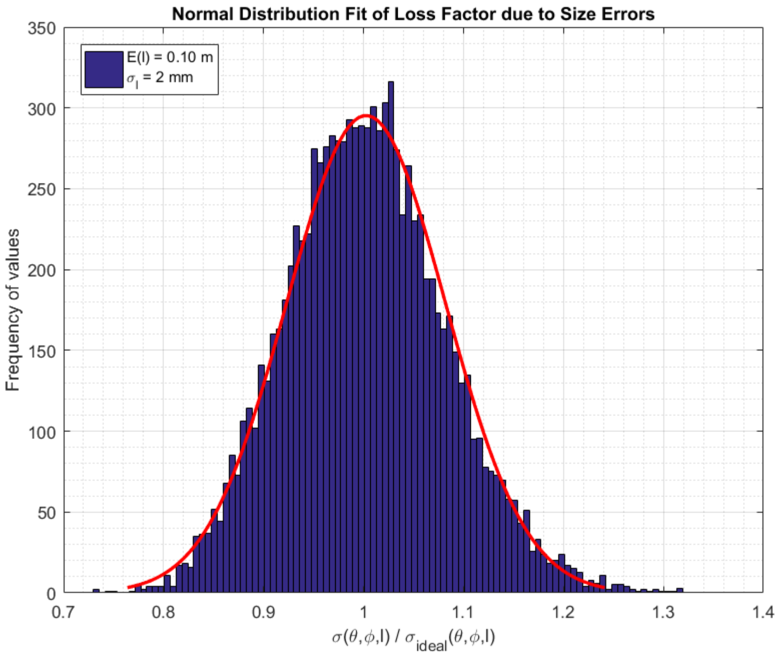

Figure 3.18: Normal distribution fit of the loss factor in RCS due to errors in the leg length of the reflector.

3.4. RCS Loss Factor due to Non-Orthogonality

For trihedral corner reflectors, the maximum expected loss for a given trihedral for angular deviations smaller than 1° can be approximated by:

$$\begin{aligned} L_{non.orth.} &= 10\log_{10}(\frac{\sin q}{q})^4 \\ &= 10\log_{10} sinc^4(q)\ [dB], \text{ where } q = \frac{2.54\ \delta_{err} l}{\lambda} \end{aligned} \tag{3.58}$$

with l is the leg length and δ_{err} is the threefold angular error (i.e. deviation angle) in radian as given in [13]. It is clear from the equation that the loss due to non-orthogonality is a function of two variables, namely the angular error δ_{max} and the leg length l. Due to the restriction that this equation puts, production of the trihedral corner reflectors should be at most within 1° of precision in the corner walls.

3.4.1. Analytical Derivation of the Probability Distribution of the Loss Factor $L_{non.orth.}$ due to Mass Production Errors

If the corner reflectors can be produced with some acceptable tolerance in the alignment of the surfaces during mass production, with no extra knowledge about the angular error, it can be assumed to be normal distributed :

$$p_1(\delta_{err}) = \frac{1}{\sqrt{2\pi}\sigma_{\delta_{err}}}\, exp\left(-\frac{\delta_{err}^2}{2\sigma_{\delta_{err}}^2}\right) \tag{3.59}$$

For small angular error, function (3.58) can be approximated, by means of its Taylor series representation, with $sinc\ (x) \approx 1 - \frac{x^2}{6}$, which gives:

$$L_{non.orth} \approx (1 - C\ \delta_{err}^2)^4, \tag{3.60}$$

where $C = \frac{(2.54l)^2}{6\lambda^2}$.

The probability distribution of the loss factor $L_{non.orth}$ can be derived by means of "Transformation of Random Variables" from the probability distribution $p_1(\delta_{err})$ of the angular error δ_{err} from equation (3.59). Applying transformation of the variable from (3.60) to the PDF of (3.59), the probability distribution $p(L_{non.orth})$ is:

$$p(L_{non.orth.}) = 2\ p_1(\delta_{err}(L_{non.orth.})) \left| \frac{d\delta_{err}}{dL_{non.orth.}} \right| \tag{3.61}$$

where the factor 2 comes from the even symmetry of the function in equation (3.60), and,

$$\delta_{err}(L_{non.orth.}) = \left(\frac{1 - L_{non.orth.}^{1/4}}{C} \right)^{1/2} \tag{3.62}$$

is the inverse function that follows from equation (3.60). Taking the absolute value of the derivative of this inverse function gives:

$$\left| \frac{d\delta_{err}}{dL_{non.orth.}} \right| = \frac{L_{non.orth}^{-3/4}}{8C\left(\frac{1-L_{non.orth}^{1/4}}{C}\right)^{1/2}} \tag{3.63}$$

and,

$$p_1(\delta_{err}(L_{non.orth.})) = \frac{1}{\sqrt{2\pi}\sigma_{\delta_{err}}}\, exp\left(-\frac{\left(\frac{1-L_{non.orth.}^{1/4}}{C}\right)}{2\sigma_{\delta_{err}}^2}\right) \tag{3.64}$$

Finally, putting the pieces together according to equation (3.61) and simplifying the results, the probability distribution of the loss factor $L_{non.orth.}$ is obtained analytically to be:

$$p(L_{non.orth.}) = \frac{1}{4\sqrt{2\pi C}\sigma_{\delta_{err}}} L_{non.orth.}^{-3/4} \, (1 - L_{non.orth.}^{1/4})^{-1/2} \, exp\left(- \frac{1 - L_{non.orth.}^{1/4}}{2C\sigma_{\delta_{err}}^2} \right) \tag{3.65}$$

Next, equation (3.65) can be approximated by β-distribution for small error. For small angular error, i.e. $\delta_{err} \approx 0$ in equation (3.60), the loss factor becomes approximately $L_{non.orth}. \approx 1$.

Denote $(1 - L_{non.orth}^{1/4}) = f(h)$, the Taylor expansion of $f(h)$ around the point $L_{non.orth.,0} \approx 1$ follows as:

$$f(h)\Big|_{L_{non.orth.}=L_{non.orth.,0}} \approx f(L_{non.orth.,0}) + \frac{d\, f(L_{non.orth.})}{dL_{non.orth.}}\Big|_{L_{non.orth.}=L_{non.orth.,0}} (L_{non.orth.} - L_{non.orth.,0}) \tag{3.66}$$

The elements of the Taylor polynomial from equation (3.66) can be obtained to be:

$$f(L_{non.orth.,0}) \approx (1 - L_{non.orth.,0}^{1/4}) = 0 \tag{3.67}$$

$$\frac{d\, f(L_{non.orth.})}{dL_{non.orth.}}\Big|_{L_{non.orth.}=L_{non.orth.,0}} = -\frac{1}{4} \tag{3.68}$$

which, after filling into equation 3.66, results in:

$$(1 - L_{non.orth}^{1/4})\Big|_{L_{non.orth.}=L_{non.orth.,0}} \approx -\frac{1}{4}(L_{non.orth.} - 1) = \frac{1}{4}(1 - L_{non.orth.}) \tag{3.69}$$

Furthermore, the following factor from equation (3.65) can be re-written as:

$$\begin{aligned} exp\left(- \frac{1 - L_{non.orth.}^{1/4}}{2C\sigma_{\delta_{err}}^2} \right) &= \left[exp(1 - L_{non.orth.}^{1/4}) \right]^{-1/2C\sigma_{\delta_{err}}^2} \approx \left[exp\left(-\frac{1}{4}(L_{non.orth.} - 1) \right) \right]^{-1/2C\sigma_{\delta_{err}}^2} \\ &= [exp\,(L_{non.orth.} - 1)]^{1/8C\sigma_{\delta_{err}}^2} \end{aligned} \tag{3.70}$$

Now, denote $exp(L_{non.orth.} - 1) = f(y)$, the Taylor expansion of $f(y)$ around the point $L_{non.orth.,0} \approx 1$ follows as:

$$f(y)\Big|_{L_{non.orth.}=L_{non.orth.,0}} \approx f(L_{non.orth.,0}) + \frac{d\, f(L_{non.orth.})}{dL_{non.orth.}}\Big|_{L_{non.orth.}=L_{non.orth.,0}} (L_{non.orth.} - L_{non.orth.,0}) \tag{3.71}$$

The elements of the Taylor polynomial from equation (3.71) can be obtained to be:

$$f(L_{non.orth.,0}) \approx exp\,(L_{non.orth.,0} - 1) = exp\,(0) = 1 \tag{3.72}$$

$$\frac{d\, f(L_{non.orth.})}{dL_{non.orth.}}\Big|_{L_{non.orth.}=L_{non.orth.,0}} \approx exp\,(L_{non.orth.,0} - 1) = exp\,(0) = 1 \tag{3.73}$$

which, after filling into equation 3.71, results in:

$$exp\,(L_{non.orth.} - 1)\Big|_{L_{non.orth.}=L_{non.orth.,0}} \approx L_{non.orth.}. \tag{3.74}$$

Therefore,

$$[exp\,(L_{non.orth.}-1)]^{1/8C\sigma^2_{\delta_{err}}} \approx L_{non.orth.}^{1/8C\sigma^2_{\delta_{err}}} \tag{3.75}$$

Using these approximations in (3.65) gives:

$$p(L_{non.orth.}) \approx \frac{1}{2\sqrt{2\pi C}\sigma_{\delta_{err}}} L_{non.orth.}^{\frac{1}{8C\sigma^2_{\delta_{err}}}-\frac{3}{4}} (1-L_{non.orth.})^{-1/2} \tag{3.76}$$

which has the form of β-distribution pdf with the shape parameters:

$$\alpha = \frac{1}{8C\sigma^2_{\delta_{err}}} + \frac{1}{4}; \tag{3.77}$$

$$\beta = \frac{1}{2}, \tag{3.78}$$

However, this pdf is subject to normalization to satisfy the rule that $\int_0^1 p(L_{non.orth.})\,dL_{non.orth.} = 1$. It is notable that the error in orientation affects only the parameter α of the distribution, in which $\beta = 0.5$ is a fixed value.

Figure 3.19 below represents the plots of shape parameters obtained from the derived β-distribution alongside the shape parameters obtained from the Monte-Carlo simulations, for n=10000 targets evaluated at $f = 77\ GHz$, as a function of the angular error δ_{err} at different leg sizes. From the figures can be concluded that the two curves agree quite well at small errors. It is also notable that as the leg size increases, two curves are becoming apart at smaller values of angular error.

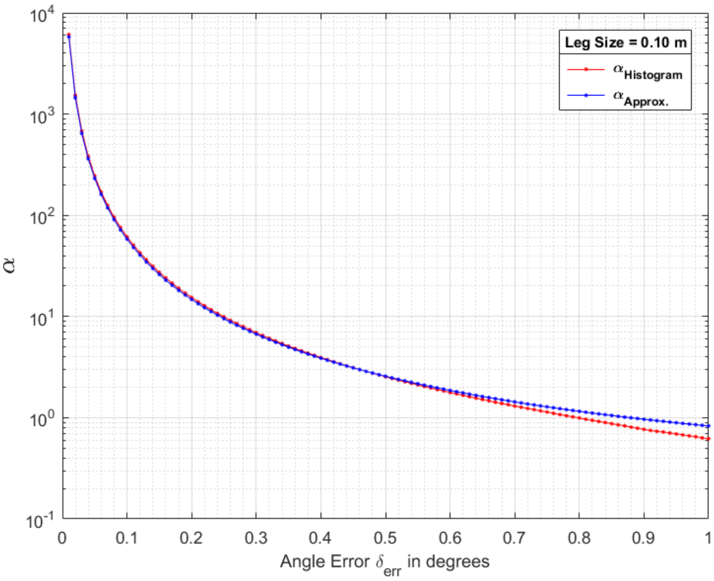

(a) for leg size l=0.10 m.

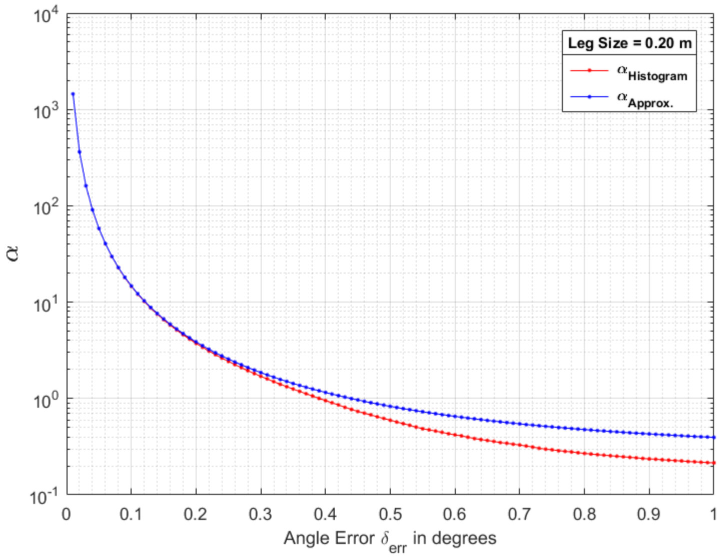

(b) for leg size l=0.20 m.

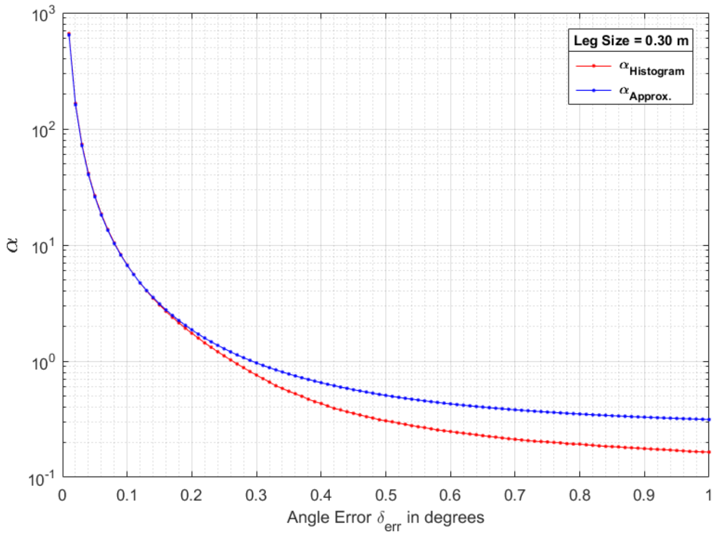

(c) for leg size l=0.30 m.

Figure 3.19: Shape Parameters α's vs. Angle Errors

Figure 3.20 below represents the plots of the shape parameters obtained from the derived β-distribution alongside the shape parameters obtained from the Monte-Carlo simulations, for n=10000 targets evaluated at $f = 77\ GHz$, as a function of the leg size l at different angular errors δ_{err}. From the figures can be concluded that, at a given angular error δ_{err}, the two curves agree quite well at smaller leg sizes. The fact that the two curves are becoming apart at smaller values of angular error as the leg size increases is more obvious from the plots in this figure.

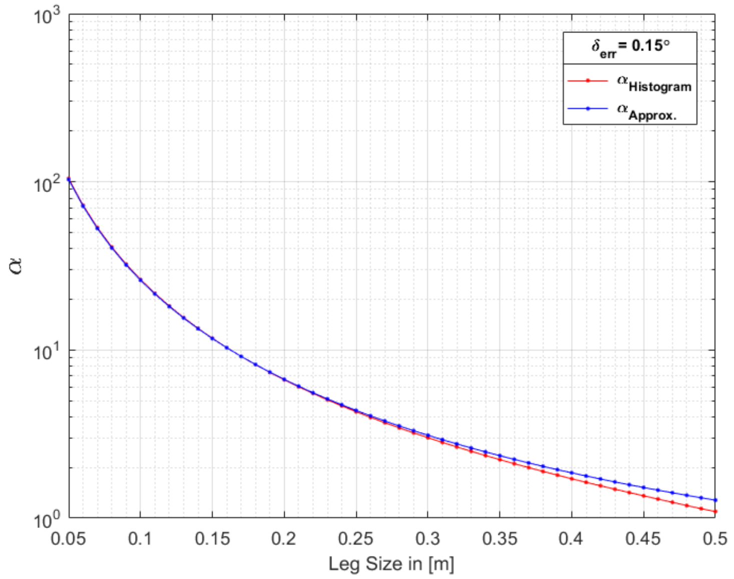

(a) at std. dev. of δ_{err} = 0.15 °

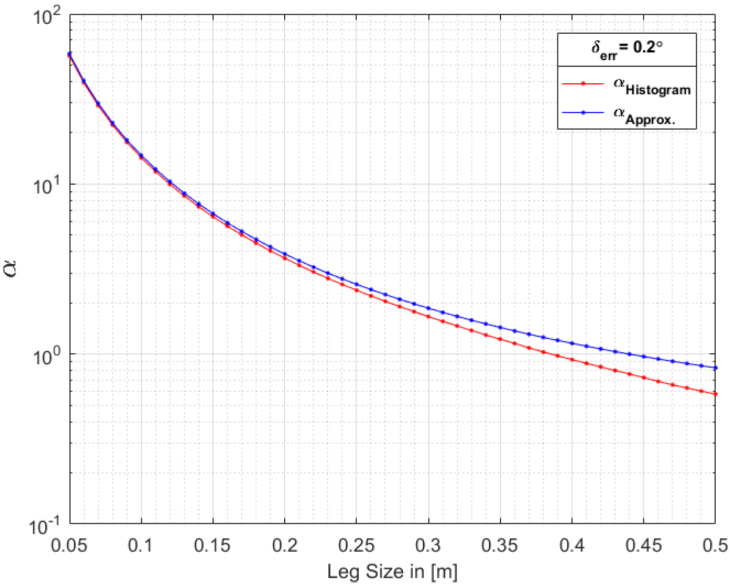

(b) at std. dev. of δ_{err} = 0.20 °

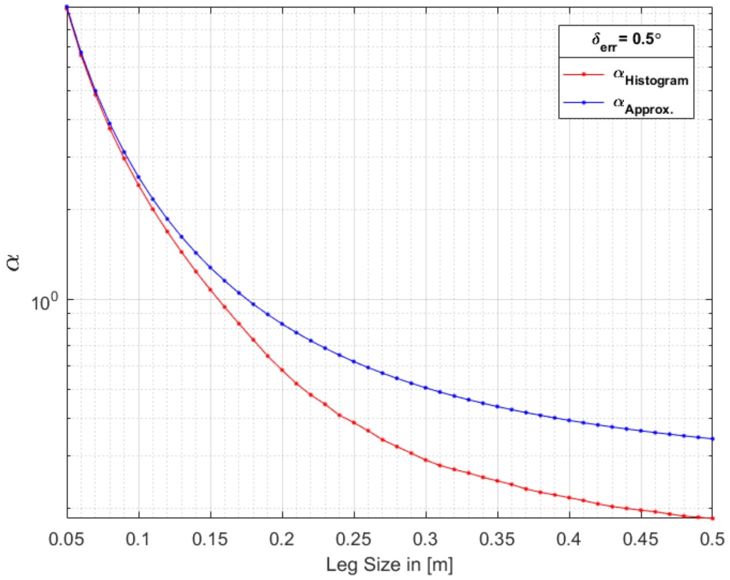

(c) at std. dev. of δ_{err} = 0.50 °

Figure 3.20: Shape Parameters α's vs. Leg Size

3.4.2. Beta Distribution Fit on the Distribution of RCS Loss Factor due to Angular Error at *l=0.10 m.*

In this section, a beta distribution fit on the histograms of the loss factor due to angular errors in the corner reflector is performed at different δ_{err} deviation angles, when the size of the reflector is kept fixed to be $l = 0.10\ m$. This is represented in figure 3.21.

From the plots in figure 3.21 can be seen that beyond a certain amount of angular error, a second peak starts to appear, which is found to be roughly about $\delta_{err} \approx 0.50°$ for $l = 0.10\ m$. Therefore, under these conditions, the maximum amount of angular error that is applicable is $\delta_{err,max} = 0.50°$ and the corresponding shape parameters are estimated to be $\alpha = 2.398$ and $\beta = 0.489$.

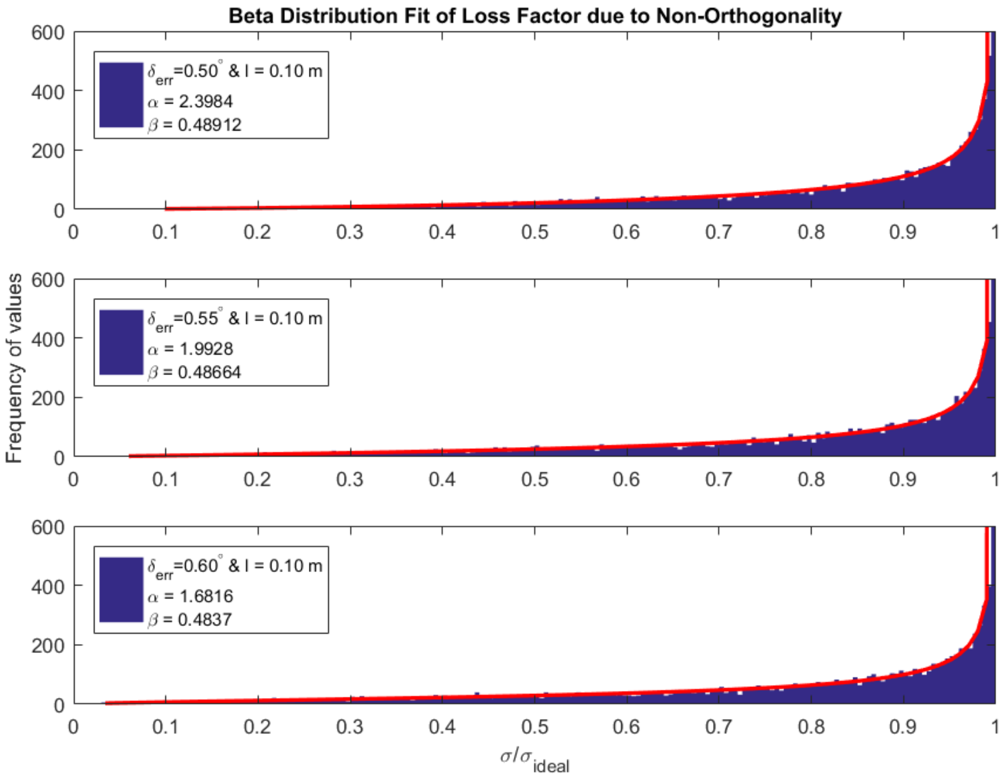

(a) Beta distribution fit for deviations of $\delta_{err} = 0.50°$, $\delta_{err} = 0.55°$ and $\delta_{err} = 0.60°$

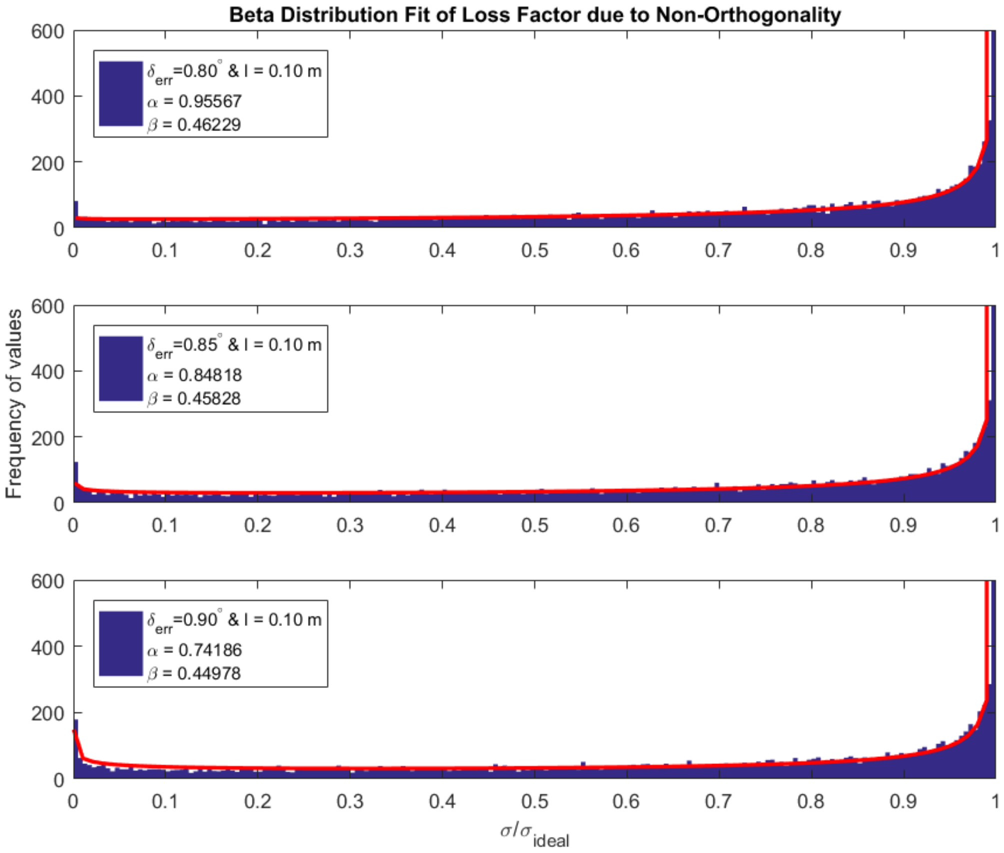

(b) Beta distribution fit for deviations of $\delta_{err} = 0.80°$, $\delta_{err} = 0.85°$ and $\delta_{err} = 0.90°$

Figure 3.21: Beta Distribution fit plots for different deviation angles from the orthogonality for $l = 0.10\ m$.

Additionally, the RCS pattern vs. deviation angles δ_{err}, which follows directly from equation (3.58), is plotted in figure 3.22 with the second lobe present for leg size of $l = 0.10\ m$. In the figure, an additional straight blue line is drawn at -3-dB level as well as the minima are highlighted whereafter the second lobe starts to appear as can be seen from the figure.

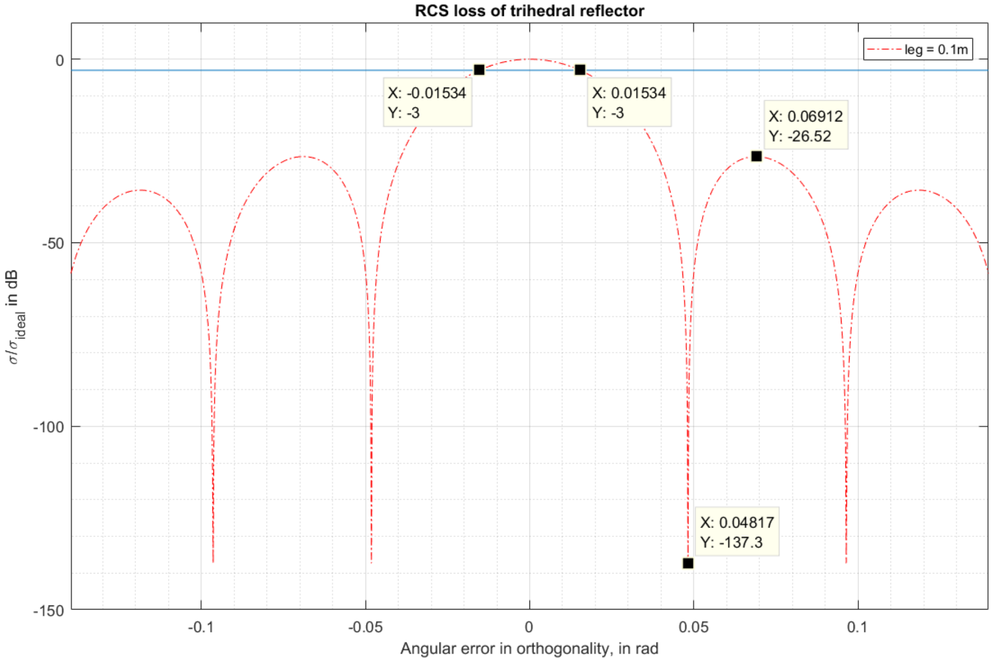

Figure 3.22: RCS loss pattern of the trihedral corner reflector vs. deviation angle δ_{max} in radians from the orthogonality, at leg size of $l = 0.10\ m$.

In figure 3.23, the plots are given in which the estimated shape parameters α and β of the beta distributions are plotted versus the deviation angles δ_{err} in relative scale at leg length of $l = 0.10\ m$, with a vertical blue line indicating the maximum applicable deviation angle $\delta_{err,max}$.

Moreover, an evaluation is made to see how the shape parameters α and β behave if the leg size of the reflector increases for the deviation angle δ_{err} kept fixed. This is plotted and represented in figure 3.24 at $\delta_{err} = 0.50°$. From the figure can be concluded that the shape parameter α decreases under 0.5 for leg sizes bigger than $l = 0.25\ m$ while the shape parameter β at starts to increase again beyond leg size of $l = 0.30\ m$.

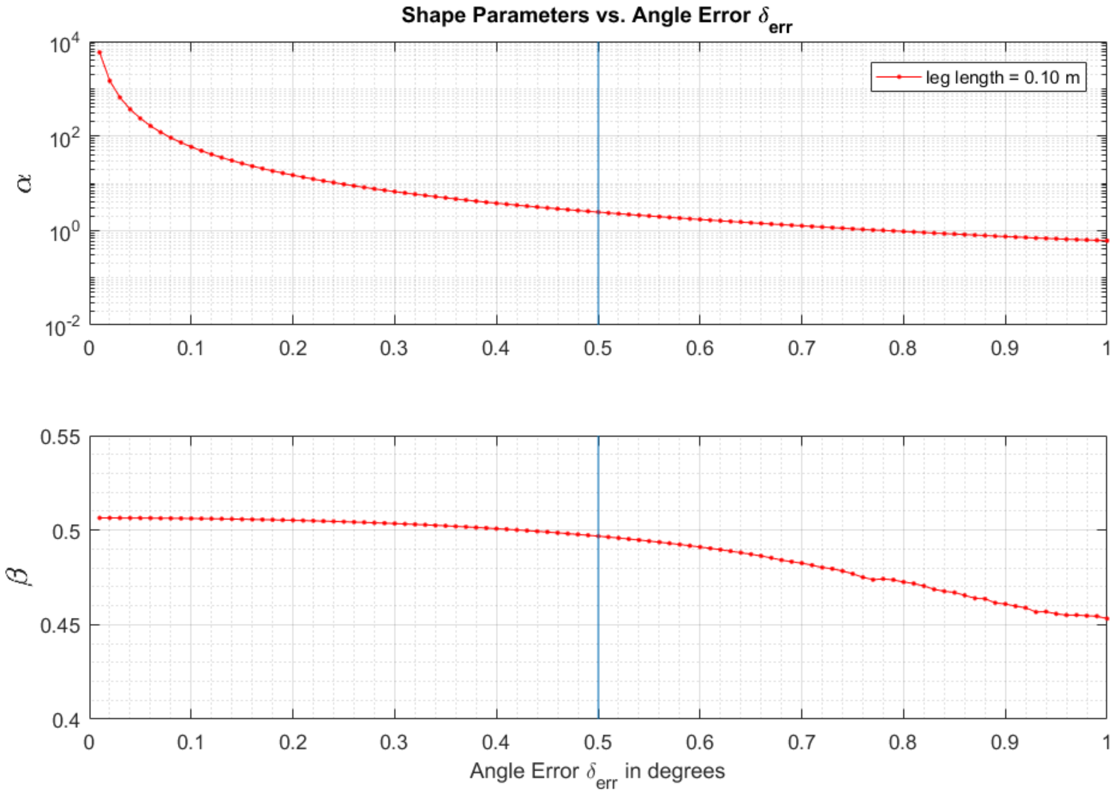

Figure 3.23: Estimated shape parameters at leg size $l = 0.10\ m$ vs. deviation angles δ_{err}.

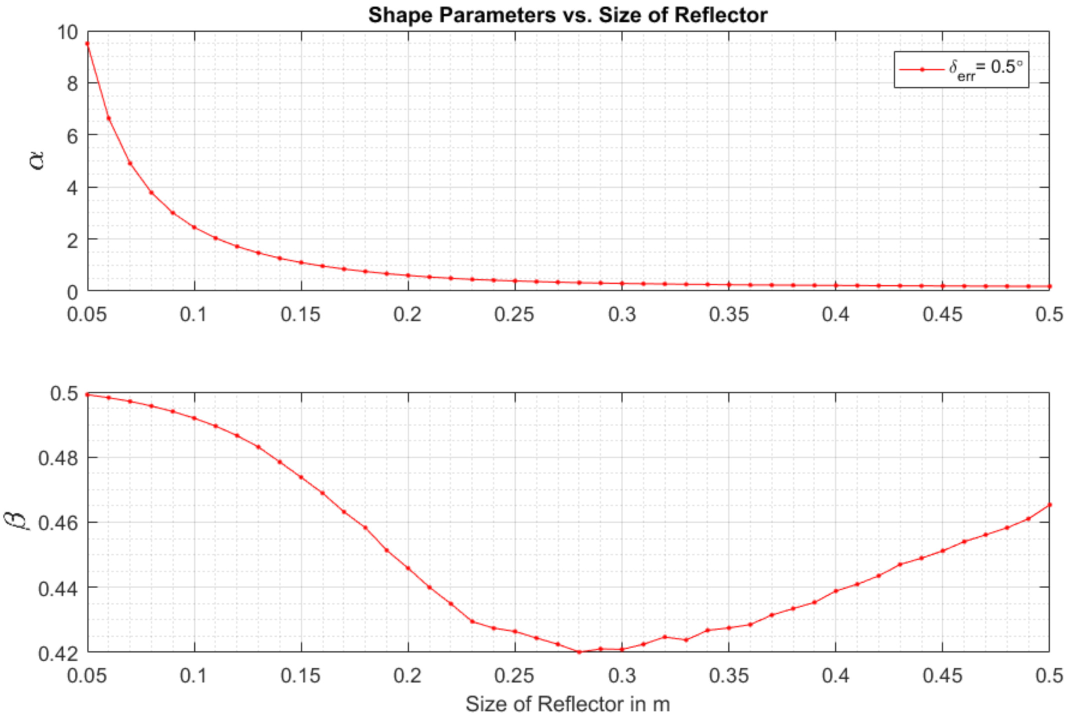

Figure 3.24: Estimated shape parameters at deviation angle $\delta_{err} = 0.50°$ vs. the leg size of the reflector.

3.4.3. Beta Distribution Fit on the Distribution of RCS Loss Factor due to Angular Error at Other Leg Sizes

This section deals with the similar evaluations, as in previous section, for leg sizes of $l = 0.20\ m$ and $0.30\ m$. Figure 3.25 gives the 3-dB beamwidths at the leg sizes $l = 0.10\ m$, $l = 0.20\ m$ and $l = 0.30\ m$, both in radians and in degrees, after investigating the RCS patterns for the latter two leg sizes in the same way done for leg size $l = 0.10\ m$ in the last section. From this figure can be seen that the 3-dB beamwidth decreases with the increasing leg size.

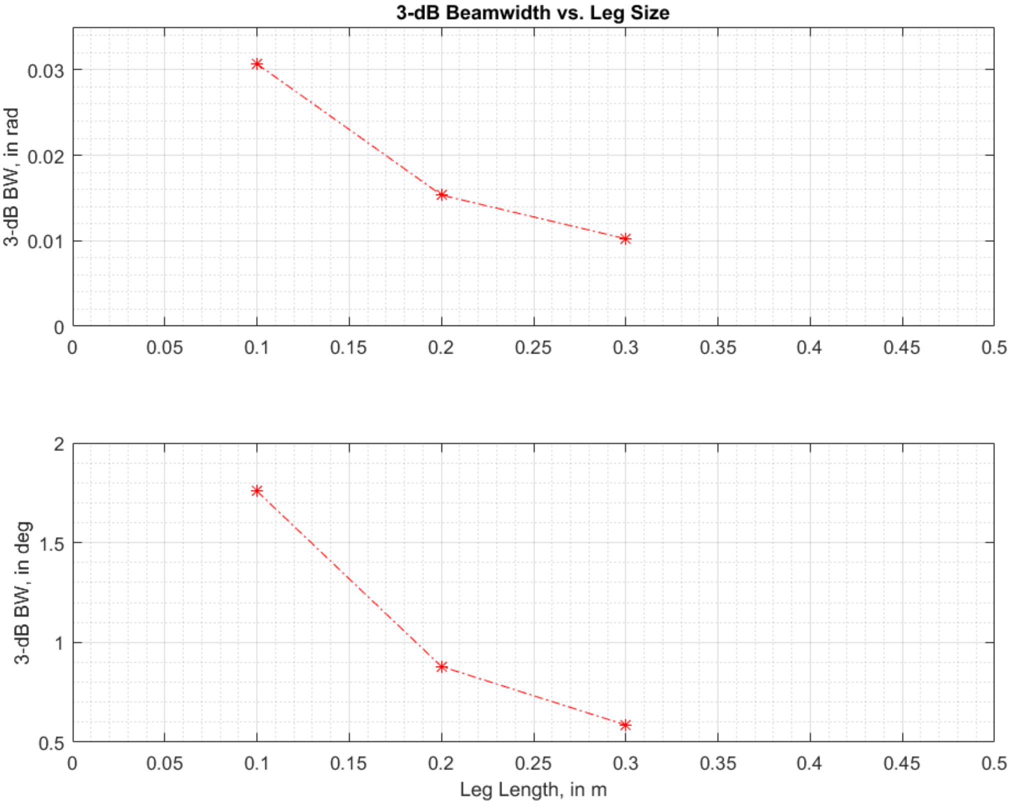

Figure 3.25: 3-dB beamwidth vs. the leg sizes of $l = 0.10\ m$, $l = 0.20\ m$ and $l = 0.30\ m$, with upper figure representing it given in radians and lower figure given in degrees.

The beta distribution fit analysis resulted in that, at the leg size $l = 0.20\ m$ the maximum amount of angular error that is applicable in this work is roughly $\delta_{err,max} \approx 0.25°$, whereas it is roughly $\delta_{err,max} \approx 0.20°$ for the leg size $l = 0.30\ m$, because a second peak tends to appear in the beta distribution fit plots when the deviation angle δ_{err} gets bigger than these values, respectively at the considered leg sizes. The corresponding shape parameters are estimated to be $\alpha = 2.476$ and $\beta = 0.491$ for the leg size of $l = 0.20\ m$ and $\alpha = 1.712$ and $\beta = 0.491$ for the leg size of $0.30\ m$.

Figure 3.26 gives the plots in which the estimated shape parameters α and β of the beta distributions are plotted versus the deviation angles δ_{err} in relative scale at leg lengths of $l = 0.20\ m$ and $l = 0.30\ m$. Again with a vertical blue line indicating the maximum applicable angular error $\delta_{max,err}$ at the given leg sizes.

Considering figures 3.23 and 3.26, one can conclude that the second peak in the beta distribution fit plots appears earlier when the size of the reflector gets bigger.

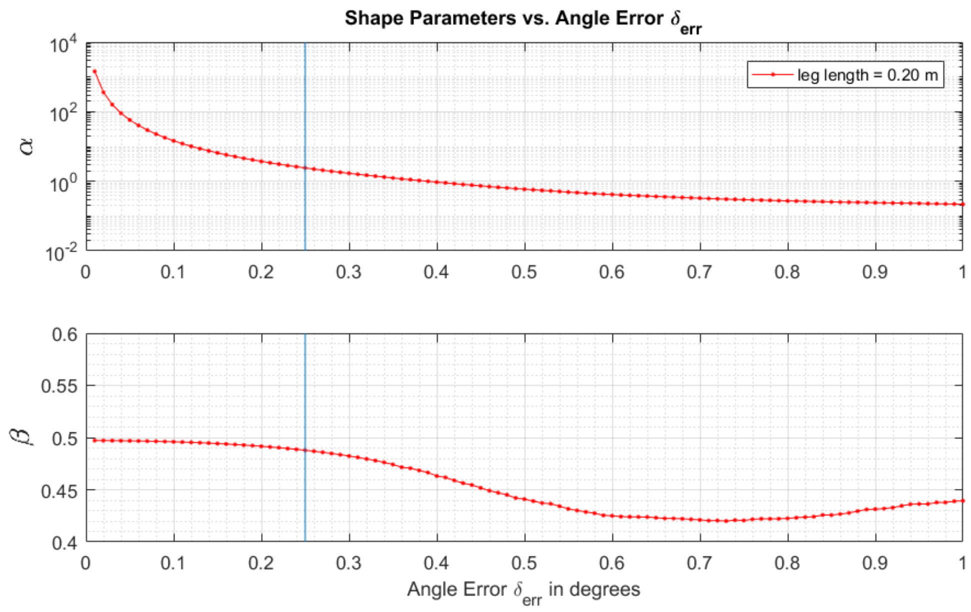

(a) At leg size of $l = 0.20\ m$

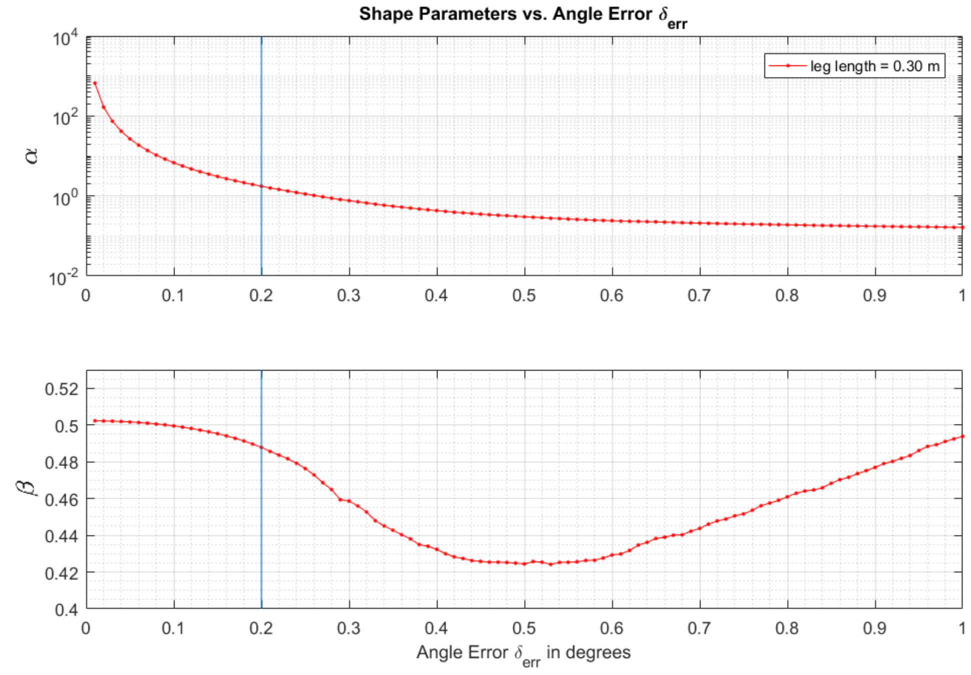

(b) At leg size of $l = 0.30\ m$

Figure 3.26: Estimated shape parameters vs. deviation angles δ_{err} at leg sizes of $l = 0.20\ m$ and $l = 0.30\ m$, respectively. Vertical blue line denotes $\delta_{err,max}$.

As in the previous section, again an evaluation is made to see how the shape parameters α and β behave if the leg size of the reflector increases, with the deviation angle δ_{err} being fixed. The results are given in figure 3.27 for deviation angles $\delta_{err} = 0.25°$ and $\delta_{err} = 0.20°$, respectively. From the figures can be concluded that at both deviation angles the shape parameters α and β decrease with the increasing leg size of the reflector.

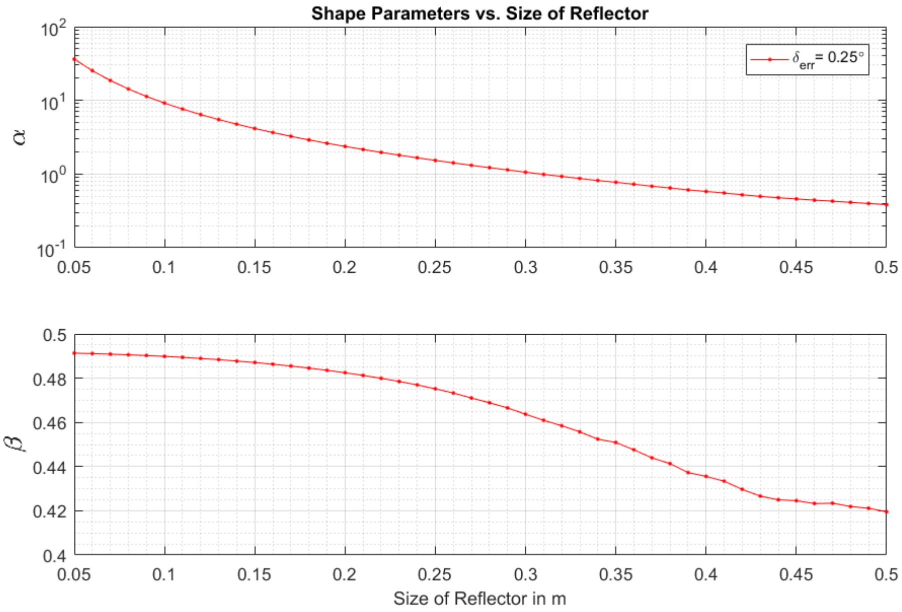

(a) At $\delta_{err} = 0.25°$.

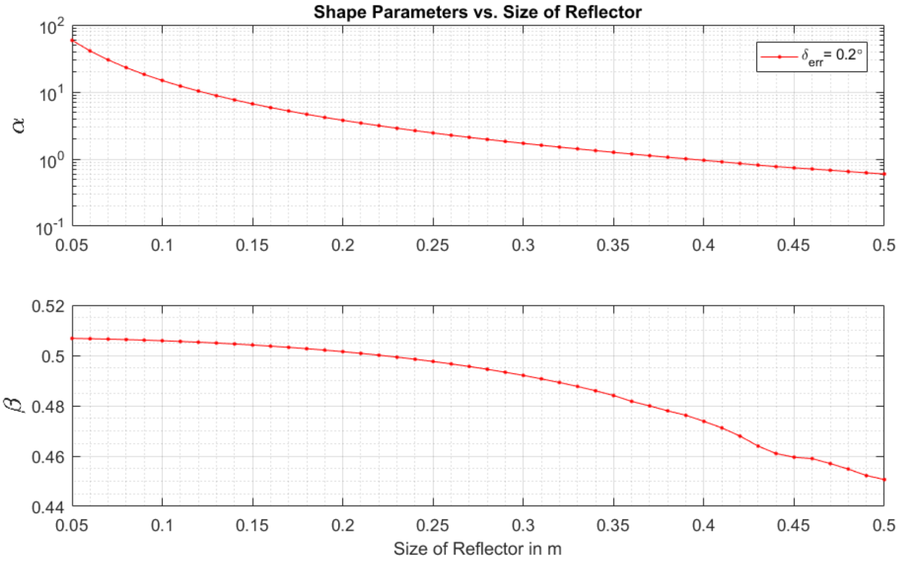

(b) At $\delta_{err} = 0.20°$.

Figure 3.27: Estimated shape parameters vs. leg size of the reflector, with the deviation angles δ_{err} kept fixed at $\delta_{err} = 0.25°$ and $\delta_{err} = 0.20°$, respectively.

In table 3.1, a summary of the evaluations made above is given at the three leg sizes considered.

Table 3.1: **Summary of beta distribution fit analysis at different leg sizes**

Leg Size in m	**Max. Allowable Angular Error** $\delta_{max,err}$ **in deg**	**Max. Allowable Angular Error** $\delta_{max,err}$ **in rad**	**Shape Parameter** α	**Shape Parameter** β
0.10 m	0.50 °	0.0087	2.398	0.489
0.20 m	0.25 °	0.0044	2.476	0.491
0.30 m	0.20 °	0.0035	1.712	0.491

In general, better visibility of the target requires bigger size but, as can be concluded from the results in the table, bigger size in turn requires higher production precision in terms of the angular error $\delta_{max,err}$. Also note that, as the size gets bigger, the second lobe will appear earlier since $\delta_{max,err}$ value gets then smaller. This is in accordance with the decreasing 3-dB beamwidth as the size of the corner reflector gets bigger. Furthermore, the shape parameters β are almost always about $\beta \approx 0.5$, as resulted from the analytical derivation, while the shape parameter α changes from one leg size to another.

3.4.4. A Theoretical Check : Match Between The Expected Maximum Allowable Angular Errors from Theory and Simulations

The maximum allowable angular errors $\delta_{err,max}$ from the simulations given in table 3.1 are thus the deviation angles beyond which a second peak starts to appear in the beta distribution fit plots. Specifically, denote the expected maximum allowable angular error from theory to be δ_{err,max_exp}. The histograms of the RCS loss factor due to non-orthogonality, using the formula from equation (3.58), are generated by means of a Monte Carlo simulation in which the angular errors δ_{err}'s are assumed to be normal distributed. From the properties of a normal distribution it is known that 99.7% of the data lies within three standard deviations of the mean.

Consider figure 3.28 in which the RCS loss pattern of the trihedral corner reflector for leg size of $l = 0.10\ m$ and an example pdf of normal distribution are given [14]. In the upper figure, δ_0 denotes the normal distributed angular error where the first minimum in the RCS loss pattern before the second lobe arises and in the lower figure, σ_{CA} is the standard deviation of the corner angles (CA), i.e. $\sigma_{CA} = \delta_{err}$, near the minimum in the pdf of normal distribution.

Theoretically, one would expect that, considering the symmetry in the pdf of normal distribution, the second peak in the beta distribution fit plot would start to appear beyond $\delta_0 = 6 \cdot \sigma_{CA}$, where the standard deviation of the corner angle should be set to $\sigma_{CA} = \delta_{err,max}$. This means that if there is a match between δ_0 and δ_{err,max_exp} values, it can be concluded that the maximum allowable angular errors $\delta_{err,max}$'s achieved from the simulations are the good ones.

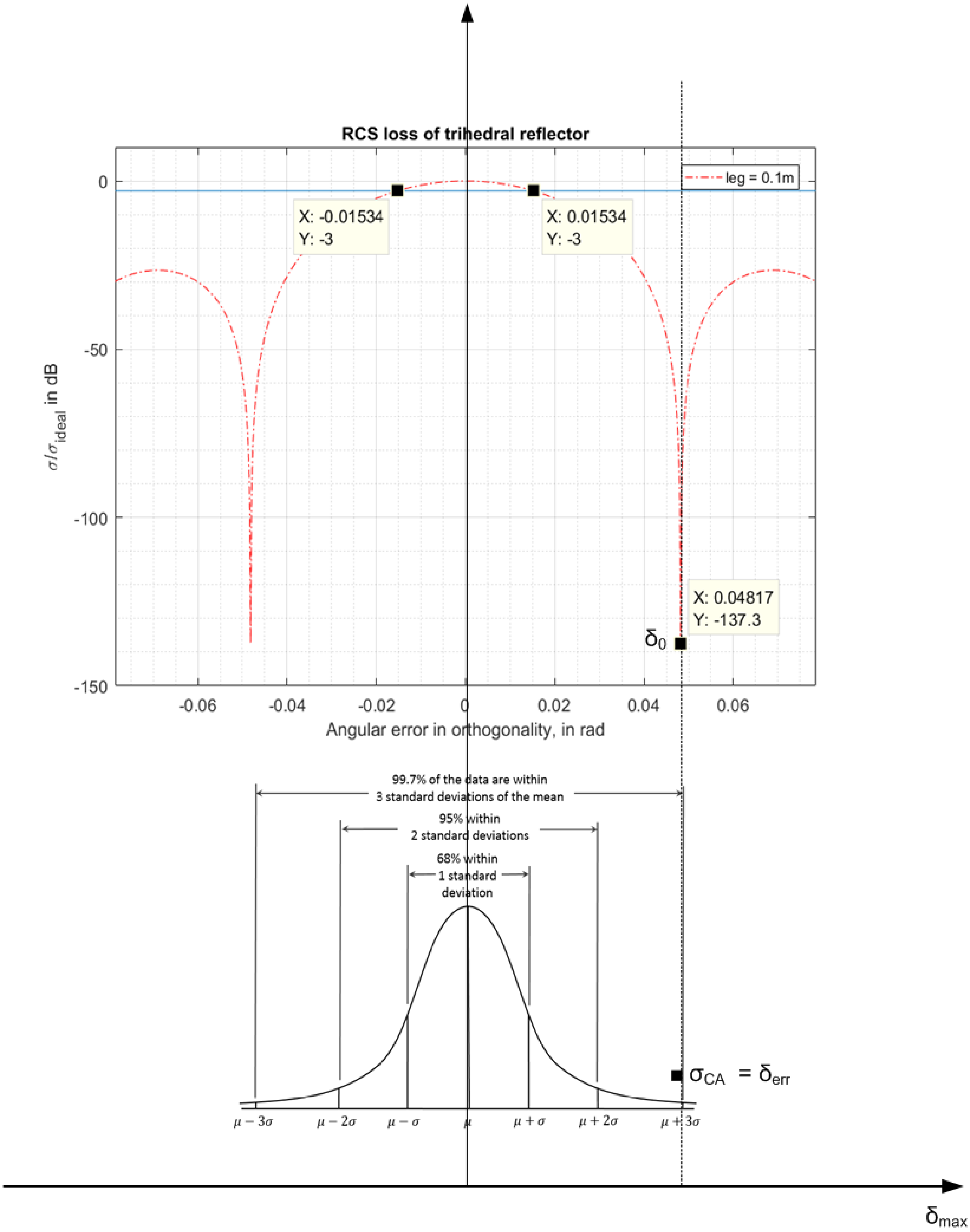

Figure 3.28: RCS loss pattern at leg size $l = 0.10\ m$ and the pdf of normal distribution.

Table 3.2 below gives an overview of the results achieved through Monte-Carlo simulations and from the theory at different leg sizes. To make the comparison easier, figure 3.29 below plots the δ_0 values alongside the δ_{err,max_exp} values at the corresponding leg sizes. It can be said that these two matches quite well with each other.

Table 3.2: $\delta_{err,max}$ **results from simulations and the expected theoretical results** δ_{err,max_exp} **at different leg sizes in a table.**

Leg Size in m	**Max. Allowable Angular Error** $\delta_{err,max}$ **in deg**	**Max. Allowable Angular Error** $\delta_{err,max}$ **in rad**	**First Minimum** δ_0 **in rad**	**Expected Max. Allowable Angular Error** δ_{err,max_exp} **in rad**
0.10 m	0.50 °	0.0087	0.048	$6 \cdot \delta_{err,max} = 0.0524$
0.20 m	0.25 °	0.0044	0.024	$6 \cdot \delta_{err,max} = 0.0262$
0.30 m	0.20 °	0.0035	0.016	$6 \cdot \delta_{err,max} = 0.0209$

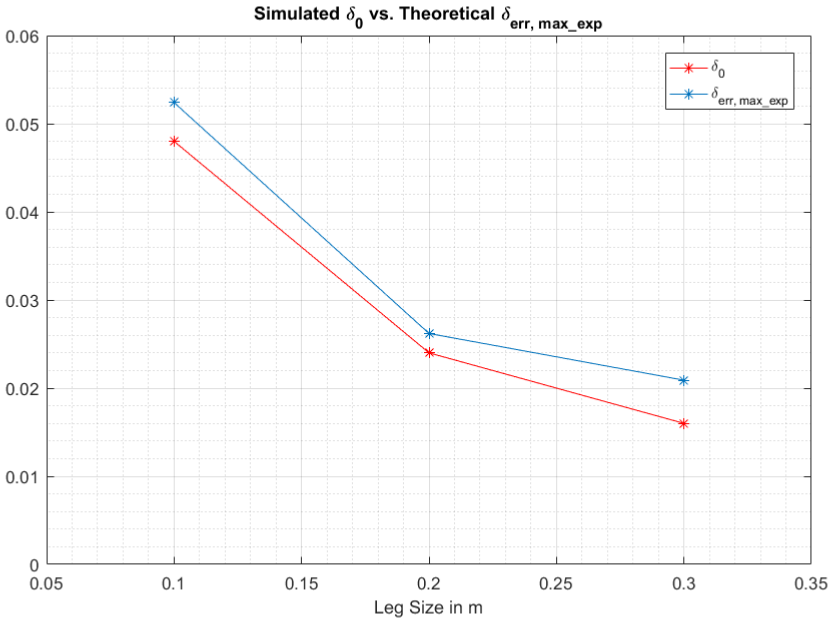

Figure 3.29: δ_0 from the Monte Carlo simulations vs. expected δ_{err,max_exp} values from the theory. Plots show that the two values at a given leg size match quite well.

3.5. RCS Loss Factor due to Total Loss

The total loss factor is obtained by multiplying the two loss factors for orientation errors and non-orthogonality as :

$$L_{total} = L_{ori.} \cdot L_{non.orth} \tag{3.79}$$

In [15], it is proved that the product of independent random beta variables is a beta variable and the formula for the approximate distribution of this beta variable is also given. The distribution of $Z = \prod_{i=1}^{k} X_i$, where X_i's are independent variables with a beta distribution of $Beta(\alpha_i, \beta_i)$, is approximated by the beta distribution of $Beta(\alpha_{apprx}, \beta_{apprx})$. The shape parameters α_{apprx} and β_{apprx} are obtained by :

$$\begin{aligned} \alpha_{apprx} &= \frac{(S-T)\cdot S}{(T-S^2)}, \\ \beta_{apprx} &= \frac{(S-T)\cdot(1-S)}{(T-S^2)}, \end{aligned} \tag{3.80}$$

in which

$$\begin{aligned} S = E(Z) &= \prod_{i=1}^{k} E(X_i) = \prod_{i=1}^{k} \frac{\alpha_i}{\alpha_i+\beta_i}, \\ T = E(Z^2) &= \prod_{i=1}^{k} E(X_i^2) = \prod_{i=1}^{k} \frac{\alpha_i(\alpha_i+1)}{(\alpha_i+\beta_i)(\alpha_i+\beta_i+1)}. \end{aligned} \tag{3.81}$$

Therefore concluded that L_{total} is a beta variable as well.

Next, a beta distribution fit analysis is performed on the distribution of the total loss factor due to orientation errors $L_{ori.}$.

3.5.1. Beta Distribution Fit Analysis on the Histogram of RCS Loss Factor due to Orientation Errors

Assuming that the leg length of the corner reflector has no errors, so therefore accurate, the total loss due to orientation errors can be written as the product of three independent random beta variables:

$$L_{ori.} = L_{elev.} \cdot L_{azi.} \cdot L_{azi.,veh.pos.} \tag{3.82}$$

where, $L_{elev.}$ is the loss factor due to orientation errors in elevation plane, $L_{azi.}$ is the loss factor due to orientation errors in azimuth plane and $L_{azi.,veh.pos.}$ is the loss factor due to errors in the position of vehicles in azimuth plane from which the histograms and the beta distribution fit results have been shown in sections 3.1.1 and 3.2, respectively.

Below the result is given for the beta distribution fit analysis, that is obtained for n=10000 targets evaluated at $f = 77\ GHz$, on the distribution of the total loss factor $L_{ori.,tot.}$ in figure 3.30 at the ideal leg size $l_{ideal} = 0.10\ m$. Also the corresponding shape parameters are given in this figure which follow both from the distribution fit in Matlab itself and from the formula of approximate distribution given in [15].

One can conclude that the approximated shape parameters ($\alpha_{apprx} = 16.1$, $\beta_{apprx} = 0.91$) agree reasonably well with the estimated shape parameters ($\alpha = 20.9$, $\beta = 1.19$).

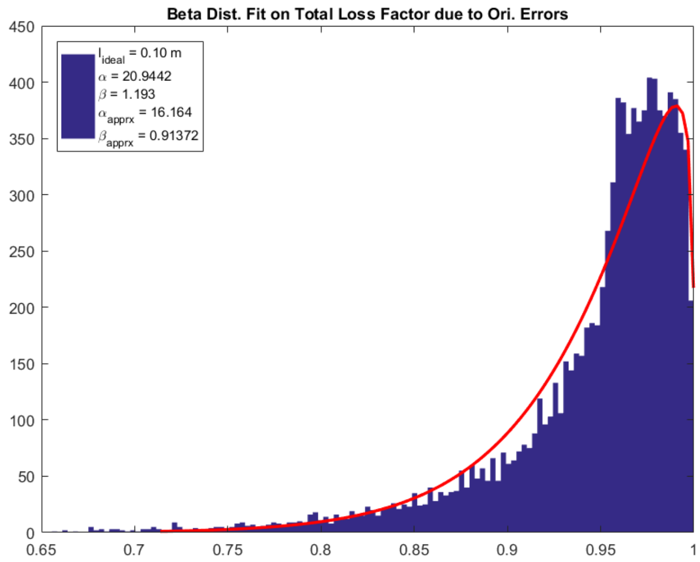

Figure 3.30: Beta distribution fit plot on the distribution of total loss factor due to orientation errors at $l_{ideal} = 0.10\ m$.

3.5.2. Beta Distribution Fit Analysis on the Histogram of Total Loss Factor

Figure 3.31 represents the beta distribution fit results on the distribution of the total loss factor L_{total} from equation (3.79) at leg sizes of $l = 0.10\ m$, $l = 0.20\ m$ and $l = 0.30\ m$ at the corresponding maximum applicable deviation angles of $\delta_{err,max} = 0.50°$, $\delta_{err,max} = 0.25°$ and $\delta_{err,max} = 0.20°$, respectively. Also the corresponding shape parameters are given in the figure which follow both from the distribution fit in Matlab itself and from the formula of the approximate distribution given in [15].

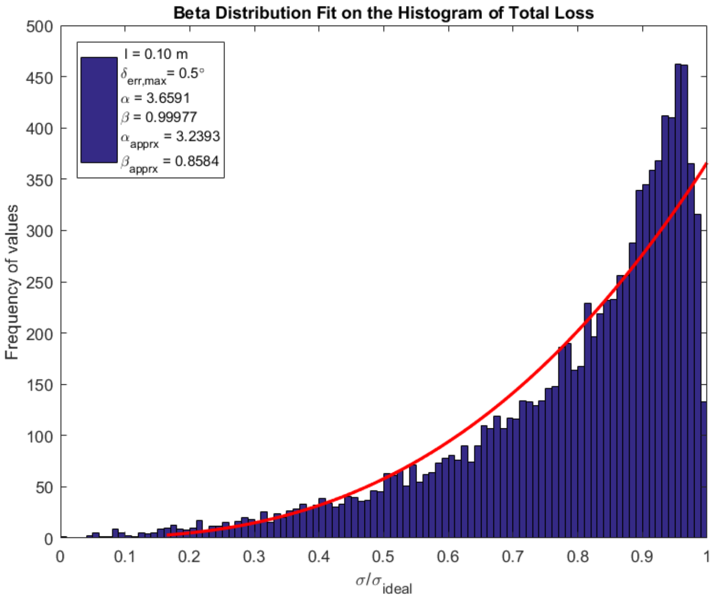

(a) Beta distribution fit for leg length $l = 0.10\ m$ and deviation of $\delta_{err,max} = 0.50°$

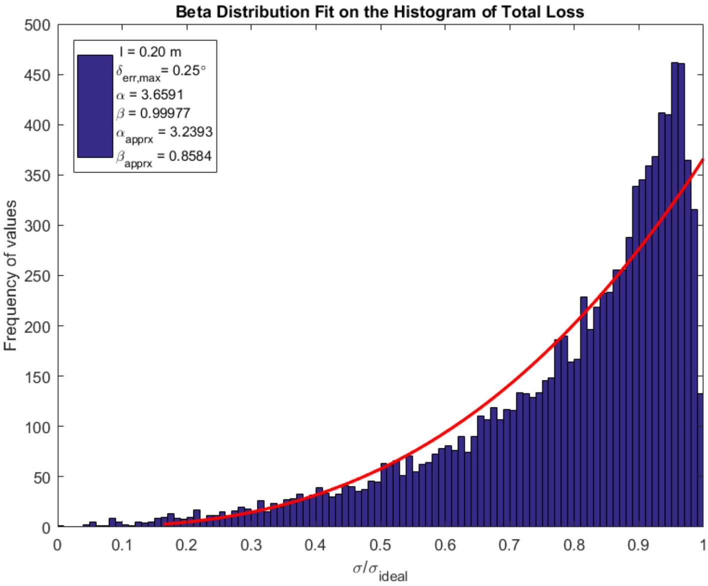

(b) Beta distribution fit for leg length $l = 0.20\ m$ and deviation of $\delta_{err,max} = 0.25°$

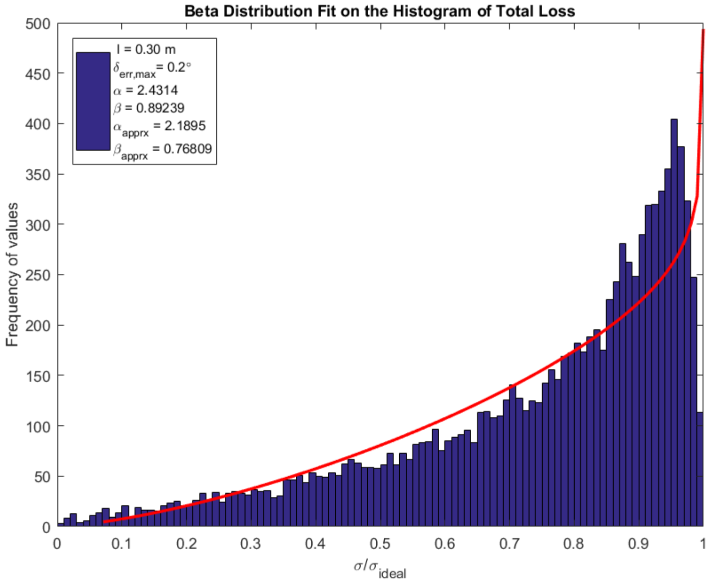

(c) Beta distribution fit for leg length $l = 0.30\ m$ and deviation of $\delta_{err,max} = 0.20°$

Figure 3.31: Beta distribution fit on the histogram of total loss factor at leg sizes of $0.10\ m$, $0.20\ m$ and $0.30\ m$ at deviation angles of $\delta_{err,max} = 0.50°$, $\delta_{err,max} = 0.25°$ and $\delta_{err,max} = 0.20°$, respectively.

Figure 3.32 gives these estimated and approximated shape parameters at the corresponding leg sizes. One can see from the plots that they do not differ from one another significantly.

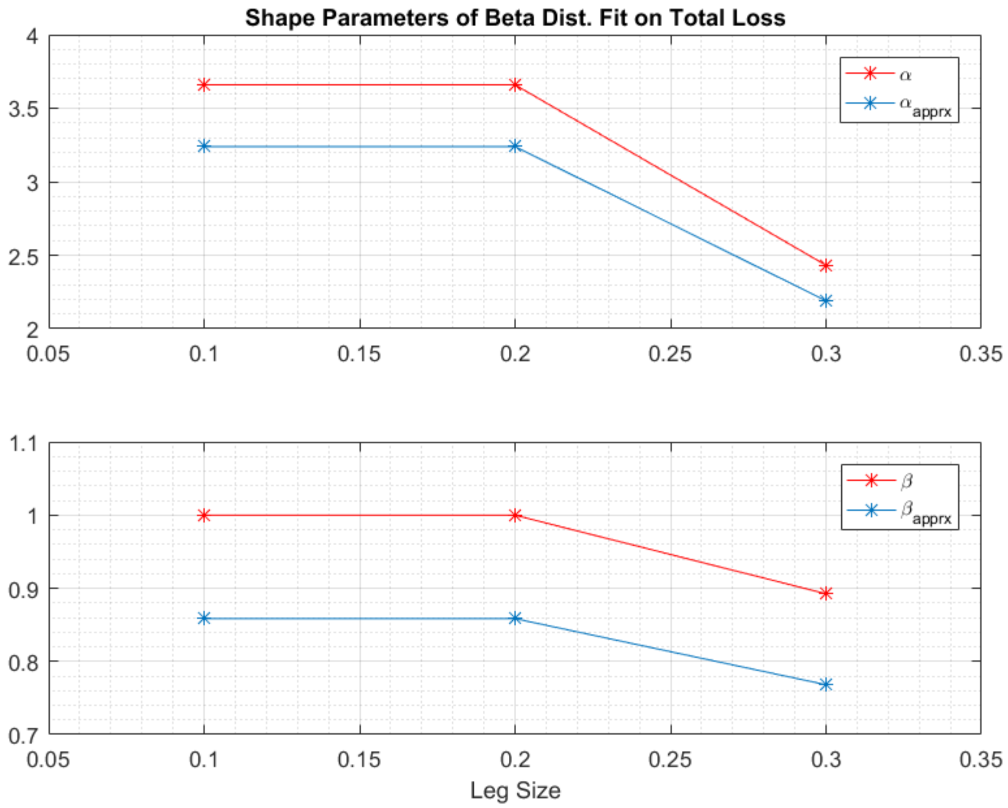

Figure 3.32: Estimated shape parameters vs. approximated shape parameters

3.6. Conclusions

This chapter dealt with the statistical characteristics of the RCS loss in terms of *RCS Loss Factor* for orientation errors, both in elevation and azimuth plane, errors in leg length as well as the non-orthogonality of the corner walls which results from mass production errors.

In case of orientation errors, first, the high-frequency RCS is approximated by means of its Taylor series in the vicinity of the points $\theta = \theta_{ideal}$ and $\phi = \phi_{ideal}$, as given in equations (3.16) and (3.43), respectively. From these results, the probability distributions of the loss factors are derived analytically for errors in elevation and azimuth plane as well as for errors in leg length of the corner reflector, under assumption that deviations from the ideal orientation in elevation and azimuth plane and that the errors in the leg lengths are normal distributed.

Particularly for orientation errors in elevation and azimuth plane, it is shown that the probability distribution of the RCS loss factors can be well approximated by β-distribution for small errors in orientation, for which the loss factor is $L_{ori} \approx 1$. Results are validated both by means of matching shape parameters obtained from the derivations and Monte-Carlo simulation and by means of Kullback-Leibler divergence in which the divergence is shown to go to very low values for small errors in orientation. Therefore, loss factors are concluded to be beta distributed.

Particularly for errors in leg length, after performing a normal distribution fit on the distribution of the loss factor, it is concluded that this pdf might further be approximated by a normal distribution.

In case of errors due to non-orthogonality of the corner walls, based on the formula given in (3.58) and assuming that the angular error is normal distributed, it can be assumed to be normal distributed, it is shown that the probability distribution of the RCS loss factors can be well approximated by β-distribution for small angular errors for which $L_{non.orth.} \approx 1$. Results are validated by means of matching shape parameters obtained from the derivation and Monte-Carlo simulation at small errors. It is noted that as the leg size increases, two curves of shape parameters are becoming apart at smaller values of angular error, which means that the β-distribution approximation is then applicable only for smaller errors.

Production of the trihedral corner reflectors should be at most within 1° of precision in the corner walls since the the formula given in (3.58) is applicable only for angular deviations smaller than 1°. Beta distribution fit analysis showed that beyond a certain amount of angular error, a second peak starts to appear, which are found to be the values as given in table 3.1 for three different leg sizes. From the results in the table concluded that, in contrast to better visibility, bigger size requires higher production precision in terms of the angular error because the second peak appeared earlier when the size of the reflector gets bigger. Also observed that 3-dB beamwidth decreases with the increasing leg size. These two results support the conclusion that the β-distribution approximation is applicable only for increasingly smaller errors when the leg size increases. Furthermore, deviation angles beyond which a second peak starts to appear in the beta distribution fit achieved from the simulations as given in table 3.1 are validated by theory corresponding to the properties of normal distribution to be roughly the good ones as they match quite well as given in figure 3.29. Together with the results obtained in section , results of the statistical characteristics of this loss factor helped to find a balance between the size, quality and number of targets to be deployed in a certain range in a given road configuration.

It is shown that the total loss factor, obtained by product of two independent random beta variables of loss factors $L_{ori.}$ and $L_{non.orth}$, can be approximated by a beta distribution as well. This is shown by means of a comparison between the estimated and approximated shape parameters at the corresponding leg sizes as given in figure 3.32, assuming accurate leg length of the corner reflector.

4

Estimation of the Radar Healthiness Ratio *Q(t,R)*

This chapter deals with defining and the estimation of the quality metric (or quality factor) based on which the healthiness of the automotive radar can be evaluated.

4.1. Defining the Radar Healthiness Ratio Q(t,R)

The radar range equation for automotive FMCW radars in the form of (required) SNR, including the free-space losses, were given in equation 2.12 to be:

$$SNR = \frac{P_r}{P_n} = \frac{P_t G_t G_r \lambda^2 \sigma_{req}}{(4\pi)^3 R^4 k T_0 F B L_{sys}} F_{pr}^4 \cdot (\tau B) \tag{4.1}$$

This equation can be re-arranged by putting all the radar specific constants, losses and the propagation factor in a single variable, called $A(t)$, which results in the following equation:

$$SNR(R) = \frac{A(t,R) \cdot \sigma(\alpha, \theta, \phi, l)}{R^4} \tag{4.2}$$

where

$$A(t,R) = \frac{P_t G^2 \lambda^2}{(4\pi)^3 k T_0 F B L_{sys}} F_{pr}^4 \cdot (\tau B) \tag{4.3}$$

In equation (4.2), $SNR(R)$ is the Signal-to-Noise Ratio being measured on drive, $\sigma(\alpha, \theta, \phi, l)$ is the RCS of the targets encountered on drive and $A(t,R)$ denotes the current state of the radar on the go.

Radar range equation can also be written in the RCS form in terms of the $SNR(R)$ that is produced by the radar. This gives:

$$\sigma_m = \frac{R^4 \cdot SNR(R)}{A_0} \tag{4.4}$$

In equation (4.4), A_0 represents a constant value which comprises the radar specific constants, losses and the propagation factor defined in the production or initial calibration phase at the factory side and σ_m is thus the measured RCS value at the output of the radar in real time based on this A_0 value.

Re-writing equation (4.4) by substituting equation 4.2 into $SNR(R)$ gives:

$$\begin{aligned}\sigma_m &= \frac{R^4}{A_0} \cdot \frac{A(t,R) \cdot \sigma(\alpha,\theta,\phi,l)}{R^4} \\ &= \frac{A(t,R) \cdot \sigma(\alpha,\theta,\phi,l)}{A_0} \\ &= Q(t,R) \cdot \sigma(\alpha,\theta,\phi,l)\end{aligned} \tag{4.5}$$

which is the measurement equation that is used when dealing with the estimation of the quality metric.

Therefore,

$$Q(t,R) = \frac{\sigma_m}{\sigma(\alpha,\theta,\phi,l)} = \frac{A(t,R)}{A_0} \tag{4.6}$$

In equation (4.6), $Q(t,R)$ is thus the quality metric that needs to be estimated.

4.2. Estimation of $Q(t,R)$ by Method of Moments

In equation 4.5, the measurement equation in terms of the quality metric $Q(t,R)$ was derived to be:

$$\sigma_m = Q(t,R) \cdot \sigma(\alpha,\theta,\phi,l) \tag{4.7}$$

where $\sigma(\alpha,\theta,\phi,l)$ is the RCS of the targets encountered on drive that depends on a number of factors such as the range to the target, size, orientation, observation and orthogonality of the corner faces of the target. Assuming accurate leg length l, the range R is known and that the orientation error in azimuth is the only error that affects this RCS, equation (4.7) reduces to:

$$\begin{aligned}\sigma_m &= Q \cdot \sigma(\theta_{ideal},\phi,l_{ideal}) \\ &= Q \cdot \left(L_{azi.} \cdot \sigma_{ideal}(\theta_{ideal},\phi_{ideal},l_{ideal})\right)\end{aligned} \tag{4.8}$$

Given equation (4.8), measurement equation with additive noise can now be written as:

$$\sigma_m = Q \cdot \left(L_{azi.} \cdot \sigma_{ideal}(\theta_{ideal},\phi_{ideal},l_{ideal})\right) + n \tag{4.9}$$

Scaling equation (4.9) by the factor $\sigma_{ideal}(\theta_{ideal},\phi_{ideal},l_{ideal})$ results in:

$$\sigma' = Q \cdot L_{azi.} + n' \tag{4.10}$$

with $\sigma' = \sigma_m/\sigma_{ideal}(\theta_{ideal},\phi_{ideal},l_{ideal})$, and, $n' = n/\sigma_{ideal}(\theta_{ideal},\phi_{ideal},l_{ideal})$. Also note that the loss factor $L_{azi.}$ was determined to be beta distributed with the shape parameters α and β: $L_{azi.} \sim Beta(\alpha,\beta)$.

4.2.1. RCS Fluctuation is a Source of Noise

Assuming there is no additive noise, measurement can be regarded as a scaled beta distribution with four parameters : $\sigma' \sim Beta(\alpha,\beta,a,c)$, where α and β are as usual the shape parameters and a and c are the parameters representing the minimum and maximum values of the distribution, respectively. Note that in our measurement, the parameter $a = 0$ and $c = Q$.

Probability density function of this scaled beta distribution conditioned on the quality factor Q is:

$$p(\sigma'|Q) = \frac{(\sigma')^{\alpha-1}\,(Q-\sigma')^{\beta-1}}{B(\alpha,\beta)\;Q^{(\alpha+\beta-1)}} \tag{4.11}$$

All the four parameters of a scaled beta distribution can be estimated by means of the method of moments by equating sample and population values of the first four central moments; mean, variance, skewness and excess kurtosis [16], [17]. One equation to calculate the estimation of the support interval range $(\hat{Q} - \hat{a})$, in terms of the sample variance and sample excess kurtosis, gives the estimate of parameter Q as:

$$\hat{Q} = \sqrt{(\text{sample variance})}\sqrt{6 + 5\hat{v} + \frac{(2+\hat{v})(3+\hat{v})}{6}(\text{sample excess kurtosis})} \tag{4.12}$$

One another alternative equation to calculate the estimation of the support interval range $(\hat{Q} - \hat{a})$, in terms of the sample variance and sample skewness, gives the estimate of parameter Q as:

$$\hat{Q} = \frac{\sqrt{(\text{sample variance})}}{2}\sqrt{(2+\hat{v})^2\ (\text{sample skewness})^2 + 16(1+\hat{v})} \tag{4.13}$$

where the sample size and sample moments are:

$$\hat{v} = \hat{\alpha} + \hat{\beta} \tag{4.14}$$

$$\text{sample mean} = \bar{y} = \frac{1}{N}\sum_{i=1}^{N} \sigma_i' \tag{4.15}$$

$$\text{sample variance} = \bar{v}_{\sigma'} = \frac{1}{N-1}\sum_{i=1}^{N}(\sigma_i' - \bar{y})^2 \tag{4.16}$$

$$\text{sample skewness} = \frac{N}{(N-1)(N-2)}\frac{\sum_{i=1}^{N}(Y_i - \bar{y})^3}{\bar{v}_Y^{3/2}} \tag{4.17}$$

$$\text{sample excess kurtosis} = \frac{N(N+1)}{(N-1)(N-2)(N-3)}\frac{\sum_{i=1}^{N}(Y_i - \bar{y})^4}{\bar{v}_Y^2} - \frac{3(N-1)^2}{(N-2)(N-3)} \tag{4.18}$$

Note that the estimated shape parameters $\hat{\alpha} = \alpha$ and $\hat{\beta} = \beta$ are gathered from the distribution of $L_{azi.} \sim Beta(\alpha, \beta)$ in the simulation.

4.2.2. Results of the Estimation of Q by Method of Moments

The results of the estimation of the quality factor Q by means of Method of Moments for $N = 5000$ realizations of a corner reflector with leg size $l = 0.10\ m$, evaluated at $f = 77\ GHz$, for different standard deviation values σ_Φ of the orientation error are given in figure 4.1. In the estimation, true quality factor is considered to be constant for all realizations and it is chosen to be $Q_{true} = 0.7$.

One can conclude that the estimation formula in terms of the sample variance and sample skewness from equation (4.13) delivers more accurate estimation results.

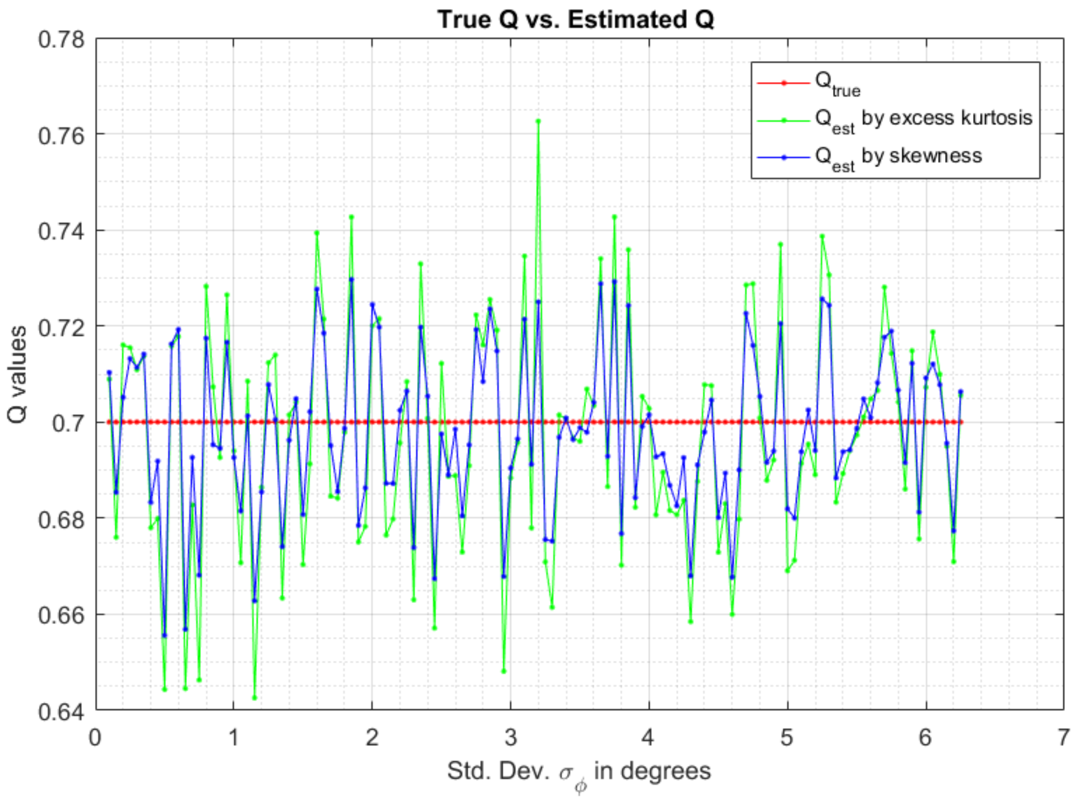

Figure 4.1: True Q-value vs. estimated Q for different values of σ_ϕ.

4.2.3. Mean Squared Error of the MoM Estimation

The mean squared error of the MoM estimation is calculated by:

$$MSE\ (Q_{est}^{(n)}) = \frac{1}{\text{(size of r)}} \sum_{r}^{R} (Q_{est,r}^{(n)} - Q_{true})^2 \tag{4.19}$$

where $n = \{10, 20, 30, ..., N\}$ is the vector containing the number of observations σ_n', and, $r = \{10, 12, 14, ..., R\}$ is the vector containing the number of realizations of the corner reflector.

Note that the vector r does not start to increase from $r = \{1, ...\}$ because of the need for more realizations due to beta distribution fitting operation in the code.

Figure 4.2 give the resulting MSE plot of the MoM estimation as a function of number of observations for both estimators from equations (4.12) and (4.13). There results validate that the estimation formula in terms of the sample variance and sample skewness in equation (4.13) delivers indeed more accurate estimation result than the estimator in equation (4.12). Furthermore, as expected, estimation accuracy improves with the increasing number of observations.

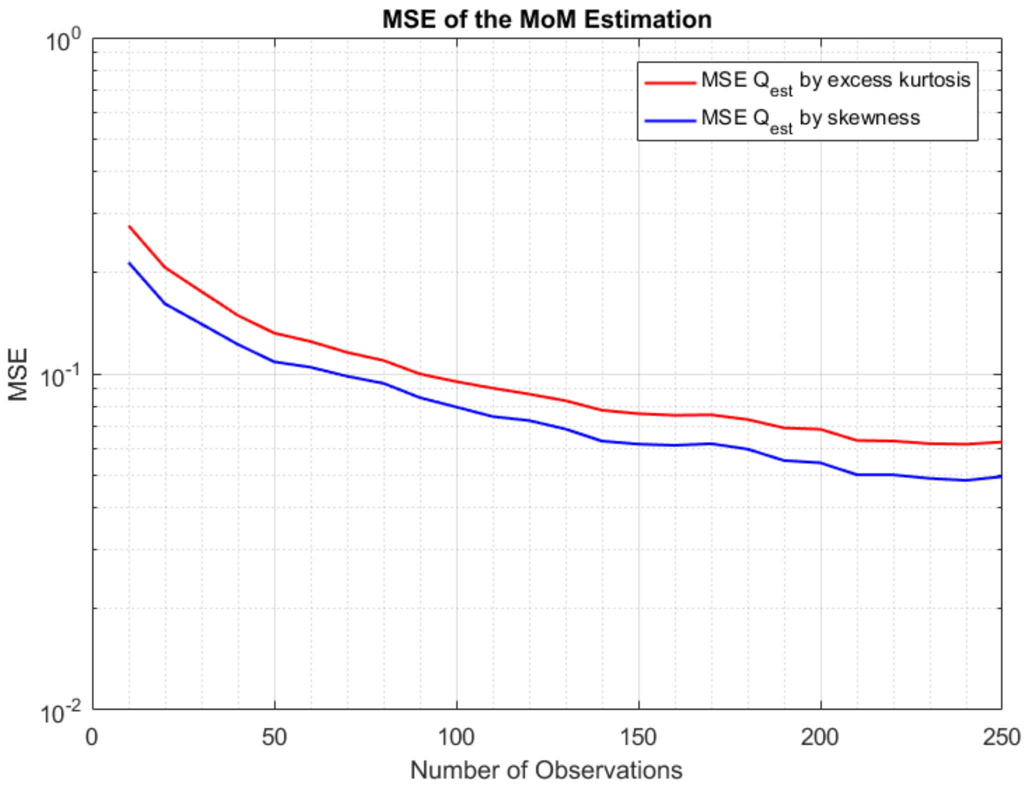

Figure 4.2: MSE of the estimated Q values as a function of the number of observations where $N = 250$ and $R = 20000$.

4.3. Maximum a Posteriori (MAP) Estimation of the Quality Factor Q

In the presence of additive noise, scaled measurement equation is given in (4.10) to be :

$$\sigma' = Q \cdot L_{azi.} + n' \tag{4.20}$$

with the loss factor $L_{azi.} \sim Beta(\alpha, \beta)$. RCS fluctuation now is considered to be a nuisance parameter here.

In case of N measurements of N independent targets, measurement equation becomes:

$$\Sigma = Q \cdot \mathbf{L_{azi}} + \mathbf{n'} \tag{4.21}$$

where $\Sigma = \begin{bmatrix} \sigma'_1 \\ \sigma'_2 \\ . \\ . \\ \sigma'_N \end{bmatrix}$, $\mathbf{L_{azi}} = \begin{bmatrix} L_{azi.,1} \\ L_{azi.,2} \\ . \\ . \\ L_{azi.,N} \end{bmatrix}$, and, $\mathbf{n'} = \begin{bmatrix} n'_1 \\ n'_2 \\ . \\ . \\ n'_N \end{bmatrix}$

For high SNR, noise can be assumed Gaussian as well as the distribution of the power. Therefore the pdf of the measurements that are conditioned on the scalar quality factor Q and the loss factors $L_{azi.,i}$, $i = 1, ..., N$, from the corresponding independent targets follows as :

$$p(\Sigma|Q,\mathbf{L_{azi}}) = \frac{1}{(2\pi\sigma_n^2)^{\frac{N}{2}}} \exp\Big[-\frac{1}{2\sigma_n^2}\sum_{i=1}^{N}(\sigma_i' - Q\,L_{azi.,i})^2\Big] \tag{4.22}$$

Since we are interested in the estimation of quality factor Q only, it is convenient to treat the loss factors $\mathbf{L_{azi}}$ as a nuisance parameter and to integrate it out by means of Bayesian approach.

The posterior pdf of the quality factor Q in the vector form is :

$$p(Q|\Sigma) = \frac{p(\Sigma|Q)\,p(Q)}{p(\Sigma)} \tag{4.23}$$

with

$$p(\Sigma|Q) = \int p(\Sigma|Q,\mathbf{L_{azi}})\,p(\mathbf{L_{azi}})\,d\mathbf{L_{azi}} \tag{4.24}$$

being the likelihood by which the loss factors $\mathbf{L_{azi}}$ are integrated out, and,

$$p(\Sigma) = \int p(\Sigma|Q)p(Q)dQ \tag{4.25}$$

being the marginal likelihood which normalizes the posterior density $p(Q|\Sigma)$.

The joint distribution of the loss factors from the corresponding independent targets in equation (4.21) is:

$$p(\mathbf{L_{azi}}) = \prod_{i=1}^{N} p(L_{azi.,i}) = \prod_{i=1}^{N} \frac{L_{azi.,i}^{\alpha-1}(1-L_{azi.,i})^{\beta-1}}{B(\alpha,\beta)}, \quad L_{azi.,i} \in [0,1], \tag{4.26}$$

and the normal distributed prior pdf of the quality factor Q is:

$$\begin{aligned} p(Q) &= \mathcal{N}(Q_0,\sigma_Q^2) \\ &= \frac{1}{\sqrt{2\pi\sigma_Q^2}}\exp\Big[-\frac{1}{2\sigma_Q^2}(Q-Q_0)^2\Big] \end{aligned} \tag{4.27}$$

Now from equations (4.22) and (4.26), the likelihood equation in (4.24) becomes :

$$p(\Sigma|Q) = \int \frac{1}{(2\pi\sigma_n^2)^{\frac{N}{2}}}\exp\Big[-\frac{1}{2\sigma_n^2}\sum_{i=1}^{N}(\sigma_i' - Q\,L_{azi.,i})^2\Big] \prod_{i=1}^{N} \frac{L_{azi.,i}^{\alpha-1}(1-L_{azi.,i})^{\beta-1}}{B(\alpha,\beta)}\,d\mathbf{L_{azi}}, \quad L_{azi.,i} \in [0,1] \tag{4.28}$$

From this result follows that the MAP estimation of Q requests the following equation to be solved:

$$\begin{aligned} \hat{Q}_{MAP} &= \arg\max_{Q}\Big\{p(\Sigma|Q)p(Q)\Big\} \\ &= \arg\max_{Q}\Big\{\int \frac{1}{(2\pi\sigma_n^2)^{\frac{N}{2}}}\exp\Big[-\frac{1}{2\sigma_n^2}\sum_{i=1}^{N}(\sigma_i' - Q\,L_{azi.,i})^2\Big]\prod_{i=1}^{N}\frac{L_{azi.,i}^{\alpha-1}(1-L_{azi.,i})^{\beta-1}}{B(\alpha,\beta)}\,d\mathbf{L_{azi}} \\ &\cdot \frac{1}{\sqrt{2\pi\sigma_Q^2}}\exp\Big[-\frac{1}{2\sigma_Q^2}(Q-Q_0)^2\Big]\Big\}, \quad L_{azi.,i} \in [0,1] \end{aligned} \tag{4.29}$$

Since equation (4.29) can be quite complex to solve, for convenience ***N measurements of the realization of a single target*** are considered. In that case, the measurement equation becomes :

$$\Sigma = Q \cdot L_{azi} + \mathbf{n'} \tag{4.30}$$

where $\Sigma = \begin{bmatrix} \sigma'_1 \\ \sigma'_2 \\ . \\ . \\ \sigma'_N \end{bmatrix}$, $\mathbf{n'} = \begin{bmatrix} n'_1 \\ n'_2 \\ . \\ . \\ n'_N \end{bmatrix}$ and the loss factor L_{azi} is now a constant parameter.

Then the pdf of the measurements that are conditioned on the scalar quality factor Q and the constant loss factor $L_{azi.}$ follows as :

$$p(\Sigma|Q, L_{azi.}) = \frac{1}{(2\pi\sigma_n^2)^{\frac{N}{2}}} \exp\Big[-\frac{1}{2\sigma_n^2}\sum_{i=1}^{N}(\sigma'_i - Q\ L_{azi.})^2\Big] \tag{4.31}$$

For one target only, the distribution of the loss factor is simply :

$$p(L_{azi.}) = \frac{L_{azi.}^{\alpha-1}(1-L_{azi.})^{\beta-1}}{B(\alpha,\beta)}, \quad L_{azi.} \in [0,1], \tag{4.32}$$

Now from equations (4.31) and (4.32), the likelihood equation becomes :

$$\begin{aligned} p(\Sigma|Q) &= \int p(\Sigma|Q, L_{azi})\ p(L_{azi})\ dL_{azi} \\ &= \int \frac{1}{(2\pi\sigma_n^2)^{\frac{N}{2}}} \exp\Big[-\frac{1}{2\sigma_n^2}\sum_{i=1}^{N}(\sigma'_i - Q\ L_{azi.})^2\Big]\ \frac{L_{azi.}^{\alpha-1}(1-L_{azi.})^{\beta-1}}{B(\alpha,\beta)}\ dL_{azi}, \quad L_{azi.} \in [0,1] \end{aligned} \tag{4.33}$$

The integral in the likelihood function from equation (4.33) for single target measurements can approximately be written as a summation which results into:

$$\begin{aligned} p(\Sigma|Q) &\approx \sum_{k=1}^{m} p(\Sigma|Q, L_{azi,k})\ p(L_{azi,k})\ \delta L_{azi.} \\ &\approx \sum_{k=1}^{m} \Big(\frac{1}{(2\pi\sigma_n^2)^{\frac{N}{2}}} \exp\Big[-\frac{1}{2\sigma_n^2}\sum_{i=1}^{N}(\sigma'_i - Q\ L_{azi,k})^2\Big]\ \frac{L_{azi,k}^{\alpha-1}(1-L_{azi,k})^{\beta-1}}{B(\alpha,\beta)}\ \delta L_{azi.}\Big) \end{aligned} \tag{4.34}$$

where $L_{azi,k} = \delta L_{azi.} \cdot k$, and, $\delta L_{azi.} = \frac{1}{m}$ since $L_{azi.} \in [0,1]$.

From these equations follow that the MAP estimation of Q requests the following equation to be solved:

$$
\begin{aligned}
\hat{Q}_{MAP} &= \arg\max_{Q} \Big\{ p(\Sigma|Q)p(Q) \Big\} \\
&= \arg\max_{Q} \Big\{ \int \frac{1}{(2\pi\sigma_n^2)^{\frac{N}{2}}} \exp\Big[-\frac{1}{2\sigma_n^2}\sum_{i=1}^{N}(\sigma_i' - Q\,L_{azi.})^2\Big] \frac{L_{azi.}^{\alpha-1}(1-L_{azi.})^{\beta-1}}{B(\alpha,\beta)}\, dL_{azi} \\
&\quad \cdot \frac{1}{\sqrt{2\pi\sigma_Q^2}} \exp\Big[-\frac{1}{2\sigma_Q^2}(Q-Q_0)^2\Big] \Big\} \\
&\approx \arg\max_{Q} \Big\{ \Big[\sum_{k=1}^{m} \Big(\frac{1}{(2\pi\sigma_n^2)^{\frac{N}{2}}} \exp\Big[-\frac{1}{2\sigma_n^2}\sum_{i=1}^{N}(\sigma_i' - Q\,L_{azi,k})^2\Big] \; \frac{L_{azi,k}^{\alpha-1}(1-L_{azi,k})^{\beta-1}}{B(\alpha,\beta)}\, \delta L_{azi.} \Big) \Big] \\
&\quad \cdot \frac{1}{\sqrt{2\pi\sigma_Q^2}} \exp\Big[-\frac{1}{2\sigma_Q^2}(Q-Q_0)^2\Big] \Big\}, \quad L_{azi.} \in [0,1]
\end{aligned}
\tag{4.35}
$$

Figure 4.3a below give the plots of the likelihood functions $p(\Sigma|Q)$ from equation (4.34) for different discretization values $\delta L_{azi.}$ where SNR = 30 dB and the true quality factor Q_{true} in the simulation is assumed to be $Q_{true} = 1$. Discretization value $\delta L_{azi.}$ has clearly no impact on the position of the maxima of the likelihood functions. Figure 4.3b gives the plots of the likelihood functions for different SNR values when discretization value is $\delta L_{azi.} = 1e-2$. Reducing the SNR value causes the position of the maxima of the likelihood functions to shift slighty away to right side.

Note that SNR here is defined to be the ratio of the power in true value of Q to the power in noise; i.e. $\frac{P_{Q_{true}}}{\sigma_n^2} = 30\ dB$. These results are obtained for $N = 10$ measurements of the realization of a single target where the error in orientation is taken to be $\sigma_\phi = 3.0°$.

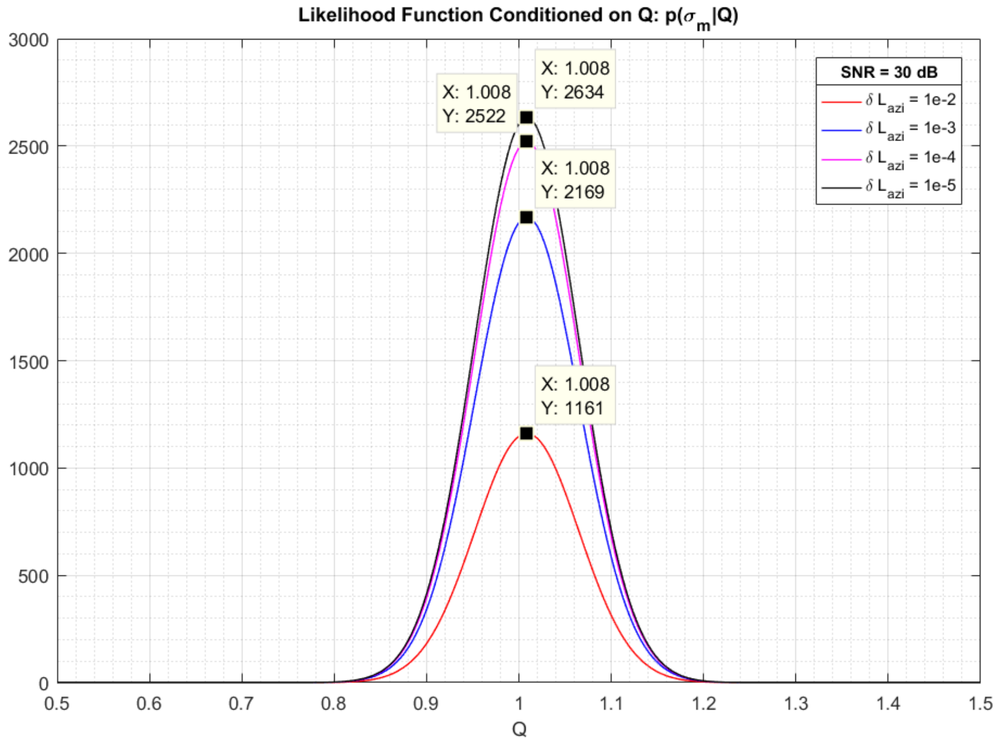

(a) $p(\Sigma|Q)$ for different discretization values $\delta L_{azi.}$ when SNR = 30 dB and Q_{true} = 1.

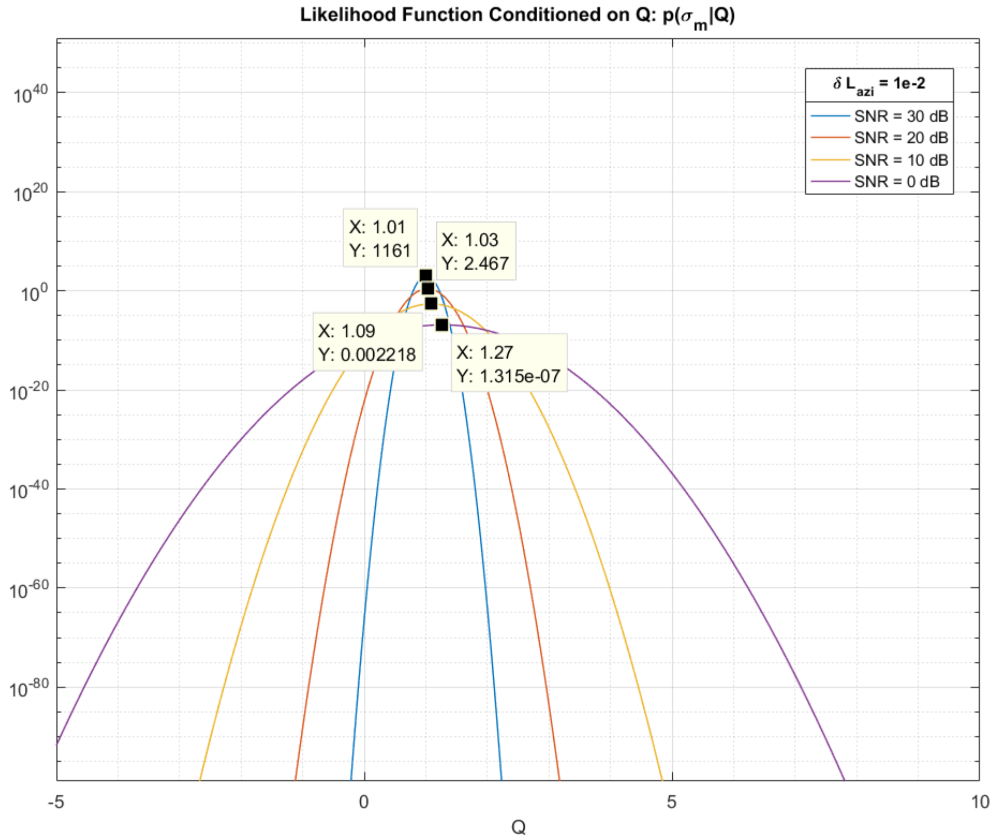

(b) $p(\Sigma|Q)$ for different SNR values at the discretization value $\delta L_{azi.} = 1e-2$ and Q_{true} = 1.

Figure 4.3: Likelihood Functions $p(\Sigma|Q)$

In figure 4.4, the plot of the relative errors in the position of the maxima of the likelihood functions as a function of SNR is given when two different discretization values $\delta L_{azi.}$ are considered. It is clear that the relative error decreases with the increasing SNR for both discretization values. One can conclude, therefore, that the noise power has much more impact on the error than the discretization errors.

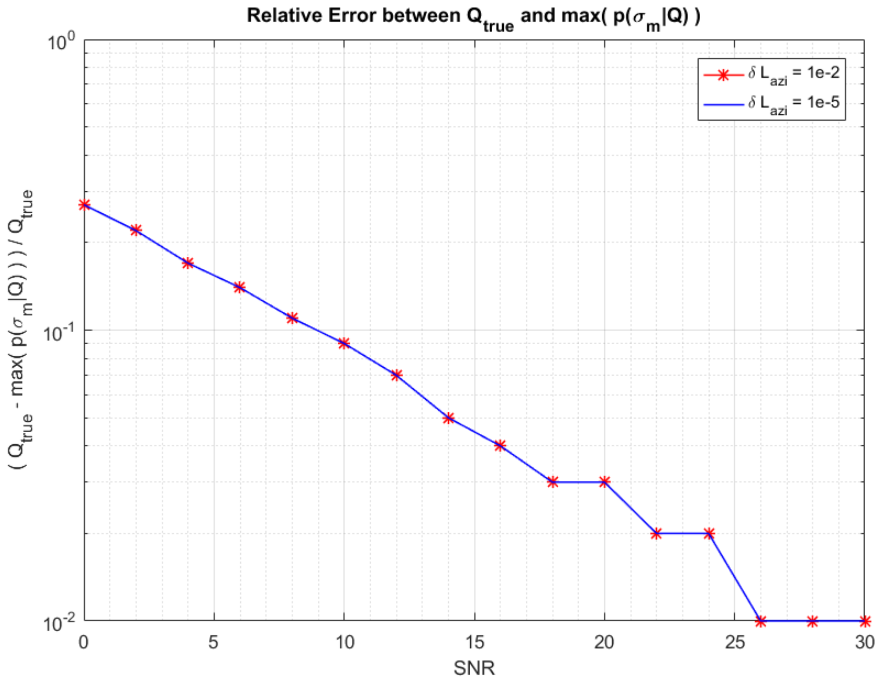

Figure 4.4: Relative errors in $p(\Sigma|Q)$ as a function of SNR, for the two given discretization values $\delta L_{azi.}$ and $Q_{true} = 1$.

In figure 4.5, the plots of the posterior pdf's $p(Q|\Sigma)$ are given for different SNR values for the given discretization value $\delta L_{azi.} = 1e-2$, where the prior pdf of the quality factor Q is taken to be normal distributed as $p(Q) = \mathcal{N}(Q_0, \sigma_Q^2) = (15, 10^2)$. Decreasing SNR value, as it was the case for the likelihood functions from figure 4.3b as well, causes the position of the maxima of the posterior pdf's to shift slighty away to right side.

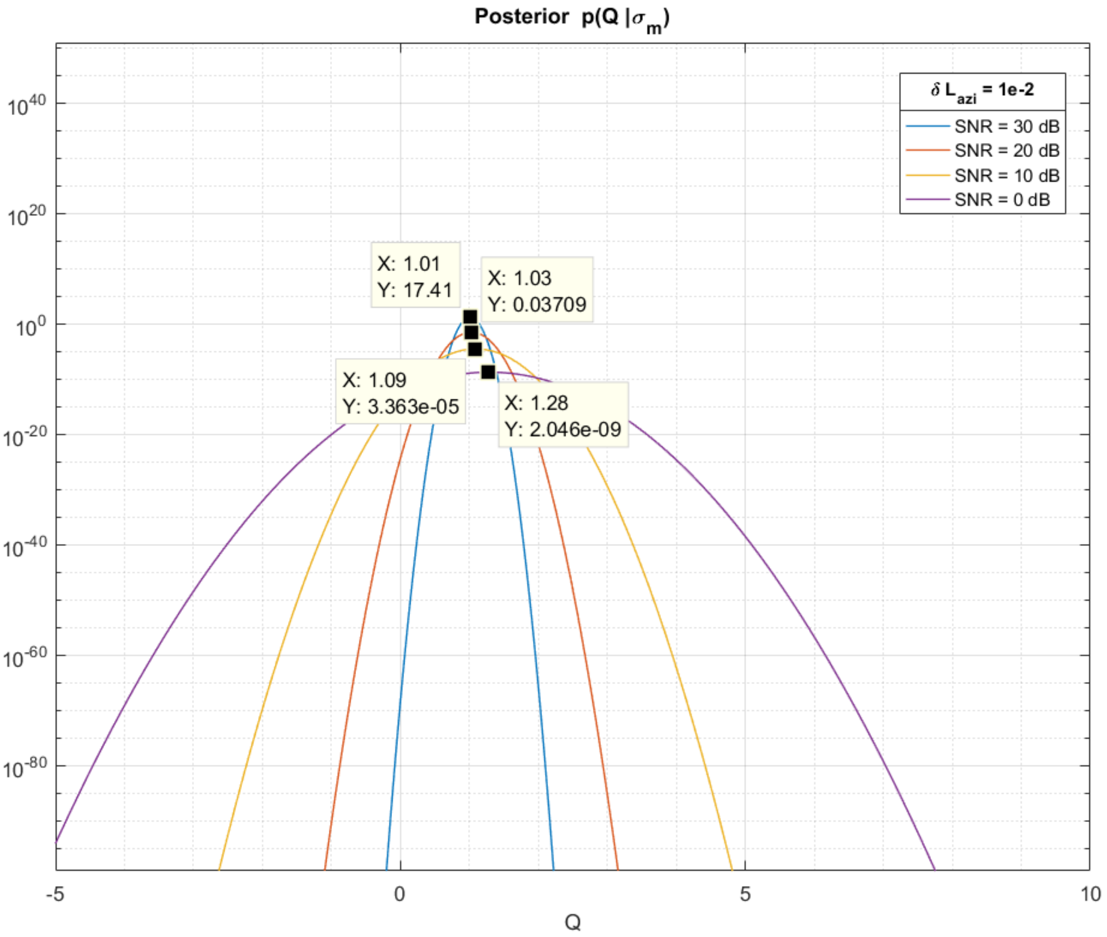

Figure 4.5: Posterior pdf's for different SNR values for the two given discretization values $\delta L_{azi.}$ and $Q_{true} = 1$.

Finally, taking the derivative of the argument $\left(p(\Sigma|Q)p(Q)\right)$ in equation (4.35) with respect to Q using the product rule and setting this result equal to zero gives the analytical equation that needs to be solved to gather the MAP estimator of the quality factor Q:

$$\begin{aligned}
&\left.\frac{\partial\left(p(\Sigma|Q)p(Q)\right)}{\partial Q}\right|_{Q=\hat{Q}_{MAP}} = \\
&\left.\frac{\partial\, p(\Sigma|Q)}{\partial Q} \cdot p(Q) + p(\Sigma|Q) \cdot \frac{\partial\, p(Q)}{\partial Q}\right|_{Q=\hat{Q}_{MAP}} = \\
&\sum_{k=1}^{m} \left(\frac{1}{(2\pi\sigma_n^2)^{\frac{N}{2}}} \exp\left[-\frac{1}{2\sigma_n^2} \sum_{i=1}^{N} (\sigma_i' - Q\, L_{azi,k})^2 \right] \frac{L_{azi,k}^{\alpha-1}(1-L_{azi,k})^{\beta-1}}{B(\alpha,\beta)}\, \delta L_{azi} \right) \\
&\cdot \left\{ \frac{1}{\sqrt{2\pi\sigma_Q^2}} \exp\left[-\frac{1}{2\sigma_Q^2}(Q-Q_0)^2 \right] \cdot \left(\sum_{k=0}^{m} \left(\frac{L_{azi,k}}{\sigma_n^2} \sum_{i=1}^{N} (\sigma_i' - Q\, L_{azi,k}) \right) - \frac{1}{\sigma_Q^2}(Q-Q_0) \right) \right\} \Bigg|_{Q=\hat{Q}_{MAP}} = 0
\end{aligned} \tag{4.36}$$

Solving this equation to find zero reduces to solving for the second term inside the curly braces, since the first multiplier term in equation (4.36) will be greater than zero. Therefore,

$$\frac{1}{\sqrt{2\pi\sigma_Q^2}} \exp\left[-\frac{1}{2\sigma_Q^2}(Q-Q_0)^2 \right] \cdot \left(\sum_{k=0}^{m} \left(\frac{L_{azi,k}}{\sigma_n^2} \sum_{i=1}^{N} (\sigma_i' - Q\, L_{azi,k}) \right) - \frac{1}{\sigma_Q^2}(Q-Q_0) \right) \Bigg|_{Q=\hat{Q}_{MAP}} = 0 \tag{4.37}$$

Considering the case of ***N measurements of the same realization of a single target***, an evaluation of the estimator performance in terms of estimation error is made by means of Monte Carlo simulation for different SNR values, orientation errors σ_ϕ, prior pdf's $p(Q)$ and number of measurements N. The results are given in figures 4.6 through 4.9 below.

Figure 4.6 gives the plots of the histogram and variance of the estimation error, which is defined as the difference between $\hat{Q}_{MAP}$ and Q_{true}; i.e. $Q_{err} = \hat{Q}_{MAP} - Q_{true}$, for different SNR values after running the estimator for $M = 500$ Monte-Carlo trials. This result is obtained for $N = 10$ measurements of the realization of a single target where the error in orientation $\sigma_\phi = 3.0°$, discretization value $\delta L_{azi.} = 1e-2$, the normal distributed prior pdf $p(Q) = \mathcal{N}(15, 10^2)$. The true quality factor Q_{true} in the simulation is assumed to be $Q_{true} = 1$.

As expected, the histogram of the estimation error Q_{err} gets narrower at higher SNR values, which means that the noise power has a significant impact on the performance of the MAP estimator. This conclusion can also be drawn from the decrease in variance of the estimation error with the SNR increasing as given in figure 4.6b. Also, mean of the estimation error is found to be around zero in all the four cases considered, i.e. $E[Q_{err}] \approx 0$.

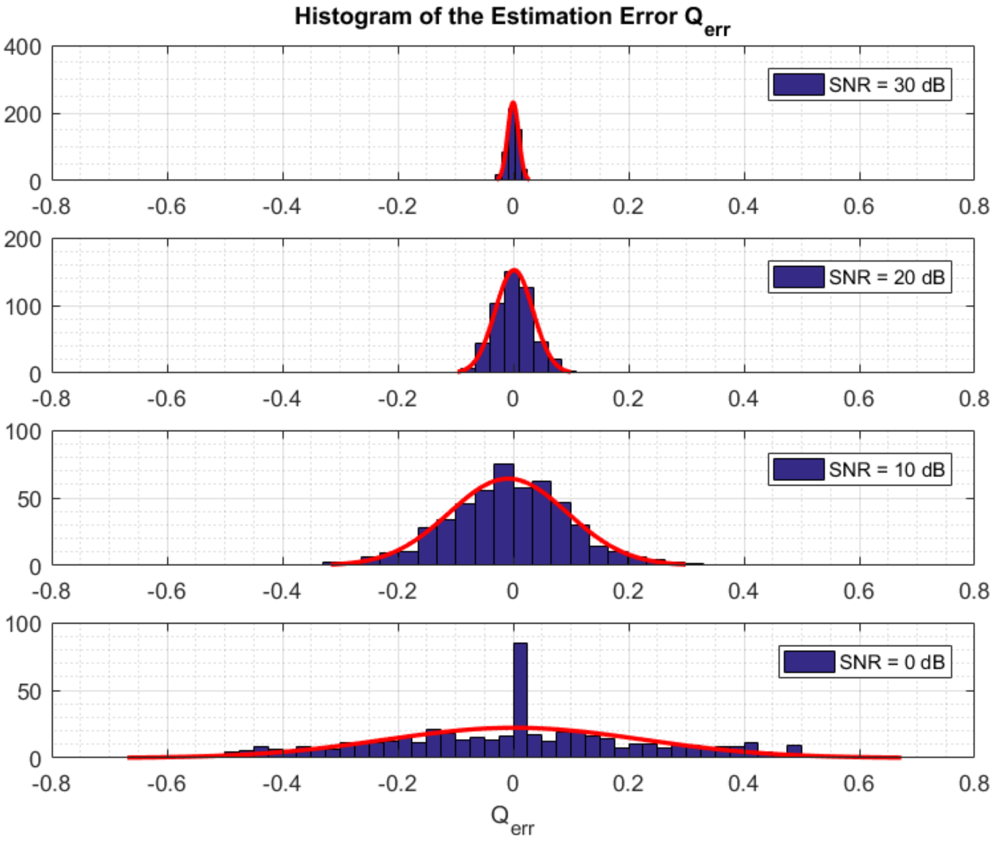

(a) Histograms of the estimation errors for four different SNR values; $SNR = 0\ dB$, $SNR = 10\ dB$, $SNR = 20\ dB$, $SNR = 30\ dB$, after $M = 500$ Monte-Carlo trials.

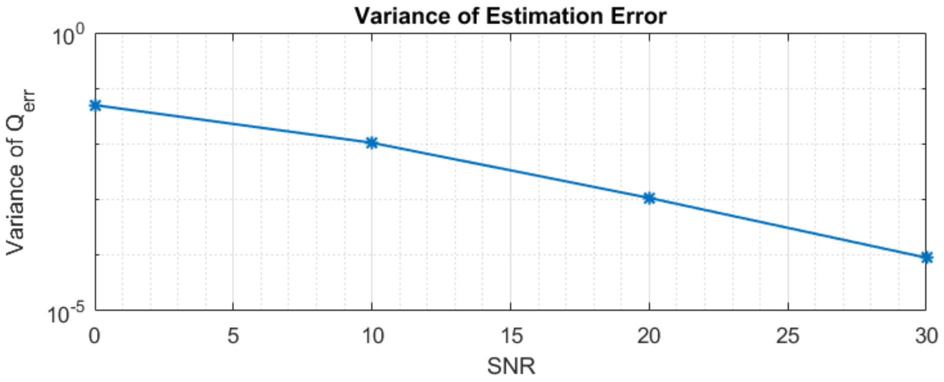

(b) Variance of the estimation errors for the four given SNR values.

Figure 4.6: An evaluation of the estimation error Q_{err} for different SNR values.

Figure 4.7 gives the result of the evaluation of the estimation error Q_{err} for four different orientation errors σ_{ϕ} after running the estimator for $M = 500$ Monte-Carlo trials. This result is again obtained for $N = 10$ measurements of the realization of a single target where the discretization value $\delta L_{azi.} = 1e-2$, the normal distributed prior pdf $p(Q) = \mathcal{N}(15, 10^2)$ and the $SNR = 30\ dB$. The true quality factor Q_{true} in the simulation is again assumed to be $Q_{true} = 1$.

From the rather constant behaviour of the variance of the estimation error can be seen that, for equal SNR, orientation error σ_{ϕ} has no significant impact on the distribution of the estimation error, which means, given correct information about potential losses $L_{azi.}$, estimator shows comparable performance for equal SNR. From this evaluation, the mean of the estimation error is found to be around zero in all the four cases considered, i.e. $E[Q_{err}] \approx 0$. Therefore, one can conclude that the impact of the noise power on the performance of MAP estimator is way bigger than the impact of the loss factor $L_{azi.}$.

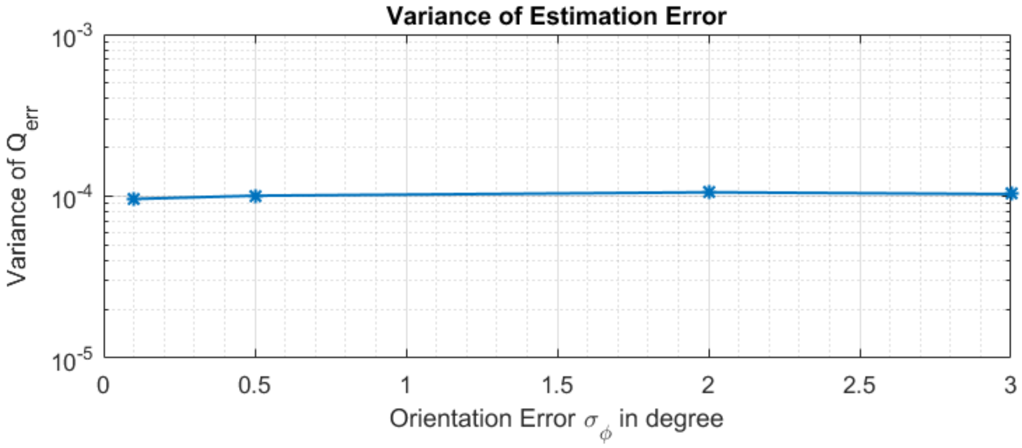

Figure 4.7: Variance of the estimation errors for four different orientation errors; $\sigma_{\phi} = 0.1°$, $\sigma_{\phi} = 0.5°$, $\sigma_{\phi} = 1.0°$, $\sigma_{\phi} = 3.0°$, after $M = 500$ Monte-Carlo trials.

Figure 4.8 gives the results of the evaluation of the estimation error Q_{err} for different normal distributed prior pdf's $p(Q) = \mathcal{N}(Q_0, \sigma_Q^2)$ after running the estimator for $M = 500$ Monte-Carlo trials. This result is again obtained for $N = 10$ measurements of the realization of a single target where the error in orientation $\sigma_\phi = 3.0°$, the discretization value $\delta L_{azi.} = 1e-2$ and the $SNR = 30\ dB$. The true quality factor Q_{true} in the simulation is again assumed to be $Q_{true} = 1$.

The variances of the estimation error seem to be very close to one another both for different standard deviations σ_Q when the mean value Q_0 is fixed and for the same standard deviations σ_Q when the mean value Q_0 is changed from one value to another. From this rather constant behaviour of the variances of the estimation error can be seen that, given correct information on the quality factor Q in terms of prior pdf, estimator shows comparable performance for equal SNR. The mean of the estimation error is again found to be around zero in all the cases considered in this particular evaluation.

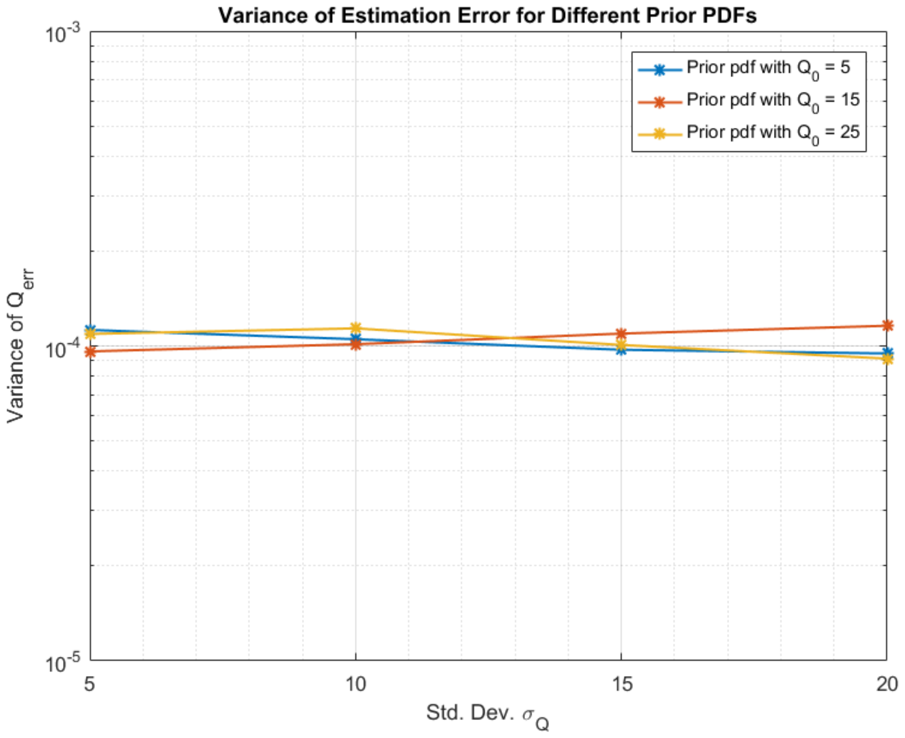

Figure 4.8: Variances of the estimation errors for twelve different prior pdf's from the combination of three different mean values Q_0 and four different standard deviation values σ_Q.

Figure 4.9 gives the plots of the histograms, mean and variance of the estimation error Q_{err} obtained for four different number of measurements, i.e. $N = 10$, $N = 100$, $N = 200$ and $N = 500$, of the realization of a single target after running the estimator for $M = 500$ Monte-Carlo trials. Here the error in orientation $\sigma_\phi = 3.0°$, the discretization value $\delta L_{azi.} = 1e-2$ and the $SNR = 30\ dB$. The true quality factor Q_{true} in the simulation is again assumed to be $Q_{true} = 1$.

As expected, taking more measurements improves the performance of the estimator as can be seen from the histogram of the estimation error Q_{err} getting narrower with increasing amount of measurements. This can also be seen from the decrease in variance of the estimation error with the number of measurements N increasing as given in figure 4.9b. The mean of the estimation error is again found to be around zero in all the four cases considered.

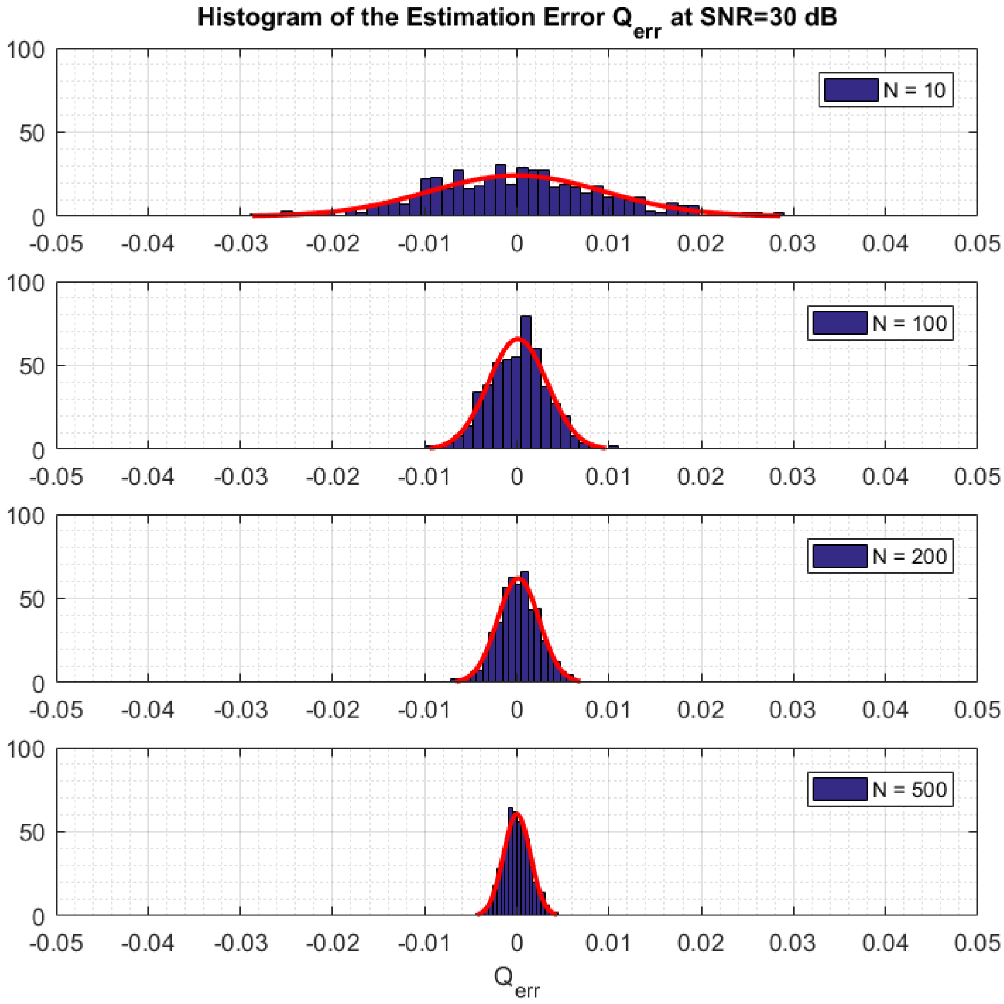

(a) Histograms of the estimation errors for four different number of measurements; $N = 10$, $N = 100$, $N = 200$ and $N = 500$, after $M = 500$ Monte-Carlo trials.

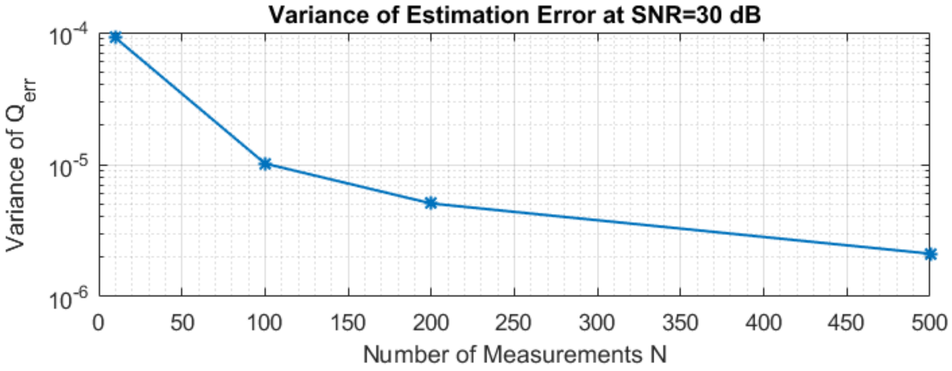

(b) Variance of the estimation errors for the four given different number of measurements.

Figure 4.9: An evaluation of the estimation error Q_{err} for different number of measurements.

4.4. Maximum Likelihood Estimation (MLE) of the Quality Factor Q

Assuming the case when no prior information on the quality factor Q is available, then, considering the case of ***N measurements of the same realization of a single target***, one can perform a MLE estimation of parameter Q :

$$
\begin{aligned}
\hat{Q}_{MLE} &= \arg\max_{Q} \left\{ p(\Sigma|Q) \right\} \\
&\approx \arg\max_{Q} \left\{ \sum_{k=1}^{m} \left(\frac{1}{(2\pi\sigma_n^2)^{\frac{N}{2}}} \exp\left[-\frac{1}{2\sigma_n^2} \sum_{i=1}^{N} (\sigma_i' - Q\, L_{azi,k})^2 \right] \frac{L_{azi,k}^{\alpha-1}(1-L_{azi,k})^{\beta-1}}{B(\alpha,\beta)}\, \delta L_{azi.} \right) \right\}.
\end{aligned}
\tag{4.38}
$$

Taking the derivative of the argument with respect to Q and setting this result equal to zero gives the analytical equation that needs to be solved to obtain the MLE estimator of the quality factor Q:

$$
\begin{aligned}
&\frac{\partial\big(p(\Sigma|Q)\big)}{\partial Q}\Big|_{Q=\hat{Q}_{MLE}} = \\
&\left[\sum_{k=1}^{m} \left(\frac{1}{(2\pi\sigma_n^2)^{\frac{N}{2}}} \exp\left[-\frac{1}{2\sigma_n^2} \sum_{i=1}^{N} (\sigma_i' - Q\, L_{azi,k})^2 \right] \frac{L_{azi,k}^{\alpha-1}(1-L_{azi,k})^{\beta-1}}{B(\alpha,\beta)}\, \delta L_{azi.} \right) \right] \\
&\cdot \left[\sum_{k=1}^{m} \left(\frac{L_{azi,k}}{\sigma_n^2} \sum_{i=1}^{N} (\sigma_i' - Q\, L_{azi,k}) \right) \right] \Big|_{Q=\hat{Q}_{MAP}} = 0
\end{aligned}
\tag{4.39}
$$

An evaluation of the estimator performance in terms of estimation error is made by means of Monte Carlo simulation for different SNR values, orientation errors σ_ϕ and number of measurements N. The results are given in figures 4.10 through 4.12 below.

Figure 4.10 gives the plots of the histograms and variance of the estimation error Q_{err} for different SNR values after running the estimator for $M = 500$ Monte-Carlo trials. This result is obtained for $N = 10$ measurements of the realization of a single target where the error in orientation $\sigma_\phi = 3.0°$ and discretization value $\delta L_{azi.} = 1e-2$. The true quality factor Q_{true} in the simulation is assumed be $Q_{true} = 1$.

As expected, the estimator performance improves with increasing SNR as can be seen from the histogram of the estimation error Q_{err} getting narrower at higher SNR values as well as from the decrease in variance of the estimation error with the SNR increasing as given in figure 4.10b. Additionally, mean of the estimation error is around zero in all the four cases considered, i.e. $E[Q_{err}] \approx 0$. The noise power has thus a significant impact on the performance of the MLE estimator.

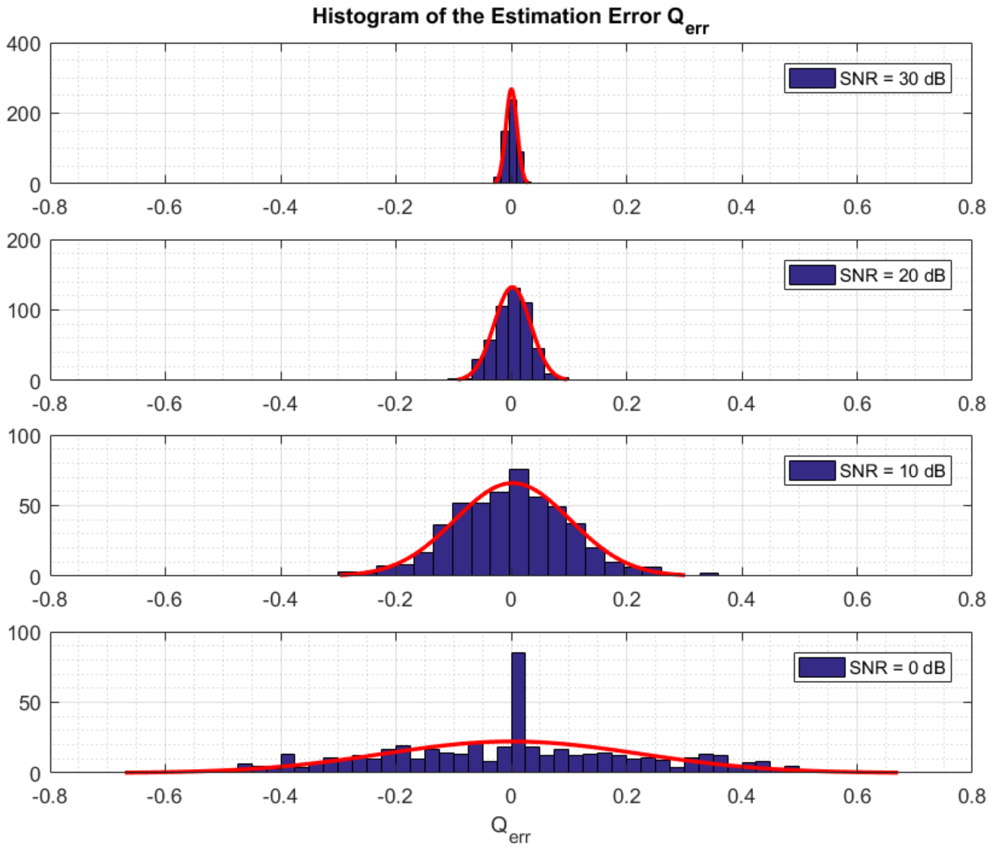

(a) Histograms of the estimation errors for four different SNR values; $SNR = 0\ dB$, $SNR = 10\ dB$, $SNR = 20\ dB$, $SNR = 30\ dB$, after $M = 500$ Monte-Carlo trials.

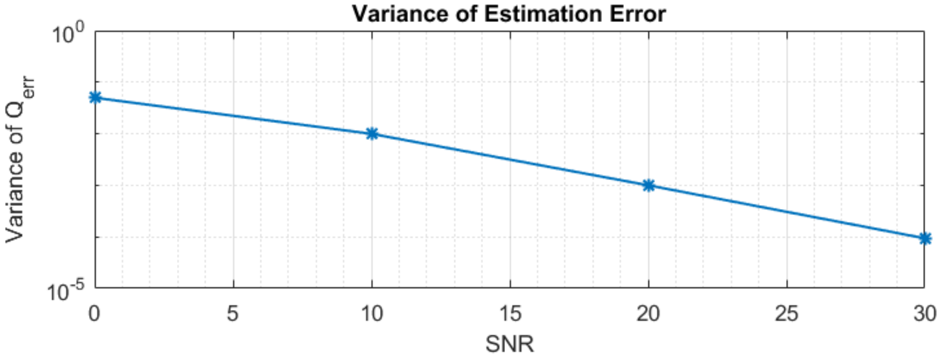

(b) Variance of the estimation errors for the four given SNR values.

Figure 4.10: An evaluation of the estimation error Q_{err} for different SNR values.

Additionally, figure 4.11 gives the result of the evaluation of the estimation error Q_{err} for four different orientation errors σ_ϕ after running the estimator for $M = 500$ Monte-Carlo trials. This result is obtained for $N = 10$ measurements of the realization of a single target where the discretization value $\delta L_{azi.} = 1e-2$ and the $SNR = 30\ dB$. The true quality factor Q_{true} in the simulation is again assumed to be $Q_{true} = 1$.

From the rather constant behaviour of the variance of the estimation error can be seen that, for equal SNR, orientation error σ_ϕ has no significant impact on the distribution of the estimation error, which means, given correct information about potential losses $L_{azi.}$, estimator shows comparable performance for equal SNR. As it was the case for previous evaluation results, mean of the estimation error is again around zero in all the four cases considered, i.e. $E[Q_{err}] \approx 0$. Therefore, one can conclude that the impact of the noise power on the performance of MLE estimator is way bigger than the impact of the loss factor $L_{azi.}$.

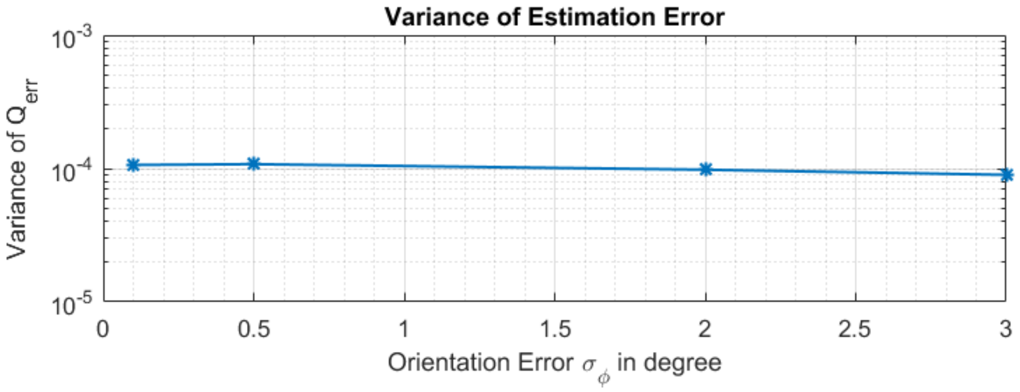

Figure 4.11: Variance of the estimation errors for the four given orientation errors; $\sigma_\phi = 0.1°$, $\sigma_\phi = 0.5°$, $\sigma_\phi = 1.0°$, $\sigma_\phi = 3.0°$, after $M = 500$ Monte-Carlo trials.

Figure 4.12 gives the plots of the histograms and variance of the estimation error Q_{err} obtained for four different number of measurements, i.e. $N = 10$, $N = 100$, $N = 200$ and $N = 500$, of the realization of a single target after running the estimator for $M = 500$ Monte-Carlo trials. Here the error in orientation $\sigma_\phi = 3.0°$, the discretization value $\delta L_{azi.} = 1e-2$ and the $SNR = 30\ dB$. The true quality factor Q_{true} in the simulation is again assumed to be $Q_{true} = 1$.

As expected, taking more measurements improves the performance of the estimator as can be seen from the histogram of the estimation error Q_{err} getting narrower with increasing amount of measurements. This can also be seen from the decrease in variance of the estimation error with the number of measurements N increasing as given in figure 4.12b. Moreover, mean of the estimation error is around zero in all the four cases considered, i.e. $E[Q_{err}] \approx 0$.

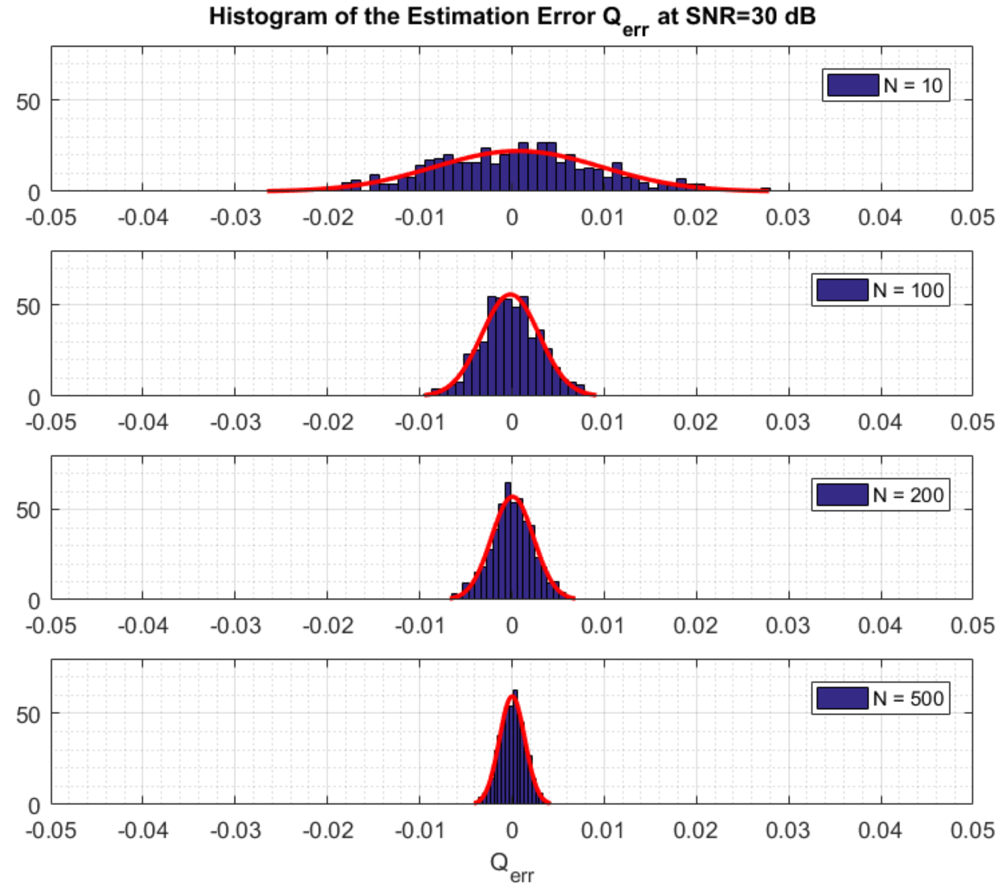

(a) Histograms of the estimation errors for four different number of measurements; $N = 10$, $N = 100$, $N = 200$ and $N = 500$, after $M = 500$ Monte-Carlo trials.

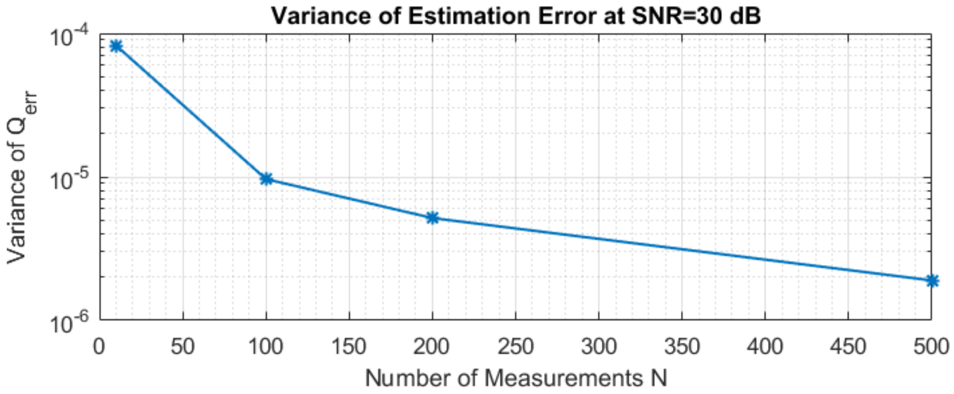

(b) Variance of the estimation errors for the four given different number of measurements.

Figure 4.12: An evaluation of the estimation error Q_{err} for different number of measurements.

4.5. Conclusions

In this chapter, the quality metric (or the quality factor), based on which the healthiness of the automotive radar can be evaluated, is defined and estimated by means of three different estimation methods. This quality metric is defined through radar range equation for automotive FMCW radars.

In Method of Moments method, assuming RCS fluctuation is the only source of noise, thus no additive noise, accurate leg length of l, the known range of R and that the orientation error in azimuth is the only error that affects the received RCS, measurement is regarded as a scaled beta distribution with four parameters. The parameter Q, being the maximum value of the distribution, is estimated by equating sample and population values of the first four central moments using equations 4.12 and 4.13. The estimation formula in terms of the sample variance and sample skewness from equation (4.13) delivered more accurate estimation results which are also validated in terms of the mean squared error of both estimators. Furthermore, estimation accuracy improves with the increasing number of observations.

In the presence of additive noise and prior information on the quality factor Q and considering *multiple measurements of the same realization of a single target*, an estimation of the quality factor is done by means of Maximum a Posteriori (MAP) estimation by solving equation (4.35) numerically. An evalution of the likelihood functions showed that the positions of the maxima of the likelihood functions are independent of the discretization value in numerical computation but they are sensitive to changes in SNR. The relative errors in the position of these maxima decreases with the increasing SNR. An evaluation of the estimator performance in terms of the estimation error is made by means of Monte Carlo simulations for different SNR values, orientation errors, prior pdf's of Q and number of measurements. It is shown that increasing the SNR and taking more measurements improve the performance of the estimator. Furthermore, performance of the estimator is in this case also independent of the amount of orientation errors as well as different normal distributed prior pdf's of Q.

In the presence of additive noise and assuming the case when no prior information on the quality factor Q is available, an estimation of the quality factor Q is done by means of Maximum Likelihood Estimation (MLE). Evaluation of the estimator performance in terms of estimation error for different SNR values, orientation errors and number of measurements showed that the estimator performance improves with increasing SNR and number of observations whereas the performance of the estimator is independent of the amount of orientation errors.

5

Conclusions and Future Work

5.1. Conclusions

The major goal of this project is to provide results and knowledge that will contribute to the improvement of safety of (semi-)autonomous vehicles by means of improving reliability of automotive radars self-diagnostic by which degraded radar performance can be detected via the developed approach based on randomized set of targets that are embedded into road infrastructure.

In order to develop such an approach,

- First, the most appropriate calibration target is determined according to defined target selection criteria, which turned out to be a trihedral corner reflector. Considering visibility and safety issues based on the given geometry of a straight three-lanes European highway configuration, an appropriate position of the calibration target alongside the highway as well as the number of targets to be deployed in a certain range are determined. Based on the given road configuration and two different references of automotive radar specifications, the minimum required size of the corner reflector is obtained to be $l_{min} \geq 0.0840\ m$.

- Then, statistical characteristics of the RCS loss for orientation errors, both in elevation and azimuth plane, errors in leg length as well as the non-orthogonality of the corner walls are discussed. The probability distributions of the loss factors are derived analytically shown that they can be well approximated by beta distribution for small errors in orientation in elevation and azimuth plane and for small angular errors in the alignment of corner walls of the corner reflector. Results are validated by means of matching shape parameters obtained from the derivation and Monte-Carlo simulations at small errors. Therefore, these three loss factors are concluded to be beta distributed.

  Moreover, production of the trihedral corner reflectors should be at most within 1° of precision in the corner walls since the the formula given in (3.58) is applicable only for angular deviations smaller than 1°. *sinc*-nature of this formula results in a second lobe that arises beyond a certain amount of angular error which led to the finding that, in contrast to better visibility, bigger size requires higher production precision in terms of the angular error because the second peak appeared earlier when the size of the reflector gets bigger. Also observed that 3-dB beamwidth decreases with the increasing leg size. From these two results concluded that the β-distribution approximation is applicable only for smaller errors when the leg size increases. Results achived by simulations are then validated by the theory corresponding to the properties of normal distribution. Additionally, the total loss factor is shown to be able to be approximated by a beta distribution as well.

  Together with the results obtained in section 3.6, results of the statistical characteristics of the loss factor due to non-orthogonality helped to find a balance between the size, quality and number of targets to be deployed in a certain range in a given road configuration.

- Finally, the quality metric (or the quality factor), based on which the healthiness of the automotive radar can be evaluated, is defined and estimated by means of three different estimation methods.

  In addition to the assumptions of accurate leg length of l, the known range of R and that the orientation error in azimuth is the only error that affects the received RCS, assuming no additive noise and RCS fluctuation being the only source of noise, quality factor Q is estimated by Method of Moments by equating sample and population values of the first four central moments using formulas given in 4.12 and 4.13. The estimation formula in terms of the sample variance and sample skewness from equation (4.13) delivered more accurate estimation results which are also validated in terms of the mean squared error of both estimators. Furthermore, estimation accuracy improves with the increasing number of observations.

  In the presence of additive noise and prior information on the quality factor Q and considering *multiple measurements of the same realization of a single target*, an estimation of the quality factor is done by means of Maximum a Posteriori (MAP) estimation. An evaluation of the estimator performance in terms of the estimation error is made by means of Monte Carlo simulations for different SNR values, orientation errors, prior pdf's of Q and number of measurements. It is shown that increasing the SNR and taking more measurements improve the performance of the estimator. Furthermore, performance of the estimator is independent of the amount of orientation errors as well as different normal distributed prior pdf's of Q.

  Again considering the *multiple measurements of the same realization of a single target*, the case when in the presence of additive noise and assuming no prior information on the quality factor is available, an estimation of the quality factor Q is done by means of Maximum Likelihood Estimation (MLE). Evaluation of the estimator performance in terms of estimation error for different SNR values, orientation errors and number of measurements showed that the estimator performance improves with increasing SNR and number of observations whereas the performance of the estimator is in this case also independent of the amount of orientation errors.

The developed statistical approach of dynamic evaluation of the automotive radar performance is novel and can directly contribute to real-time evaluation of the radar performance and be used for an appropriate sensor fusion at an autonomous vehicle.

5.2. Future Work

- Trihedral corner reflector was selected to be the most appropriate calibration target to use in this project among the discussed ones. However, it can still be meaningful to consider possible another candidates of calibration targets in the future research.

- The algorithm to estimate the quality factor Q either by means of MAP or MLE is derived for the case of *multiple measurements of the same realization of a single target* because equation (4.29) can be quite complex to solve. In this case it requires the integration over the loss factors of multiple targets. Hence, in presented study we did not solve the most general problem when the radar sensor health estimated using multiple sequential measurements of multiple calibration targets that have statistical uncertainties in their production quality and installation errors. Solving equation (4.29) is left open for future attention in order to solve the full estimation problem in which the case of *multiple measurements of multiple independent targets* have to be considered.

A

Symbols used in the Highway Configurations and Their Numeric Values in a Table

In the next pages, the most important symbols used throughout the figures 2.12, 2.13 and 2.14, their meaning, formulas to calculate their numeric values and their numeric values are given in tables, respectively.

Table A.1: **Important symbols and their numeric values from Figure 2.12**

Symbol	**Description of the Symbol**	**Formula to Compute Numerical Value**	**Numerical Value**
R_{rad}	*Detection Range of the Automotive LRR*	-	200 m
n_{lanes}	*Number of Lanes*	-	3
w_{lane}	*Lane Width*	-	3.75 m
w_{esl}	*Emergency Stopping Lane Width*	-	2.5 m
w_{car}	*Personal Car Width*	-	2.0 m
ϕ_{scan}	*Automotive Radar Antenna Azimuth Scan Angle*	-	15°
Q	*Nearest Possible Target Position to ESL*	$((n_{lanes} \cdot w_{lane}) + w_{esl}$	Q(x,y) = (200 m, 13.75 m)
P	*Furthest Possible Target Position to ESL*	$R_{rad} \cdot \tan(\phi_{scan})$	P(x,y) = (200 m, 53.589 m)
T	*Calibration Target Position*	-	T(x,y) = (200 m,)
d	*Maximum Distance Between Two Successive Calibration Targets*	$((n_{lanes} \cdot w_{lane}) + w_{esl} + d_1) - 0.5 \cdot w_{car})/\tan(\phi_{scan})$	66.243 m
d_1	*Distance between Q and T*	-	5.0 m
α	*Azimuthal Observation Angle Car 3*	$arctan(\frac{((n_{lanes} \cdot w_{lane} + w_{esl} + d_1) - 0.5 \cdot w_{car})}{R_{rad}})$	5.07°
β	*Azimuthal Observation Angle Car 1*	$arctan(\frac{(0.5 \cdot w_{car} + w_{esl} + d_1)}{R_{rad}})$	2.43°
R_1	*Radial Distance Between Car 1 and Calibration Target*	$\sqrt{R_{rad}^2 + (0.5 \cdot w_{car} + w_{esl} + d_1)^2}$	200.180 m
R_3	*Radial Distance Between Car 3 and Calibration Target*	$\sqrt{R_{rad}^2 + (((n_{lanes} \cdot w_{lane}) + w_{esl} + d_1) - 0.5 \cdot w_{car})^2}$	200.786 m
R_4	*Radial Distance Between Car 4 and Calibration Target*	$((n_{lanes} \cdot w_{lane}) + w_{esl} + d_1) - 0.5 \cdot w_{car})/\sin(\phi_{scan})$	68.581 m

Table A.2: **Important symbols and their numeric values from Figure 2.13**

Symbol	**Description of the Symbol**	**Formula to Compute Numerical Value**	**Numerical Value**
R_{rad}	*Detection Range of the Automotive LRR*	-	200 m
w_{lane}	*Lane Width*	-	3.75 m
w_{esl}	*Emergency Stopping Lane Width*	-	2.5 m
w_{car}	*Personal Car Width*	-	2.0 m
ϕ_{scan}	*Automotive Radar Antenna Azimuth Scan Angle*	-	15°
d_1	*Distance between Q and T*	-	*5 m*
d_{min}	*See figure*	$(0.5 \cdot w_{car} + w_{esl} + d_1)/\tan(\phi_{scan})$	
R_{min}	*Radial Distance Between Car 2 and Calibration Target*	$(0.5 \cdot w_{car} + w_{esl} + d_1)/\sin(\phi_{scan})$	32.841 m
β	*Azimuthal Observation Angle Car 1*	$arctan(\frac{(0.5 \cdot w_{car} + w_{esl} + d_1)}{R_{rad}})$	2.43°
ζ	See figure	$90° - \phi_{scan}$	75°
$\Delta\phi_{inc}$	Range of Incident Angles in Azimuth Plane	$90° - \zeta - \beta$	12.57°

Table A.3: **Important symbols and their numeric values from Figure 2.14**

Symbol	**Description of the Symbol**	**Formula to Compute Numerical Value**	**Numerical Value**
R_{rad}	*Detection Range of the Automotive LRR*	-	200 m
n_{lanes}	*Number of Lanes*	-	3
w_{lane}	*Lane Width*	-	3.75 m
w_{esl}	*Emergency Stopping Lane Width*	-	2.5 m
w_{car}	*Personal Car Width*	-	2.0 m
θ_{scan}	*Automotive Radar Antenna Elevation Scan Angle*	-	3°
d_1	*Distance between Q and T*	-	5.0 m
h_{rad}	*Automotive Radar Height*	-	0.5 m
h_{max}	*Maximum Possible Target Height above* h_{rad}	$R_{min} \cdot \tan(\theta_{scan})$	1.72 m
R_1	*Radial Distance Between Car 1 and Calibration Target*	$\sqrt{R_{rad}^2 + (0.5 \cdot w_{car} + w_{esl} + d_1)^2}$	200.180 m
R_3	*Radial Distance Between Car 3 and Calibration Target*	$\sqrt{R_{rad}^2 + (((n_{lanes} \cdot w_{lane}) + w_{esl} + d_1) - 0.5 \cdot w_{car})^2}$	200.786 m
R_4	*Radial Distance Between Car 4 and Calibration Target*	$((n_{lanes} \cdot w_{lane}) + w_{esl} + d_1) - 0.5 \cdot w_{car})/\sin(\phi_{scan})$	68.581 m
R_{min}	*Radial Distance Between Car 2 and Calibration Target*	$(0.5 \cdot w_{car} + w_{esl} + d_1)/\sin(\phi_{scan})$	32.841 m
d_{min}	*See figure*	-	5.0 m
ρ	*Illimunation Angle into Calibration Target from Car 1*	$arctan(R_1/h_{max})$	89.501°
η	*Illimunation Angle into Calibration Target from Car 3*	$arctan(R_3/h_{max})$	89.501°
Ψ	*Illimunation Angle into Calibration Target from Car 2*	$arctan(R_{min}/h_{max})$	87.002°
ω	*Illimunation Angle into Calibration Target from Car 4*	$arctan(R_4/h_{max})$	88.563°

Bibliography

[1] Grace, M.I. ”Automobile radar antenna alignment system using transponder and lasers” U.S. Patent 6,329,952, Dec. 11, 2001.

[2] Grace, M.I. ”Automotive radar antenna alignment system” U.S. Patent 6,335,705, Jan. 1, 2002.

[3] G. Vinci, A. Koelpin, and R. Weigel, “Employing six-port technology for phase-measurement-based calibration of automotive radar,” in Microwave Conference Proceedings (APMC), 2009 Asia-Pacific, 2009, pp. 329 –332

[4] T. Matsuoka, T. Umehara, A. Nadai, T. Kobayashi, M. Satake and S. Uratsuka, ”Calibration of the high performance airborne SAR system (Pi-SAR2),” 2009 IEEE International Geoscience and Remote Sensing Symposium, Cape Town, 2009, pp. IV-582-IV-585, doi: 10.1109/IGARSS.2009.5417443

[5] Feng, Z., Huang, L., Tang, Z., Liu, J., and Zhao, L. (2014). Airborne SAR radiometric calibration using point targets. In 35th International symposium on remote sensing of environment (ISRSE35) IOP publishing IOP conference series: Earth and environmental science 17, 012186. doi:10.1088/1755-1315/17/1/012186.

[6] G. T. Ruck, D. E. Barrick, W. D. Stuart, and C. K. Krichbaum, *Radar Cross Section Handbook*, vol. 1, Plenum Press, New York, 1970.

[7] G. T. Ruck, D. E. Barrick, W. D. Stuart, and C. K. Krichbaum, *Radar Cross Section Handbook*, vol. 2, Plenum Press, New York, 1970.

[8] K. Werber et al., “How do traffic signs look like in radar?” in Proceedings of the 44th European Microwave Conference. EuMA, 2014, pp. 135–138.

[9] Hasan Iqbal, Frank Bogelsack, and Christian Waldschmidt, ”Polarimetric RCS Analysis of Traffic Objects”, in Proceedings of the 14th European Radar Conference, EuMA, 2017.

[10] ITU-R Recommendation, M.2057-0, ”Systems characteristics of automotive radars operating in the frequency band76-81 GHz for intelligent transport systems applications”, International Communication Union, 2014.

[11] N. Chen, *Millimetre wave propagation and scattering phenomena for automotive radar*, MSc Thesis, Delft University of Technology (2016).

[12] Continental-automotive.com. (n.d.). [online] Available at: https://www.continental-automotive.com/getattachment/9b6de999-75d4-4786-bb18-8ab64fd0b181/ARS30X-Datasheet-EN.pdf.pdf [Accessed 13 Jun. 2019].

[13] C. Craeye , P. Sobieski , E. Robin & A. Guissard (1997) Angular errors in trihedrals used for radar calibrations, International Journal of Remote Sensing, 18:12, 2683-2689, DOI: 10.1080/014311697217549

[14] Commons.wikimedia.org. (n.d.). File: Empirical Rule.PNG - Wikimedia Commons. [online] Available at: https://commons.wikimedia.org/wiki/File:Empirical_Rule.PNG [Accessed 7 Mar. 2019].

[15] Da-Yin Fan (1991), The distribution of the product of independent beta variables, Communications in Statistics - Theory and Methods, 20:12, 4043-4052, DOI: 10.1080/03610929108830755

[16] W. P. Elderton, *Frequency Curves and Correlation*, Charles and Edwin Layton, London, 1906.

[17] N. L. Johnson, S. Kotz, N. Balakrishnan, ”Beta Distributions,” in *Continuous Univariate Distributions*, vol. 2, 2nd ed., USA: Wiley, 1995, ch. 25.